CCFE
CULHAM CENTRE FOR FUSION ENERGY

UK Atomic Energy Authority

UKAEA-CCFE-PR(21)33

K. Arakawa, Z. Bergstrom, M.J. Caturla, S.L. Dudarev, F. Gao, M.R. Gilbert, A.M. Goryaeva, S.Y. Hu, X. Hu, R.J. Kurtz, A. Litnovsky, J. Marian, M.-C. Marinica, E. Martinez, E.A. Marquis, D.R. Mason, B.N. Nguyen, P. Olsson, Y. Osetskiy, D. Senor

Perspectives on multiscale modelling and experiments to accelerate materials development for fusion

Perspectives on multiscale modelling and experiments to accelerate materials development for fusion

K. Arakawa, Z. Bergstrom, M.J. Caturla, S.L. Dudarev, F. Gao, M.R. Gilbert, A.M. Goryaeva, S.Y. Hu, X. Hu, R.J. Kurtz, A. Litnovsky, J. Marian, M.-C. Marinica, E. Martinez, E.A. Marquis, D.R. Mason, B.N. Nguyen, P. Olsson, Y. Osetskiy, D. Senor

This is a preprint of a paper submitted for publication in Journal of Nuclear Materials

Perspectives on multiscale modelling and experiments to accelerate materials development for fusion

K. Arakawa[a], Z. Bergstrom[b], M.J. Caturla[c], S.L. Dudarev[d], F. Gao[e], M.R. Gilbert[d,*], A.M. Goryaeva[f], S.Y. Hu[g], X. Hu[h], R.J. Kurtz[g], A. Litnovsky[i,j], J. Marian[k], M.-C. Marinica[f], E. Martinez[l,m], E.A. Marquis[n], D.R. Mason[d], B.N. Nguyen[g], P. Olsson[o], Y. Osetskiy[h], D. Senor[g], W. Setyawan[g], M.P. Short[p], T. Suzudo[q], J.R. Trelewicz[r], T. Tsuru[q], G.S. Was[e], B.D. Wirth[b], L. Yang[b], Y. Zhang[h], S.J. Zinkle[b]

[a] *Next Generation TATARA Co-Creation Centre, Organization for Industrial Innovation, Shimane University, Matsue, Japan*
[b] *University of Tennessee-Knoxville, Knoxville, TN, USA*
[c] *Facultad de Ciencias, Fase II, Department of Fsica Aplicada, Universidad de Alicante, Alicante, Spain*
[d] *United Kingdom Atomic Energy Authority, Culham Centre for Fusion Energy, Culham Science Centre, Abingdon, Oxon, OX14 3DB, UK*
[e] *Department of Nuclear Engineering and Radiological Sciences, University of Michigan, Ann Arbor, MI, 48109, USA*
[f] *Université Paris-Saclay, CEA, Service de Recherches de Métallurgie Physique, 91191, Gif-sur-Yvette, France*
[g] *Pacific Northwest National Laboratory, Richland WA, USA*
[h] *Materials Science and Technology Division, Oak Ridge National Laboratory, Oak Ridge, TN 37831, USA*
[i] *Forschungszentrum Jülich GmbH, Institut für Energie- und Klimaforschung, 52425 Jülich, Germany*
[j] *National Nuclear Research University MEPhI, Kashirskoe sh.31, 115409, Moscow, Russian Federation*
[k] *Department of Materials Science and Engineering, University of California, Los Angeles, CA, USA*
[l] *Department of Mechanical Engineering, Clemson University, Clemson, SC 29623, USA*
[m] *Department of Materials Science and Engineering, Clemson University, Clemson, SC 29623, USA*
[n] *Department of Materials Science and Engineering, University of Michigan, Ann Arbor, MI, 48104, USA*
[o] *KTH Royal Institute of Technology, Nuclear Engineering, SE106 91 Stockholm, Sweden*
[p] *Massachusetts Institute of Technology, Cambridge, MA, USA*
[q] *Japan Atomic Energy Agency, Tokai-mura, Naka-gun, Ibaraki-ken, Japan*
[r] *Department of Materials Science and Chemical Engineering, Stony Brook University, Stony Brook, NY, USA*

Abstract

Prediction of material performance in fusion reactor environments relies on computational modelling, and will continue to do so until the first generation of

*Corresponding author
Email address: mark.gilbert@ukaea.uk (M.R. Gilbert)

fusion power plants come on line and allow long-term behaviour to be observed. In the meantime, the modelling is supported by experiments that attempt to replicate some aspects of the eventual operational conditions. In 2019, a group of leading experts met under the umbrella of the IEA to discuss the current position and ongoing challenges in modelling of fusion materials and how advanced experimental characterisation is aiding model improvement. This review draws from the discussions held during that workshop.

Topics covering modelling of irradiation-induced defect production and fundamental properties, gas behaviour, clustering and segregation, defect evolution and interactions are discussed, as well as new and novel multiscale simulation approaches, and the latest efforts to link modelling to experiments through advanced observation and characterisation techniques.

Keywords: multiscale modelling, fusion materials, radiation damage, hydrogen and helium, defect evolution, experimental characterisation

---

Contents

1. Introduction

This article provides a review of the status of fusion materials theory and modelling, largely drawn from the Fusion Materials Technology Collaboration Program (FM TCP) workshop held in June 2019. The workshop was organized with the specific aim of discussing the opportunities for experimental validation of recent advances in theory and modelling that offer the potential to accelerate materials development for fusion energy. The Fusion Materials TCP is part of a network of autonomous collaborative partnerships focused on a wide range of energy technologies, known as Technology Collaboration Programs or TCPs. The TCPs are organized under the auspices of the International Energy Agency (IEA), but the TCPs are functionally and legally autonomous. Views, findings and publications of the Fusion Materials TCP do not necessarily represent the views or policies of the IEA Secretariat or its individual member countries.

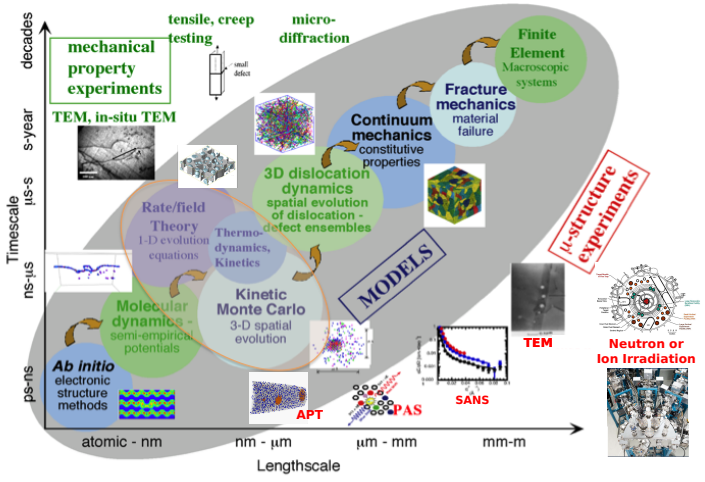

Figure 1: Illustration of an integrated experimental and computational science-based approach to the multiscale investigation of materials degradation due to high-energy particle irradiation.

The workshop was held in Walla Walla, WA and organized by Mark Gilbert, Rick Kurtz and Brian Wirth. It represents the 6th meeting on fusion materials theory and modelling organized under the auspices of the FM TCP, although there had been a significant gap since the 5th workshop that occurred in Alicante Spain in 2013. The workshop series has consistently been organized around discussing the latest developments in computational modelling and theory of materials behaviour in fusion environments, which are characterized by a high flux of neutrons with an energy spectrum peaked at 14 MeV, along with time varying thermal-mechanical loading conditions. The simulation paradigm for this computational modelling is the so-called multiscale approach, which relies on a parameter-passing framework where multiple temporal and spatial domains are divided into regimes according to the characteristic length and timescales of the physical phenomena involved. Figure 1 provides a schematic diagram of a science-based, and integrated experimental and computational modelling approach to investigating materials degradation in a nuclear environment.

Figure 1 illustrates the hierarchical parameter passing paradigm of multiscale modelling, presently dominating the scientific thought in the field. It begins with the smallest length and shortest time scales, and seeks to integrate *ab initio* electronic structure calculations, typically relying on density functional theory (DFT), followed by molecular dynamics (MD) simulations, kinetic Monte Carlo (KMC), rate-theory or phase-field simulations with thermodynamics and kinetics through the passing of information about the controlling physical mechanisms over the relevant length and time scales to predict microstructure evolution during high-energy neutron irradiation. Detailed microstructural information generated using the multiscale approach can form a basis for modelling the mechanical behaviour through meso (represented by 3D dislocation dynamics) and continuum scale models, which must be incorporated into fracture mechanics models at the continuum scale in order to predict material deformation and failure of individual (fusion) reactor components, through finite element modelling. In the figure, individual modelling techniques are identified in a series of linked process ellipses, with representative schematics illustrating the type of modeled material behaviour through the length and timescales. The passing of information between the scales is represented through a series of arrows.

Of course, multiscale modelling by itself, given the drastic approximations involved in some of the models, is insufficient to fully predict the performance of complicated engineered structures in the fusion nuclear environment, and the science-based multiscale paradigm requires a close integration of modelling predictions with a suite of experimental characterisation techniques. This is necessary not only for experimental validation, but also to have the experiments confirm, or identify, key mechanisms of defect cluster interactions with transmutation gases that will be produced in much larger quantities in fusion materials than are typical of fission neutron irradiation. A sub-set of these techniques is represented for microstructural characterisation on the lower side of the gray sphere and for experimental mechanical behaviour/testing methods on the upper side. As noted earlier, a specific aim of the June 2019 workshop was discussing the opportunities for experimental validation of recent advances in

modelling and theory.

The workshop involved approximately 30 participants and 25 invited presentations. The speakers provided both a review of the current status of knowledge and updates on the latest advances in computational modelling capability, including machine learning, and strove to identify how advances in both simulation and experimental capability could feed back onto both research techniques to advance the capability for simulation driven experimental design. A common question within the multiscale modelling paradigm relates to ensuring that we have optimized the implementation of scale bridging by defining the most important mechanisms at the lowest length scales and incorporating them into continuum or reduced order models that can connect to experimental results for benchmarking and validation. Another common theme in the presentations at the workshop involved the emerging technique of machine learning, and how that offers the potential to improve reduced parameter models and to automate the scale bridging parameter passing within the multiscale modelling framework. The remainder of this article reviews the key issues and outstanding questions within each of the 4 main topical themes discussed in the workshop: simulating defect production, modelling and observing microstructural evolution, developing techniques to predict how microstructure influences properties, and how the behaviour of gas influences material. A final summary section reviews the advances and highlights the future challenges and opportunities for the future implementation of multiscale modelling to accelerate materials development for fusion energy.

2. Simulating defect production and fundamental properties

This section describes recent advances in modelling and interpreting the production and behaviour of defects in materials exposed to the high-energy neutron irradiation that will be produced in fusion reactors. The following subsections discuss: the development of dynamic simulations combining DFT and MD to explore damage creation using quantum accuracy (Section 2.1), and how DFT calculations are still being used to provide important information about the properties of fundamental defects in crystalline materials (2.2). Then we discuss the use of classical MD to explore the interaction of cascades and sub-cascades in W (Section 2.3) and the analysis of the stress fields created by defects in those cascades that will have a fundamental impact on materials at the macro-scale (2.4). A final sub-section (2.5) is devoted to describing an important recent development in the computational simulation of materials, namely how machine learning can overcome the limitations of both DFT (small scale and short time accessible to dynamic DFT simulations) and classical MD (insufficient accuracy) by enabling a more accurate description of a material at atomic level at a relatively low computational cost.

2.1. modelling primary damage on the quantum scale

When energetic particles interact with materials they can cause a number of different effects, including electronic excitations, nuclear reactions and displace-

ment of ions in the material. If the energetic transfer to the ions is sufficient, past the threshold displacement energy (TDE), the displaced ion will not return to its original site, leaving behind a vacancy and forming a self-interstitial, thus damaging the crystal structure itself, resulting in a primary damage state. Since the material in a fusion reactor environment will be under continual highly energetic irradiation, primary damage will form all through the materials during the entire operation of the reactor. The evolution of this damage state, when the point defects and directly generated defect clusters diffuse, recombine and agglomerate, can lead to a wide variety of changes of materials properties that are limiting the safe operation lifetime.

The primary damage state itself has historically been studied using classical- and semi-classical methods [1, 2, 3] and only in more recent times have a quantum description of the damage dynamics been developed [4]. From the quantum, or *ab initio*, dynamic studies, it has been seen that even though the resulting predictions from semi-classical models are often on average reasonable, significant details of the physical interactions are not well described and fully *ab initio* dynamic modelling has an important role to play. *Ab initio* MD is, however, several orders of magnitude more computationally expensive than classical MD, and therefore the limits on what can be simulated are severe. The simulation cell sizes for these types of simulations are currently limited to a few hundred atoms. The intrinsic character of primary damage simulations, where a few atoms in the simulation cell experience extreme local compression during the trajectory, is a clearly limiting factor for the computational efficiency. The very small closest approach distances that occur, in comparison with canonical static or quasi-static defect relaxation simulations, render some of the commonly used time-saving approximations invalid. In particular, the minimal valence (or frozen core) model that is commonly used in DFT simulations, cannot be applied with confidence for dynamic primary damage simulations, since the close compression will cause orbital overlap even for the outermost core shells, which then add to the repulsive interaction. It is clearly important to include at least the last core shell explicitly in the simulations to correctly describe the local compression conditions. However, this comes at a great computational cost. TDE studies from the literature have used around 100-200 atoms for some ceramic compounds [5, 6, 7], while for metals it has been shown that at least 500 atoms are needed [4]. The difference between the two classes is the bonding character and consequent degree of localisation that is clearly stronger in ceramics than in metals, where interactions and dynamics are naturally more dispersive. Angularly resolved TDE in Fe (see, for example, figure 1 in [4]), predicted using either semi-classical molecular dynamics (CMD) or using *ab initio* (quantum molecular dynamics [QMD]) are relatively similar. The average TDE from these two approaches are 39 eV (CMD) versus 32 eV (QMD). However, at finer resolution, many differences exist; demonstrating the importance of the higher accuracy model (QMD).

In order to go beyond the threshold events which constitute the lower limit of primary damage, some method development is clearly necessary. Small displacement cascade simulations would have to be carried out in simulation cells

of a few thousand atoms, and for timescales of around ten picoseconds at least. For this reason, the community has been developing methods to speed up QMD simulations for primary damage events. One such development, LAVAX [8] for LAMMPS, is a method to locally switch potentials on the fly during the trajectory so that the major part of the simulation cell, which experiences near-equilibrium conditions and coordination distances, is treated by a minimal valence potential, where the frozen core description is maximally utilized; while the atoms that take active part in the primary damage formation are treated using an expanded set of valence electrons, where at least the shell under the canonical valence is explicitly included in the potential. In this way the orbital overlap that occurs at close compression conditions is taken into account. Since the primary damage event is highly stochastic in nature, one cannot easily determine which atoms will undergo strong local compression in a general case and therefore the method includes a predictor simulation loop, that uses classical MD to determine in advance which atoms will most probably undergo local compression in the next few time steps. A speedup of an order of magnitude can be achieved with this method, which opens the door for QMD simulations of small displacement cascades.

2.2. Structure and volumes of elementary defects

Historically, the majority of studies exploring the production of defects assumed a perfect crystalline state of material before a primary collision impact event [2]. This assumption, with some notable exceptions involving for example simulations and observation of collision cascades in nanocrystalline materials [9, 10], and studies of overlapping cascades [11], have focused attention on the exploration of the most elementary point defects forming in crystals under irradiation. The structure of these defects as well as their formation and migration energies in pure elements and alloys have now been determined using density functional theory calculations [12] that not only provided the data required for the quantitative interpretation of observations of electrical resistivity recovery of irradiated materials [13, 14], but also helped resolve long outstanding questions related to the observation and interpretation of X-ray diffraction data on elementary defects [15].

In addition to predicting energies and structures of defects in a variety of materials, density functional theory calculations have recently enabled performing accurate computation of relaxation volumes of defects [16, 17]. Volumes of defects have long been a subject of extensive experimental effort [18], which showed that measuring these volumes accurately was challenging. It is also hard to evaluate these volumes using atomistic simulations and semi-empirical interatomic potentials because the results prove highly sensitive to the assumed many-body law of interaction between the atoms [19]. Still, knowing the volumes of defects is critically significant to modelling radiation effects in materials because these volumes determine the magnitude of local lattice deformations [19] as well as macroscopic lattice swelling or contraction resulting from the accumulation of defects [20].

Table 1: Relaxation volumes of a vacancy and several high-symmetry self-interstitial atom defects in body centred cubic metals, computed using density functional theory and the GGA-PBE functional [16]. Volumes are given in atomic units $\Omega_0 = a^3/2$, where a is the bcc lattice parameter. Volume of a $\langle 111 \rangle$ SIA defect is the average between a crowdion and a dumbbell configuration.

element	vacancy	$\langle 111 \rangle$	$\langle 110 \rangle$	tetrahedral	$\langle 100 \rangle$	octahedral
Li	-0.532	1.17	1.227	1.232	1.246	1.239
Na	-0.443	1.32	1.348	1.379	1.389	1.416
K	-0.397	1.37	1.393	1.425	1.446	1.449
Rb	-0.394	1.41	1.429	1.463	1.497	1.498
Cs	-0.353	1.45	1.451	1.498	1.547	1.553
Ba	-0.343	1.16	1.106	1.016	0.958	0.905
V	-0.351	1.47	1.466	1.495	1.529	1.530
Nb	-0.445	1.55	1.538	1.571	1.651	1.650
Ta	-0.451	1.52	1.499	1.557	1.636	1.645
Cr	-0.414	1.37	1.434	1.606	1.610	1.609
Mo	-0.372	1.538	1.584	1.617	1.680	1.675
W	-0.324	1.71	1.753	1.791	1.868	1.868
Fe	-0.220	1.66	1.620	1.619	1.858	1.851

Relaxation volumes of a vacancy and several high-symmetry configurations of self-interstitial atom defects in all the bcc and fcc metals, computed using density functional theory [16, 17], are summarised in Tables 1 and 2. The values still exhibit slight sensitivity to the choice of the exchange-correlation functional used in density functional theory calculations [16, 17], but the margin of error is now many times lower than that of values computed using semi-empirical potentials or measured experimentally [18, 19].

From the data given in the Tables we see that the formation of a Frenkel pair of a vacancy and a self-interstitial atom defect produces large net expansion of the lattice, which in all the metals is at least of the order of one atomic volume per Frenkel pair, and in aluminium exceeds two atomic volumes per Frenkel pair. Lattice distortions produced by the defects are fairly localised, and atomic displacements vary as $u(r) \sim 1/r^2$ as a function of distance r from a point defect. It is this character of variation of displacements as a function of distance from the centre of a defect, or a defect cluster, that is responsible for the relaxation volume of a point defect being a well defined quantity. Indeed, the relaxation volume is proportional to the product of atomic displacements $u(r)$ at an arbitrarily chosen surface, which varies as $u(r) \sim r^{-2}$, and the surface area, which scales as r^2, producing a convergent result independent of r. Lattice distortions generated by the defects generate internal stresses and deformations in materials exposed to irradiation, and as we show below, the magnitude of these stresses and deformations can be very high.

Table 2: Relaxation volumes of a vacancy and several high-symmetry self-interstitial atom defects in face centred cubic metals, computed using density functional theory and the GGA-PBE functional [17]. Volumes are given in atomic units $\Omega_0 = a^3/4$, where a is the fcc lattice parameter. Volume of a $\langle 110 \rangle$ SIA defect is the average between a crowdion and a dumbbell configuration.

element	vacancy	$\langle 100 \rangle$	octahedral	$\langle 110 \rangle$	$\langle 111 \rangle$	tetrahedral
Ca	-0.234	1.408	1.413	1.301	1.363	1.386
Al	-0.244	2.301	2.406	2.465	2.506	2.530
Ni	-0.358	1.792	1.842	1.867	1.864	1.866
Cu	-0.361	1.767	1.832	1.822	1.847	1.850
Sr	-0.211	1.843	1.777	1.657	1.740	1.798
Rh	-0.378	1.963	1.988	2.057	2.077	2.054
Pd	-0.430	1.836	1.884	1.892	1.897	1.918
Ag	-0.258	1.890	1.947	1.939	1.989	1.999
Ir	-0.349	1.935	1.969	2.029	2.075	2.048
Pt	-0.456	2.023	2.023	2.101	2.100	2.131
Au	-0.346	2.039	2.086	2.081	2.166	2.178
Pb	-0.342	1.570	1.661	1.521	1.525	1.520
Th	-0.331	1.998	1.931	2.140	2.077	2.028

2.3. Effect of cascade morphology on defect clustering in high-energy cascades

It has been recognized that high-energy cascades in Fe exhibit well-separated cascade fragments known as sub-cascades [21, 22]. However, cascades in W exhibit no break-ups [23, 24]. Instead, the morphology of high-energy cascades in W consists of interconnected sub-cascades [23, 22]. Even though the notion of sub-cascade is less clear in such a morphology, the morphology is different from that of low-energy cascades where no sub-cascades form. By following the evolution of atomic density map (to reveal the morphology) and correlating it with the location of surviving defect clusters, the interconnection of sub-cascades is shown to facilitate the formation of large defect clusters in W cascades [23, 25]. A large interstitial cluster forms when a highly dense region of displaced atoms emanating from a sub-cascade moves into the low-density region (core) of a nearby sub-cascade. In such a process, a large vacancy cluster often forms in the core of the sub-cascade left behind by the displaced atoms. The different morphologies of high-energy cascades between W and Fe result in distinctively different defect cluster size and spatial distributions.

Figure 2a shows an example of $\langle 100 \rangle$ and $\langle 111 \rangle$ interstitial (SIA) loops, and a $\langle 100 \rangle$ vacancy loop formed in a single cascade in W obtained from MD simulations [26]. In fact, these SIA loops both form from highly dense wave front emanating from the same sub-cascade whose core becomes the vacancy loop. The number of SIAs in the $\langle 100 \rangle$ and $\langle 111 \rangle$ loops is 61 and 65, respectively, while the vacancy loop contains 153 vacancies. In the figure, dumbbell atoms are colored based on their orientation. The average orientation of dumbbells within an SIA cluster is taken as the Burgers vector of the cluster. A misorientation angle θ_{I-V} is defined as the angle between the Burgers vector of an SIA

cluster and the position vector of the cascade core from the SIA cluster. The center of mass of the largest vacancy cluster (in this case is the ⟨100⟩ vacancy loop) is taken as the core location. The distance between the SIA cluster and the core is denoted as d_{I-V}. Figure 2b and c show the distributions of θ_{I-V} and d_{I-V} for W cascades at 300 K and 1025 K.

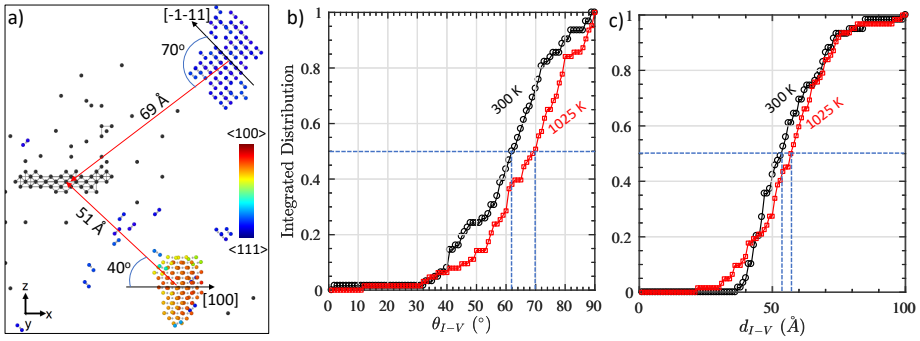

Figure 2: (Color online) a) A snapshot of surviving defects in a 100-keV cascade in W at 300 K where vacancies are plotted as black dots while dumbbell atoms are colored based on their orientation. Red arrows are position vectors of the cascade core (taken as the largest vacancy cluster) from SIA clusters. Black arrows are the Burgers vector direction of the SIA clusters. b) and c) Distribution of misorientation angle of θ_{I-V} and distance d_{I-V} of SIA clusters with respect to cascade core (see text) collected from 50, 60, 75, 100, 150, and 200 keV cascades in W (only clusters with at least 30 SIAs are taken into account).

An important feature of the distribution of θ_{I-V} is that it is not random. In fact, the number of clusters with $\theta_{I-V} < 30°$ is negligible. Therefore, it is suggested that multi-scale radiation damage accumulation simulations should use primary defect states as obtained in the cascades rather than assuming a random distribution. Perhaps a more crucial aspect that would influence the fidelity of multi-scale simulations is that loops with various characters (e.g. ⟨100⟩, ⟨111⟩, and mixed) are generated in cascades [26, 27], in which they exhibit vastly different diffusivity in W. Therefore, taking into account the kinetics of transformation between different characters, particularly from mixed loops into pure loops in the multi-scale simulations is potentially critically necessary. Research to explore the kinetics of mixed loop transformation is largely needed in the future.

2.4. Elastic stress produced by radiation defects

Defects generated by irradiation are nothing but strong localised non-linear deformations of the lattice. Anharmonic interactions between atoms in the central, most strongly distorted, core region of a defect structure give rise to the fact that defects can be characterised by well-defined relaxation volumes, which are large and positive for self-interstitial atom defects, and negative for vacancies. These relaxation volumes can be computed using density functional theory, and a comprehensive compilation of relaxation volumes of defects computed for a

variety of elemental metals is given in Tables 1 and 2. Relaxation volumes can also be computed for clusters of defects [28], as well as for impurities or solute atoms in alloys.

A defect or a cluster of defects produces elastic stress σ_{ij} in the lattice surrounding the defect. At a relatively large distance from a defect, situated at $\mathbf{R}$, this stress can be evaluated using the formula [29, 30]

$$\sigma_{ij}(\mathbf{x}) = -C_{ijkl} P_{mn} \frac{\partial^2 G_{km}(\mathbf{x}-\mathbf{R})}{\partial x_l \partial x_n}, \tag{1}$$

where repeated indices imply summation, C_{ijkl} is the tensor of elastic constants of the material and $G_{km}(\mathbf{x}-\mathbf{R})$ is the elastic Green function. In the above equation, P_{mn} is the elastic dipole tensor of the defect, which is a fundamental quantity relating the structure of a defect to the long-range elastic strain that it produces in the surrounding lattice [30, 31]. Elements of the dipole tensor P_{mn} of a defect are related to its relaxation volume by a linear transformation [32, 30], showing that the larger is the relaxation volume of the defect the larger is the stress that it produces in the surrounding lattice. Equation (1) also explains how the fluctuating internal stress, developing in a material following its exposure to irradiation, is related to non-linear lattice distortions in the core regions of radiation-induced defects.

Since stress is a tensor quantity, described by a symmetric 3×3 matrix $\sigma_{ij}(\mathbf{x})$ involving six independent matrix elements, for the purpose of evaluating the overall magnitude of stress it is convenient to use a single scalar quantity, computed by combining all its matrix elements. A suitable scalar quantity, called the von Mises stress σ_{vM}, which conveniently is positive definite, equals

$$\sigma_{vM}(\mathbf{x}) = \sqrt{\frac{3}{2}\sigma_{ij}(\mathbf{x})\sigma_{ji}(\mathbf{x}) - \frac{1}{2}\left[\sigma_{ii}(\mathbf{x})\right]^2}, \tag{2}$$

where repeated indices imply summation, and hence $\sigma_{ii} = \sigma_{11} + \sigma_{22} + \sigma_{33}$. In Figure 3 we plotted the real-space distribution of the von Mises stress, computed using equation (2) and showing the stress field generated by a cluster of defects formed following a high-energy collision cascade event in crystalline W.

In agreement with equation (1), at large distances from the defects formed in a cascade, the von Mises stress varies as the inverse cube of distance to the centre of the cascade, $\sigma_{vM}(\mathbf{x}) \sim |\mathbf{x}-\mathbf{R}|^{-3}$. Close to the centre of the cascade where lattice is strongly distorted, stress is very high, approaching the shear modulus of the material. This is not surprising since the magnitude of stress reflects the scale of lattice deformation in the core of a defect or a dislocation. The magnitude of lattice strain in the core of a defect or a dislocation is of the order of 10 to 15% [34, 35, 36].

Whereas stress diminishes relatively rapidly as a function of distance away from an individual isolated defect or a cluster of defects, the overall level of lattice distortions and deformations in a material accumulates as the density of defects increases with exposure to irradiation. For example, if we take 10 nm as a characteristic measure of the spatial extent of the stress field of debris

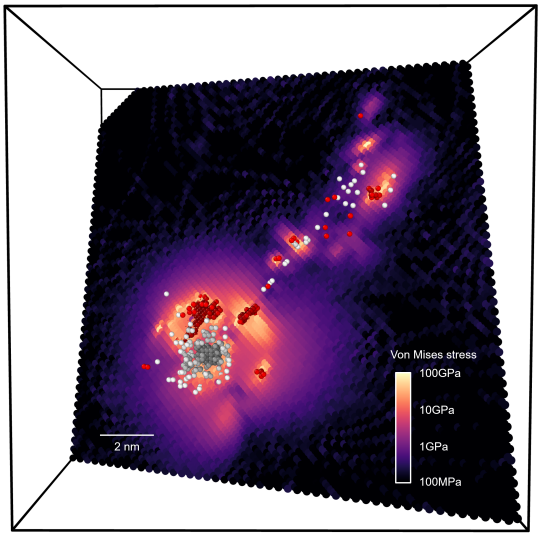

Figure 3: Spatial distribution of stress generated by defects produced by a collision cascade event in crystalline bcc W. The cascade shown in the figure was initiated by a 150 keV primary knock-on atom. Vacancies (white spheres), and interstitials (red spheres), were identified using a Wigner-Seitz defect analysis. The spatial distribution of stress is described by the von Mises invariant of the stress tensor, plotted in a {211} plane intersecting the three-dimensional structure of cascade debris. Note that close to the defects the von Mises stress is as high as 100 GPa, which is comparable to the shear modulus of pure crystalline tungsten $\mu = 160$ GPa. Reproduced from Ref. [33] with permission from the American Institute of Physics.

produced by the cascade shown in Figure 3 and note that this cascade contains several hundred individual defects, we find that defects with the average volume concentration of 1% per lattice site, corresponding to the radiation exposure of $\sim$0.01 dpa, produce high internal stress, fluctuating from one location to another in the bulk of an irradiated material on the scale varying from hundreds of MPa to several GPa.

2.5. Bridging the gap between quantum and classical methods by using machine learning (ML)

In the last decade, materials science was continuously impacted by the emergent fields of mathematical statistics, namely, artificial intelligence (AI) and machine learning (ML). The ability of computers to acquire knowledge by extracting patterns from raw data is known as *machine learning*. These representations of the data give computers the ability to learn without being explicitly programmed. The performance of ML algorithms strongly depends on the representation of data they are given as input. Each piece of representation is called a *feature*, *fingerprint* or *descriptor*. In the case of atomic-scale materials science, ML approaches propose a notion of atomic descriptors. The atomic descriptors enable a specific numerical representation of the crystal structure

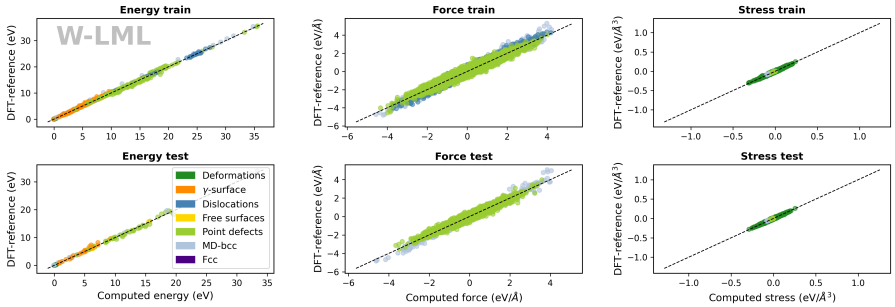

Figure 4: Linear ML (LML) potential for W. Each subplot provides a comparison of the energies, forces and stress with the corresponding DFT values from the database. Atomic systems that carry information on different materials properties (e.g., containing different structural defects) are depicted with different colors.

and its invariant description with respect to physical principles and symmetry, including permutation of atoms, translational and rotational invariance. These functions make it possible to capture the essential features of the individual atomic environments in a space of fixed dimensionality, referred to as the descriptor space. Thus, instead of using $\mathbb{R}^{3N}$ dimensional description of the local atomic environments, one employs a space with the dimension D independent of the number of degrees of freedom $\mathbb{R}^D$. This space with fixed dimension, independent of the system size, is the place for doing statistical correlations in order to build accurate atomistic force fields (see Section 2.5.1 below), or to characterize structural defects (Section 2.5.2).

2.5.1. ML force fields

An accurate description of condensed matter properties requires a precise knowledge of the material at the atomic scale. By using an inter-atomic potential, the energy of bonding between atoms is expressed solely as a function of atomic coordinates, with the electronic degrees of freedom included only implicitly. For example, in metals where the functional form of the Density of States is relatively simple, the Embedded Atom Method (EAM) potentials [37, 38, 39, 40, 41, 42] are valid and successfully and widely applied. For materials under irradiation many important results have been achieved using EAM potentials. More than 1500 studies have used EAM potentials designed for W [43, 44] and Fe [45, 46, 47] to study irradiated materials. This success would imply that there is no need to explore other avenues to parametrize the interatomic interactions. However, there are two major reasons that drives new developments and perspectives. Firstly, the fitting process of traditional potentials is limited and rigid. Facilitated by the continuous increase in computational power and parallel computing, *ab initio* approaches constantly reveal new hidden aspects of defects. The empirical potentials should integrate these new findings, but this is challenging due to increased complexity and the risk of overfitting when trying to match too many scenarios. Alternatively, the un-

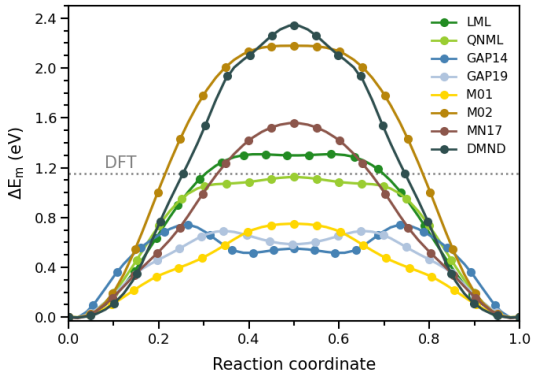

Figure 5: Energy barriers of three-vacancy migration in bcc W computed using different interatomic potentials. The comparison is done between the semi-empirical potentials: M01 and M02 [44], MN17[48], DMND [43], and the Ml potentials: LML and QNML [49, 50], GAP14 [51] and GAP19[52]. The dotted grey line indicates the DFT calculations from Ref.[48].

derlying physics can be changed, as has been attempted with potentials such as MEAM, BOP, ReaxFF, COMB, etc. Secondly, the physics models impose the scalability of numerical methods. A detailed analysis of existing numerical methods in material science suggests that there is a gap between the less accurate empirical methods that scale as maximum in N^2 (N being the number of atoms) and more accurate electronic structure calculations, that scale at least as N^3. Although the electronic structure methods such as tight binding or hybrid electronic structure-empirical methods (e.g. QM/MM) attempt to bridge the gap between ab initio $> N^3$ methods and empirical $< N^2$ methods, they are not completely successful and have unfavorable scaling.

Artificial intelligence methods can be employed to fill the scaling gap while also enabling the creation of new functions that can support more scenarios.

The first attempt to couple artificial intelligence and atomic-scale materials science was proposed by Behler and Parrinello in 2007 [53]. Compared to the traditional approach, the process of ML potential design differs by in three ways:

i. the database is on an equal footing with the fitting formalism. ML potentials require using an extensive training database because its content has a strong impact on accuracy and transferability of the potential. The design of the database, by including the relevant information as well as the suitable selection, called sparsification, is a crucial point for achieving an efficient ML potential. Goryaeva et al [54] recently proposed a novel solution for solving the matrix problem, which is based on assigning each atom a distortion score.

ii. all the database configurations, with different number of atoms, are mapped into the descriptor space. This projection is ensured by a descriptor function, which also influence the potential accuracy and, therefore, represents an important intrinsic characteristic of the potential. The dimension of

descriptor space range from a few tens to a few thousand components. The descriptors can encode the local geometry on neighbouring atoms using the distances or /and angles between atoms [53, 55, 56], spectral analysis of local atomic environments [55, 56] or involved tensorial description of atomic coordinates [57, 58]. Mallat *et al.* proposed innovative descriptors based on the the scaling wavelets transformation [59, 60]. The similarity distance descriptors describe the distances between the atomic environments [56, 61, 62]. Sometimes, deep learning on a specially designed neural network can be used to construct the descriptor itself [63, 64, 65, 66].

iii. the fitting algorithm is performed in the descriptor space and the (statistical) ML procedure of the fit defines the performance and limitations of the potential. The relationship between atomic energies and components of the descriptors can be linear [67, 68, 69, 70, 54, 49, 71] or highly non-linear, which are based on neural networks (NN) [53, 72, 73, 74, 75] or kernel methods [76, 77, 78, 79, 80, 81, 82, 83] (it should be noted that a linear kernel is equivalent with a linear regression). Some of the kernel models are formalized in the ever-growing field of the statistical on-the-fly learning methods [81, 83, 84], while the others are built in the form of potentials such as Gaussian Approximation Potentials (GAP) [55, 85]. The GAP is the most robust and commonly used version.

The highly non-linear methods are suitable to interpolate multivariate functions while for small training databases they show rather poor performances in the extrapolation regime. However, one can overcome this inconvenience by a well-chosen regularization or by constantly increasing the components of the database.

Linear ML (LML) models have some interesting advantages. These models are very stable: they do not behave awfully wrong outside their fitting range and they have few parameters and can be fitted with relatively small training datasets. The linear ML model does not imply a linear relation between the phase space and the observable. Any non-linear regression becomes linear if the domain of the regression function is projected into a space with a sufficiently large number of dimensions. The coefficients of such a potential are determined using weighted linear regression against the training database in the descriptor space. Thus, LML potentials offer a good tradeoff between accuracy and computational efficiency. The main advantages of this method (compared, for instance, to kernel methods) is that the size of the training database does not affect the numerical cost of the potential. The LML potential is only defined by the set of $D + 1$ parameters, with D being the dimension of the descriptor function.

Computational cost and accuracy of ML potentials depend on several factors that are contingent on the underlying ML model and type of atomic descriptor. Similarly to any conventional potential, the numerical efficiency of ML potentials scales with the number of atoms N. The numerical cost of kernel potentials additionally scales with the number of local atomic environments in the training database. The kernel GAP and LML potentials, which are based on spectral

descriptors, are respectively, four and two orders of magnitude slower than EAM potentials [49].

The LML method is relatively simple to implement. Any idea of potential suppose that the total energy of the system is the sum of local energies, of each a atom, i.e. $E = \sum_a \epsilon_a$. Using the LML formalism, each local energy is linear proportional to the descriptor components $\epsilon_a = \beta_0 + \sum_k D_k^a \beta_k$. β are the $D+1$ parameters of the potential and D_k^a is the k^{th} component (among D) of the descriptor on the a^{th} atom. From this formulation of energy, the forces and the stress of the system can be deduced. The LML potential in materials science was originally introduced by Thompson and co-workers [67, 68, 69]. A similar regression algorithm was also employed using tensorial descriptors [57, 58] or hybrid descriptors proposed by Goryaeva et al [49]. An extension of the LML, in order to capture the hidden aspect of the complex energetic landscape, is the introduction of quadratic flavour with strong precondition given by the LML fit. In this formalism we fit only the error between the DFT values and LML fit by using a quadratic coupling in the components of the descriptors $\epsilon_{DFT}^a - \epsilon_{LML}^a \sim \sum_{k,k'} \beta_{k,k'} D_k^a D_{k'}^a$. This model has $1 + D + D^2$ parameters and will be called Quadratic Noise ML (QNML), hereafter. This procedure ensure a similar transferability of LML and QNML potentials in spite of the non-linear character of the last.

A typical fit for a LML potential for W is presented in the Figure 4. The fit is performed on the extensive databases containing more that 100 000 atomic configurations in various environments, such as, vacancies, interstitials, dislocations, stalking faults, MD snapshots etc (similar to the database used in the study [51]). The LML fit provides the values of the mean average error (MAE) of energy per atom, force and virial stress below 5 meV, 60 meV/A and 12 meV/A^3, respectively. The QNML potentials have the MAEs that are more than twice smaller than the corresponding values from LML. To our knowledge, there is no traditional potential able to reach such low values of MAE.

The low value of MAE from fit ensures accurate potentials with respect to the data included in the fit. The properties that are known to be critical within EAM formalism, such as, the binding energy of the di-vacancy [48, 86, 87] or the shape of the Peierls barrier of the screw dislocation are easily fitted by ML potentials. Di-vacancy in metals of the group VI B has an unusual energy landscape [86]. In W, the first nearest neighbour vacancy is slightly repulsive or attractive depending on DFT calculations or exchange-correlation functional while the second nearest neighbour configuration is strongly repulsive [88, 86, 87]. The same tendency is observed for all elements of VI B group and is not the case for V B metals and Fe, where the most stable configuration of di-vacancy is the second nearest neighbour configuration. As predicted by the above DFT calculations, the binding energy of the di-vacancy in W in the first and the second neighbour configuration is negative in all ML potentials developed until now: LML, QNML or GAP. It is worth mentioning that with a small exception [48] there is no EAM potential, which is able to reproduce such a behaviour. It should be noted that in all developed ML potentials the information of repulsive di-vacancy was included in the fitting database.

Figure 5 compares the ability of semi-empirical potentials and ML potentials to compute the migration barrier of tri-vacancy clusters. The saddle point of V_3 is very low 1.15 eV compared to the migration barrier of $V_{1,2}$ [48], around 1.7 eV. For V_3, LML and QNML have rather good transferability and provide the right migration barrier, both in terms of energy and single saddle-point shape, whilst for the GAP class potential the error reaches up to 60% with the barrier having an unphysical shape (Figure 5). The highly non-linear character of GAP formalism yields a poor transferability. Figure 5 shows that in this extrapolation regime some of the EAM potential can perform even better that the GAP potentials. In order to improve the performance of GAP potentials in such cases, it is essential to enrich the training database. The missing configurations can be revealed at the stage of the database design using the distortion scores based on outlier analysis of the database [54]. This method was recently demonstrated to be very efficient for a similar problem with GAP potentials for Fe [54]. The straightforward solution to alleviate this drawback is to include the saddle point configurations of V_3 migration to the training dataset. A big error in migration barriers will have a strong impact on the predictions of defect kinetics under irradiation and interpretation of processes during resistivity recovery experiments. The stage IV will be strongly impacted by the fast diffusion of the vacancies clusters V_n with $n > 2$ affecting the prediction of the size and the density of vacancy clusters at temperatures higher than 300 K.

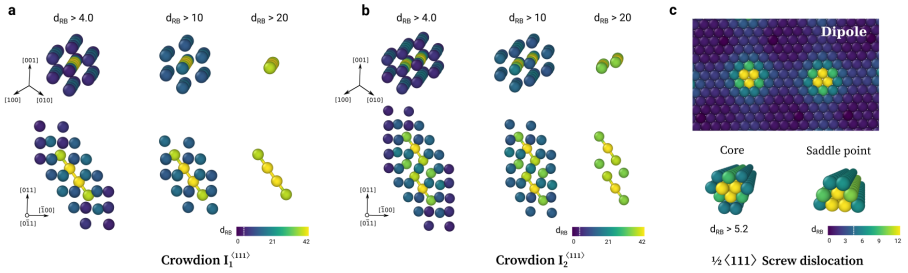

Figure 6: The structures of defects detected in bcc W using distortion score of local atomic environments based on robust MCD statistical distances d_{RB}: (a,b) $I_{1-2}^{\langle 111\rangle}$ crowdions, (c) $\frac{1}{2}\langle 111\rangle$ dislocation core and the saddle point structure when gliding in $\{110\}$ plane. The structures of crowdions (a,b) are "stratified" according to the distortion level of nearest defect environment

2.5.2. ML structural analysis

Present-day ML potentials allow accurate simulations of defect nucleation, recombination, migration and transition at the atomic scale. However, extracting the relevant information about defects and their collective behavior from atomistic calculations remains a challenge and requires processing enormous amounts of data. In particular, analysis of radiation induced damage requires a lot of effort and implies using several different methods for detection of different types of defects. A recent study [54] proposes a universal strategy for defect

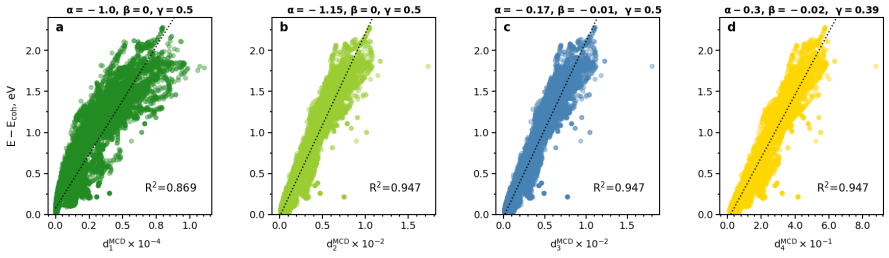

Figure 7: Correlation of the local energy from W-LML potential with various statistical distances that were proposed in Ref. [54]. The subplot (a) illustrate the standard MCD / Hotteling's T^2 estimator; (f, g, h) correspond to the variations of statistical distances inspired by QM.

detection based on statistical distances provided by outlier detection models, like Minimum Covariance Determinant (MCD). In this approach, each atom is characterized by a distortion score that describes a statistical distance from a reference distribution in the feature space of atomic descriptors. The reference distribution can be constructed from LAEs of a defect-free crystalline system at a given temperature or from a subset of atoms of particular interest (e.g. a particular defect structure). Constructing a training data set with thermal noise allows to avoid sensitivity of the defect detection model to atomic perturbations, a common shortcoming of conventional geometry based methods. Based on the local distortion scores, structural defects are identified as atoms-outliers deviating from the bulk structure. The defect detection strategy using the distortion score is universal, i.e., it performs well for defects of a different origin and the same technique can be applied for the detection and analysis of dislocations, interstitial atoms and vacancies. The detected clusters of atoms-outliers include the defect itself and its nearest atomic environment. Figure 6 illustrates the structures of crowdions and screw dislocation cores detected in W. The difference in magnitude of the distortion scores within the outlier cluster enables the stratified description of the defect and allows to distinguish the zones with different level of atomic distortion (as depicted for crowdions in Figure 6a,b). The atoms forming the defect are characterised by bigger distances d_{RB} compared to their nearest environment.

Interestingly, when computed with respect to the distribution of the underlying bulk structure, distortion scores exhibit an intrinsic correlation with local atomic energies. This correlation is enabled by a similitude between the formalism that describes the local atomic energy of materials in quantum mechanics (QM) and the statistical distances based on sample covariance matrix (see Ref. [54] for more details). Figure 7 illustrates a correlation of the local energies in W with various statistical distances that use different weights, such as powers of eigenvalues of the sample covariance matrix. The remarkable correlations with $R^2 > 0.9$ allow considering distortion scores as a surrogate model for local atomic energies. Moreover, the stratified definition of defects via distortion scores, can be used to identify the atoms with the most important contribu-

tion to the mean force of the system. This strategy can be used to accurately reconstruct the migration barriers from the mean force calculations [54]. Such an approach is of particular interest for defect localization in the simulations like QM/MM, where the definition of total energy is ambiguous. The distortion score coupled with outlier detection ML techniques can also serve to establish a qualitative criterion for transferability / reliability of kernel ML potentials (e.g., GAP) for modeling a given defect structure.

3. Analysis of Microstructural evolution

This section describes recent advances in both interpretation of experimental observations, for example in counting objects in Transmission Electron Microscopy (TEM) micrographs or clustering in Atom Probe Tomography (APT), which produces the reliable data sets needed for simulations to compare against, and the advancement of the computational techniques, particularly those based on Monte Carlo, that are now able to produce experimental-like statistics. Section 3.1 below discusses the challenges associated with linking the short timescale modelling of damage production to microstructural evolution that happens on experimental timescales before Section 3.2 summarizes the available experimental observation techniques, and 3.3 describes how these powerful techniques can be used to interpret the interaction of defects. The next subsection (3.4) describes how the defect statistics obtained from advanced observations of irradiated materials can now be compared to statistics obtained from kinetic Monte Carlo (kMC) simulations, allowing understanding that neither could provide alone. Section 3.5 reviews APT and describes the latest analysis techniques and their application to understanding segregation and clustering in irradiated materials. Recent simulations of segregation are then described (Section 3.6) before the section concludes with a discussion (3.7) of the approaches that can link microstructure statistics to the macroscale, for example by considering the accumulated volume change induced by defects.

3.1. Relating damage production to microstructure

The production of defects by energetic particles, such as ions or neutrons, occurring on picosecond time scales, can be studied by MD methods as outlined in the previous section. However, going beyond the nanosecond timescales with MD, especially when multi-million atom calculations have to be considered, is still not feasible. At the same time, there is no experimental technique that can provide information on the time and length scales of a single cascade event. Therefore, we are still lacking a direct comparison between primary damage obtained from MD and experimental observations. Methods such as kinetic Monte Carlo (kMC) and rate theory or cluster dynamics are the approximations that are often used to expand both the time and length scales well beyond the nanoseconds and nanometer capabilities of MD, to enable comparison with microstructures observed experimentally.

Understanding the connection between primary damage and microstructure developed for a given irradiation condition is probably one of the main outcomes

that these tools can provide. Currently, ion implantation is commonly used as a means to study defect production and to reduce the cost and difficulties that involve neutron irradiation. However, the use of ion beams to understand radiation damage produced by neutrons must be done with a careful analysis of their differences and limitations, as has been recently described by Zinkle and Snead [89]. In certain cases, a fairly good agreement between the microstructure produced by neutron and ion irradiation has been obtained, considering a temperature shift to account for the differences in dose rate [90, 91]. However, some controversy still remains. Is a temperature shift applicable to all cases? Can ions be used, in general, for emulating neutrons or just as a means for model validation? What is the significance of stress fields affecting the evolution of microstructure in a thin layer exposed to ion irradiation? Regardless, understanding damage production and microstructure evolution requires using a suitable physically justified models that can match experimental conditions, and kMC models in this case have advantages in comparison with direct MD simulations.

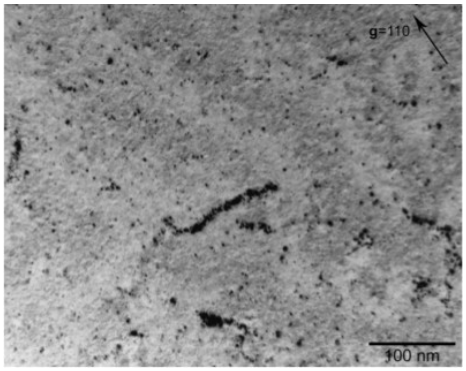

Figure 8: Example of TEM characterization of damage produced by 500 keV Fe^+ irradiation of a UHP Fe thin film at room temperature and 0.5 dpa. From Ref. [92], reprinted with permission from Elsevier.

3.2. Direct observation of microstructure

Changes in the microstructure of metals due to irradiation can be characterized by a series of experimental techniques such as TEM, Positron Annihilation Spectroscopy (PAS), APT or Small Angle Neutron Scattering (SANS). From all the different techniques TEM is arguably the most widely used in the evaluation of microscale damage of fusion materials. TEM can provide information about concentration of defects, defect size distributions, defect nature (vacancy or interstitial type) and defect type (loop and their orientation, voids, etc.). Figure 8 shows an example of the microstructure observed under TEM of a UHP thin film of Fe irradiated with 500 keV Fe^+ ions at room temperature and 0.5 dpa. In this case, decoration of a dislocation with defects produced by the irradiation can be observed. The majority of the defects here are loops of $a_0\langle 100\rangle$ type [92].

Moreover, *in-situ* TEM enables performing dynamic observations of microstructural evolution during annealing and/or irradiation. This technique has shown that phenomena such as one-dimensional diffusion of self-interstitial clusters, predicted initially by computer simulations, indeed occur in metals [93]. Figure 9 shows the diffusion of a $5.9\,nm$ diameter $\frac{1}{2}[11\bar{1}]$ loop in ultra-pure Fe observed by *in-situ* TEM at $575\,K$. In this case loops were produced by high-energy electron irradiation.

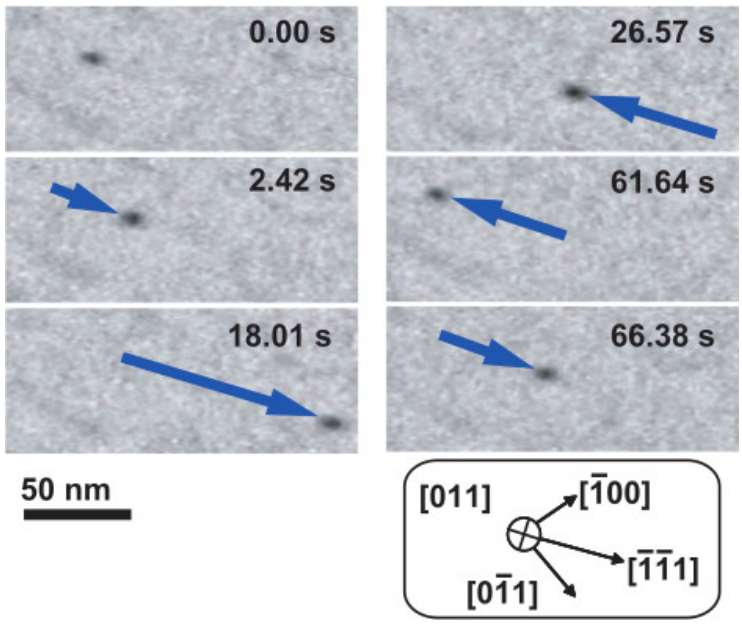

Figure 9: One dimensional diffusion of a $\frac{1}{2}[11\bar{1}]$ loop in ultra-high purity Fe at 575 K observed using *in-situ* TEM. From Ref. [93], reprinted with permission from AAAS.

3.3. Trapping and interaction between defects

There are discrepancies as to the migration energies measured experimentally and those obtained in the simulations. Despite the significant experimental and theoretical effort devoted to elucidating the source of this discrepancy, there is still not a completely satisfying answer. Carbon or other impurities, coupled to vacancies, have been proposed as possible traps for the rapidly diffusing interstitials in iron [94, 95].

Elastic interactions also result in the self-trapping of defects produced by irradiation. The formula needed to find the elastic interaction energy between two defects, A and B, in the far field limit where their separation is greater than their characteristic size, is both simple and elegant [30, 32]:

$$E_{\text{int}}^{A-B} = P_{ij}^{(A)} \left(\frac{\partial}{\partial x_j} \frac{\partial}{\partial x_l} G_{ik}(\mathbf{x}) \right) P_{kl}^{(B)}, \tag{3}$$

	Iron	Molybdenum	Tungsten
$\frac{\Omega_0^2\mu}{4\pi(1-\nu)}$	5.0	21.8	27.0
$\frac{\Omega_0^2\mu(1+\nu)}{6\pi(1-\nu)}$	4.3	23.1	19.1
$N^\star_{\mathrm{loop-loop}}$	32	6	7
$N^\star_{\mathrm{loop-void}}$	2210	97	102

Table 3: Elastic constants for interaction between nano-scale defects. The first row is for loop-loop interactions (equation 4), and the second for loop-sphere (equation 5), in units of eV/Å^3. Critical sizes for a defect placed 2nm from a 50-interstitial loop are given where the interaction energy reaches 1 eV.

where $P_{ij}^{(A)}$ and $P_{kl}^{(B)}$ are the dipole tensors of the two interacting defects. These dipole tensors can be computed by integrating the stress that the defect produces in a simulation cell, over the volume of the cell [96, 97] as $P_{ij} = -\int_V \sigma_{ij}(\mathbf{r})\mathrm{d}^3\mathbf{r}$, and $G_{ik}(\mathbf{r})$ is the elastic Green's function that we used earlier when evaluating the stress field of a defect using equation (1).

In the isotropic elasticity limit, we can go further and derive closed form expressions for the scaling laws determining the elastic interaction between defects [98]. For a pair of dislocation loops whose centers are separated by r, the energy of elastic interaction is

$$E_{\mathrm{int}}^{\mathrm{loop}A-\mathrm{loop}B} = \frac{\Omega_0^2\mu}{4\pi(1-\nu)}\,\frac{1}{r^3}\,N^{(A)}N^{(B)} \times (\text{ angular terms }), \tag{4}$$

where $N^{(A/B)}$ are the number of point defects in the loop, Ω_0 is the atomic volume, μ is the shear modulus and ν the Poisson ratio. For the interaction between a loop and a spherically-symmetric point defect, such as a spherical void [98],

$$\begin{aligned} E_{\mathrm{int}}^{\mathrm{loop-void}} &= \frac{\mu A b \Omega_{rel}}{6\pi r^3}\frac{(1+\nu)}{(1-\nu)} \times (\text{ angular terms }) \\ &= \frac{\mu\Omega_0^2}{6\pi}\frac{(1+\nu)}{(1-\nu)}\frac{N(\Omega_{rel}/\Omega_0)}{r^3} \times (\text{ angular terms }) \end{aligned} \tag{5}$$

where Ω_{rel} is the relaxation volume of the spherical defect, A is the area of the loop and $b = |\mathbf{b}|$ is the magnitude of the Burgers vector of the loop.

The experimental evidence for elastic interactions being a driving force for microstructural evolution is overwhelming, in loop rafting [99, 100, 101], self-trapping [102], and even the observation of strain fields in weak-beam-dark-field TEM. With equations 4 and 5 we can test where elastic interactions are important in simulations more generally. For an $a_0/2\langle 111\rangle$ loop containing 50 point defects, just visible in the TEM, we can find the minimum size defect $N^\star$ required to produce an interaction of 1 eV at a distance of 2 nm. For the relaxation volume of a void we can use the capillary approximation $\Omega_{\mathrm{rel}}/\Omega_0 \simeq -\alpha N^{2/3}$, with α fixed by the vacancy relaxation volume [16, 17]. These critical sizes are given in Table 3. We see that a TEM visible loop is strongly interacting

with small interstitial clusters at 2 nm separation: for iron the critical size is 32 interstitials, for tungsten only seven. Loop-void interactions are slightly weaker, and the critical void size for the same 1 eV interaction is over 2000 vacancies (a 3.7 nm diameter void) in iron, or 100 vacancies in tungsten. This simple calculation suggests elastic interactions should never be ignored in simulations when interstitial defects are of TEM visible size. Furthermore, the strength of elastic interaction is proportional to the product of relaxation volumes of defects, and for dislocation loops it scales quadratically with loop diameters. This suggests that the role of elastic interactions increases rapidly with the characteristic spatial scale of the microstructure.

Besides the direct observations performed using *in-situ* TEM, one-dimensional diffusion of dislocation loops can be inferred from the microstructure developed under irradiation. One effect is the existence of defects beyond the end of range of damage and the loss of precipitate coherency in this region which is believed can be explained by a combination of 3 dimensional and 1 dimensional diffusion of defects [103, 104]. A second piece of evidence comes from the presence of a region with enhanced void formation close to a void denuded zone near a grain boundary or a surface. One example of such behaviour is shown in Figure 10) for Fe3Cr irradiated with a dual beam of 8 MeV Ni and 3.6 MeV He up to 30 dpa with a 0.1 appm He/dpa rate and at $500^\circ C$ [105]. When the density of defects become high and the effective sink strength increases above a certain value ($\approx 1 \times 10^{14}/m^2$) the one-dimensional migration of defects is no longer observed.

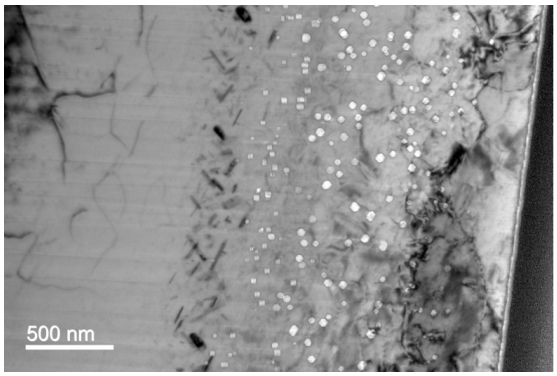

Figure 10: Defect denuded zone and enhanced void region in Fe3Cr irradiated with a dual beam of 8 MeV Ni and 3.6 MeV He up to 30 dpa and 0.1 appm He/dpa at $500^\circ C$ [105].

3.4. Statistics of defects and Monte Carlo models for microstuctural evolution

Calculations can be performed to simulate microstructures produced under irradiation. In principle, MD, with appropriate interatomic potentials can provide information about the damage produced by the irradiation. In W, where large clusters of defects visible under TEM are formed in a single cascade, a fairly reasonable agreement can be established in the low dose limit between

TEM measurements and MD simulations [27, 106]. This may also be the case in pure Fe, though the defects produced in cascades are smaller and consequently more difficult to detect. MD simulations [107] suggest a power-law size-frequency distribution of defects produced in Fe, albeit with a higher power law exponent than seen in W, so that few interstitial clusters with size > 50 point defects are created, fewer than 0.001 per Primary Knock-on Atom (PKA). This size is at the limit of TEM detection, but they have been recently observed even at very low dose (0.0015 dpa) in ultra-high-purity Fe [108]. The apparent contradiction between this result and earlier studies suggesting that cascade overlap is necessary to observe defects in heavy-ion irradiated iron [109, 110] may be due to the difficulty of making a positive identification of a loop smaller than 1 nm [111], or because small loops are inherently extremely mobile on the experimental time-scale [112] and respond more readily to elastic image forces induced by the proximity of the surface in a thin foil experiment [113].

In this case, as mentioned above, and in others, it is necessary to make use of kMC and rate theory or cluster dynamics models. For recent descriptions of these methods see Refs. [114, 115]. The first passage, rate theory and cluster dynamics models have also been integrated into phase-field models to deal with fast one directional diffusion and the effect of defect mean fields on microstructure evolution [116, 117, 118]. Although most phase-field models are qualitative (or are not accurate in terms of length scale and the input of thermodynamic and kinetics properties of defects) there are some good progress in more quantitatively describing the thermodynamic and kinetic properties of defects in irradiated materials. For example, a thermodynamically consistent model with the input from atomistic simulations and AKMC has been proposed [119, 120]. Finite element method and phase-field approach have also been coupled to understand the effect of microstructure evolution on thermomechanical properties degradation and material performance [121, 122].

Rate theory or cluster dynamics can provide information about defect concentration and size distributions but, by being mean field methods, they are not able to capture the individual defect structures and the spatial heterogeneity of the damage produced under irradiation. KMC methods, however, while using essentially the same input parameters as cluster dynamic models, are able to follow individual defects and therefore the microstructure predicted can be directly compared to that obtained experimentally, in particular to TEM characterization. Figure 11 shows an example of an object kMC (OkMC) simulation of an 85 nm thin film of Fe irradiated with 500 keV ion (representative figure from OkMC, if possible similar to Figure 1).

A direct comparison between OkMC and TEM is possible, but there are issues which must be accounted for when considering defect count or average size. Some effects can be corrected simply, while others require a much more careful consideration of the thermal history of a sample.

It is regularly quoted that there is a minimum defect size observable in a TEM [111, 106, 123, 124]. While this is true, and agrees with the results obtained

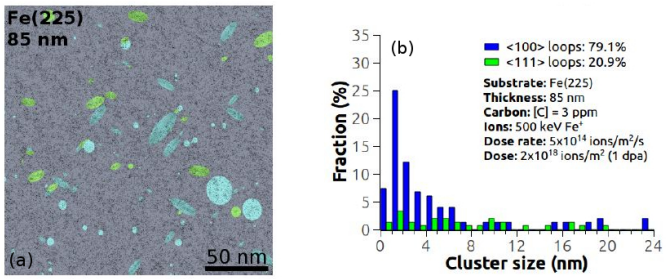

Figure 11: Example of results from an OkMC calculation of 500 keV Fe irradiation of pure Fe (a) projection of all defects along the sample thickness (b) histogram of defect sizes. Image courtesy of JP Balbuena.

using X-ray diffraction and other means of microstructural examination, strictly speaking this is the limit determined by the aperture, and small defects slightly larger than this small size limit may be undetectable due to the faintness of their intensity profile. This aspect of TEM observations is problematic from the perspective of making a comparison between theory and experiment as it means that the confidence interval for a count of small defects is very broad compared to that for large defects. It is also unlikely to be a normal distribution, so that reporting a sample standard deviation could be misleading. Sand *et al.* [125] estimated the uncounted small defects by looking at the distribution of intensities of defects as a function of size. From this they determined that the count of the smallest defects (1-2 nm) might be low by a factor of 5, in broad agreement with Refs. [106, 123, 124]. Importantly, including this confidence interval brought their theoretical estimate for the number of observable defects in line with experiment, where a simple 'square-root-N' estimator of the error in the observed count would not have done.

A second effect which may be prevalent in TEM observations of higher damage dose is the systematic reduction in count due to the shadowing of one loop by another - simply put if two dislocation loops happen to almost coincide along the viewing direction they cannot be individually resolved. We can estimate when this effect becomes significant. If all defects image with a 2d Gaussian profile with half width σ, then they will be indistinguishable when there is no dip in intensity in a line profile between their peaks. This happens when their separation is less than 2σ. If the defects are placed randomly and homogeneously, then the number found per unit area will be Poisson distributed. The probability that adding one defect will increase the distinct spot count is the probability that there are no neighbors within a circle radius 2σ, ie $p_0 = \exp[-4N\pi\sigma^2/A]$, where N is the true spot count and A the micrograph area. The probability that adding one defect will *decrease* the distinct spot count by linking an existing pair is approximately the probability there are two neighbors in the circle radius

2σ, ie $p_2 = 1/2\,(4N\pi\sigma^2/A)^2\,\exp[-4N\pi\sigma^2/A]$. Thus

$$\begin{aligned} \frac{\mathrm{d}\langle N_{\mathrm{count}}\rangle}{\mathrm{d}N} &\simeq \exp\left[-\frac{4N\pi\sigma^2}{A}\right]\left(1-\frac{1}{2}\left(\frac{4N\pi\sigma^2}{A}\right)^2\right) \\ \text{so} \qquad \langle N_{\mathrm{count}}\rangle &\simeq N\,\exp\left[-\frac{4N\pi\sigma^2}{A}\right]\left(1-\frac{2N\pi\sigma^2}{A}\right). \end{aligned} \tag{6}$$

The expected observed count rises linearly with the number of defects until they are so dense they start to overlap. Then the observed count reaches a maximum before falling again.

A third possibility is that not all loops are visible under the imaging conditions because of the $\mathbf{g}\cdot\mathbf{b} = 0$ invisibility criterion [111]. Again, a simple correction for this factor is possible if the range of $\mathbf{g}$ vectors sampled by the experiment is known. Prokhodtseva *et al.* [126] suggested how one can compute the relative proportions of $a_0/2\langle 111\rangle$ and $a_0\langle 100\rangle$ loops using a statistical method based on the invisibility criterion and a range of $\mathbf{g}$ vectors. The same argument can be used to estimate the invisible fraction, if it may be safely assumed there is no bias due to the crystallographic orientation of the foil and no long-range ordering of Burgers vectors.

A fourth possibility we can consider is that some defects may be invisible in the TEM due to their depth. This can occur when the extinction distance- $\xi_{\mathbf{g}} = \pi V/(\lambda\Gamma_{\mathbf{g}})$, where V, λ and $\Gamma_{\mathbf{g}}$ are the unit cell volume, electron wavelength and structure factor respectively- is smaller than the foil depth. In this case there are periodic layers where the incident and reflected electrons exhibit beats in intensity. This may be used to estimate the fraction of missing defects if a simulated depth profile of defects is known.

The possible corrections to observed microstructural metrics offered above may be best employed as possible systematic biases and error bar contributions to the simulated data, where the (quite broad) assumptions may be tested or corrected. But work to make the comparison between simulation and experiment has recently been made more quantitative by a systematic approach to the confidence intervals in TEM observations. Mason *et al.* [127] considered the possibility that an automated computer analysis of microstructure [106, 128] might be making type-I errors - false positive identification of defects. This was done by constructing a t-statistic, $t^\star = \bar{I}/(\sigma/\sqrt{n})$, where $\bar{I}$ is the average intensity of a spot covering n pixels given the background noise level σ. $t^\star$ is high when the spot is large and bright and low when the spot is small and faint. This can be done for each detected spot but can also be done if the same code is forced to find spots in an *unirradiated* micrograph. By comparing the distributions of the two, it is possible to determine the confidence interval for false positives. This gives a meaningful error bar to the smallest, faintest spots, but moreover gives a probability distribution function for the experimental observation, see Fig. 12. These experimental results therefore can be directly used in standard statistical hypothesis testing against simulated results.

A final challenge comparing OkMC to TEM can be much harder to correct for. A defect observed *in situ* in the TEM must be stable over the experimen-

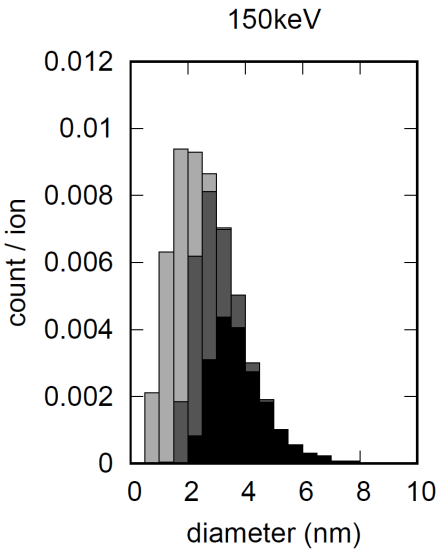

Figure 12: Automated TEM analysis of 150 keV self-ion irradiation of UHP tungsten at cryogenic temperature [127] gives a size-frequency distribution. The shading of the bars indicate significance levels ($\alpha = 0.001$ (black) , $\alpha = 0.25$ (mid-grey) , and $\alpha = 0.15$ (light grey). The confidence interval for small, faint defects is very wide, which may help matching experiment to simulation. Figure reproduced from Ref. [127].

tal timeframe. But the converse is also true: a defect which is not stable over the experimental timeframe will not be observed in the TEM. In the case of a fast migrating species, such as a bcc crowdion in a perfect pure tungsten, the diffusion constant can be as much as $10^4 \mu\text{m}^2/\text{s}$, even at liquid nitrogen temperatures [129]. The time taken to diffuse to a surface or other sink is likely to be very small compared to the experimental time. But consider the effective diffusion coefficient of such a crowdion in low carbon concentration background. We might expect the diffusion constant to be reduced by order $\exp(-E^b/k_B T)$, where E^b is a typical binding energy, say 0.62 eV in W [130]. The room temperature diffusion constant is reduced by eleven orders of magnitude at room temperature, down to 10^{-1} nm^2/s. A defect with this diffusion constant would hardly appear to move in an *in situ* TEM movie, but over six months (a reasonable cool-down period after neutron irradiation) it may move over a distance of order 1 μm. It is therefore vital that not just the flux and fluence are reported for *ex situ* TEM studies, but also that the time the sample was kept at room temperature is recorded and accounted for.

3.5. Irradiation-induced segregation and chemical decomposition

Irradiation can also induce local changes in chemical composition such as segregation of alloying elements or precipitation. APT has proven to be an excellent method to obtain detail information of these phenomena in irradiated

materials. Recently, there has been some success in comparing the results from such experiments directly to AkMC (see, for example, [115]), although there are still outstanding questions as to the appropriateness of comparisons due to the (currently unavoidable) limitations of the spatial and chemical resolution of APT.

One significant limitation in our understanding of point defect mobility and the development of dislocation loops and cavities, is the presence and role of impurities. The presence of carbon, nitrogen, phosphorous, silicon, and other impurities are nearly systematically overlooked. Yet APT consistently shows that these elements are present, form small clusters, and segregate to structural defects. Heavy ion irradiation experiments have also been known to introduce significant levels of impurities [131]. For alloyed systems, APT has provided a unique perspective on solute clustering and segregation phenomena in a wide range of irradiated alloy systems. The technique also has played a unique role in understanding the role of dose rate on phase transformation, providing complementary information to the traditional TEM observations, generally focused on dislocation loop and void imaging and quantification.

As an example, several independent studies on the Fe-Cr system have recently converged and the results paint a detailed and coherent description of the effect of irradiation on phase decomposition in this particular system. Consistent with the very slow thermal diffusion kinetics of Cr in α-Fe [132, 133], precipitation of the α' phase under thermal aging exhibits notoriously slow kinetics, requiring tens of thousands of hours in the temperature range of 450-550 °C to be noticeable using conventional characterization techniques [134]. At lower temperatures, the kinetics of decomposition are too slow, leading to uncertainty on the phase diagram. Alternatively, microstructural APT data is available for a range of irradiation conditions, all performed at the same irradiation temperature of 300 °C, allowing direct comparison between experiments. Under neutron irradiation at dose rates lower than 10^{-7} dpa/s, nm scale α' precipitates have consistently been reported in binary Fe-Cr alloys with Cr contents greater than 9 at.% [135, 136, 137, 138, 139, 140] and in some commercial Cr-containing steels, e.g. [141, 142]. The increasing size and decreasing number density of the α' precipitates with dose are consistent with a coarsening behaviour [143]. The increasing number density of α' precipitate with increasing Cr content is also consistent with increasing precipitation driving force with increasing Cr supersaturation [135]. The observations are consistent with α' formation is accelerated by the increased point defect concentration and radiation enhanced diffusion (RED). The changes in α' and matrix compositions and increased Cr solubility measured for neutron irradiation at higher temperature (450 ° C) are consistent with those measured for thermally aged alloys at 450-550 ° C [143].

Under heavy ion irradiation, the lack of α' precipitates was systematically noted at high dose rates greater than 10^{-3} dpa/s [144, 145, 146]. At lower dose rates however, Cr-rich clusters and α' precipitates were observed, with microstructures strongly dependent on dose rate suggestive of decreasing role of cascade mixing [147]. Figure 13 illustrates the development of Cr clustering as a function of dose rate for neutron and ion irradiations performed at 300 ° C.

Using *in situ* He, Ne, and Kr irradiation with TEM observations, Harrison et al. found decreasing α' number density with increasing PKA energy at constant dose rate [148], further corroborating the role of high-energy-density cascades and sub-cascade formation leading to spatial and temporal cascade overlap and therefore increasing solute mixing. Unlike heavy ion irradiation at high dose rates, 100 keV He irradiation at dose rates between 10^{-4} and 10^{-3} dpa/s led to precipitation with the rate of precipitation increasing with dose rate [148]. Similarly, significant α' coarsening was reported during electron irradiation for increasing dose [149]. In these two cases, the higher dose rate increases the Frenkel pair production rate. However, because the recombination rate is not a linear function of dose rate, the overall point defect concentration increases, leading to RED and therefore accelerated α' precipitation. Recent modelling of the Fe-Cr system provides further support to the role of point defects and cascade mixing. Using AkMC, Soisson et al. reproduced the RED effect during low dose rate irradiation [150], while Ke et al. reproduced the effect of RED for neutron and electron irradiation and cascade mixing for high dose rate heavy ion irradiation using a phase-field approach [151].

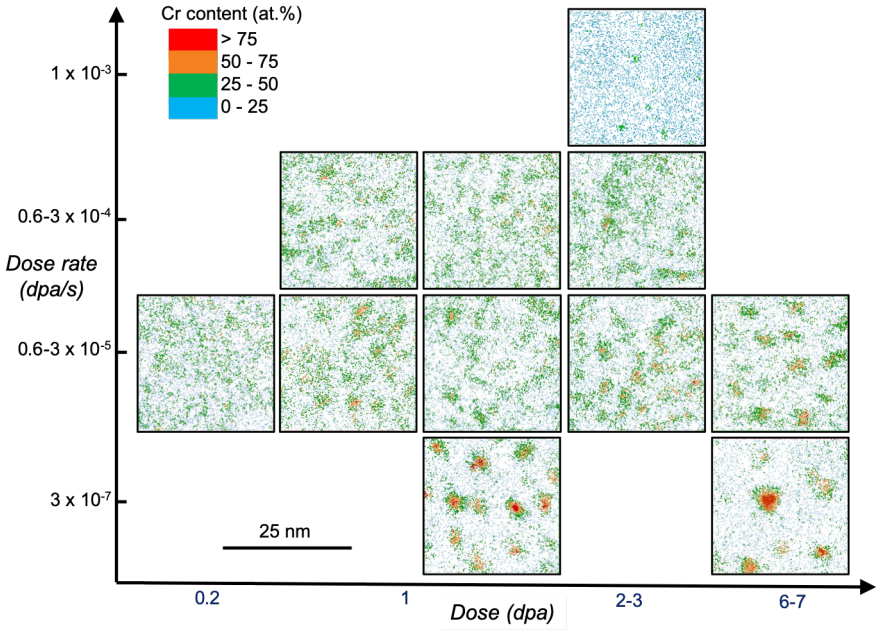

Figure 13: 2 nm thick atom maps from reconstructed APT volumes obtained after ion and neutron irradiations. Color gradient is associated with local Cr concentration measured in 1 nm diameter spheres. Adapted from [147]

These Fe-Cr studies naturally raise the question of microstructure stability or microstructural evolution for more complex alloys under irradiation. Similar to the observation that microstructural features (voids, dislocation, precipita-

tion) may have their own temperature and dose rate dependency [152], different stable and metastable phases within an alloy might have their own dependence due to different thermodynamic properties, differing point defect interactions, competition for point defects, etc. Such behaviour would challenge the use of heavy ions to reproduce neutron irradiation microstructures. However, understanding ion irradiation provides a unique opportunity to quantify individual phase stability.

While essential to our understanding of the chemical effects, the interpretation of APT data can also be subject to a number of potential limitations, similarly to the TEM challenges described above. The analysis of small solute clusters can be limited by spatial resolution and the accurate measurements of cluster composition. This issue has led to significant discussions regarding the composition of Cu clusters forming in irradiated low alloyed and stainless steels, e.g. [153], or the composition of nanoscale oxide particles in ODS alloys, e.g. [154, 155, 156]. Similar effects may be at play regarding the composition of nanoscale α precipitates in Fe-Cr alloys. The composition of α precipitates depends on a number of factors that include temperature dependence of the equilibrium composition, thermodynamic and kinetics factors that can affect the composition in the early times of formation when the precipitates are very small, i.e. < 2 nm. In addition, mixing effects could result in lower the Cr precipitate composition. Analyzing all the reported APT data on α in Fe-Cr alloys, Reese et al. argued that APT artefacts further lower the precipitate composition for the smaller precipitates sizes [143]. Conversely, Hatzoglou et al. showed that the error introduced by trajectory aberrations is less than 5 at.% [157]. This model however does not consider surface diffusion and local atomic rearrangement that would further dilute the apparent cluster composition [158, 159]. Quantifying the spatial and chemical accuracy and errors in APT data remains a significant topic of research, with recent efforts focused on the development of physics-based models to support the interpretation of APT data and its use for understanding complex microstructures as those observed in irradiated alloys.

Beyond cluster composition, the number density of clusters is an essential quantity to accurately measure in order to develop hardening models. The APT community has traditionally used relatively simple clustering identification algorithms. The so-called friend-of-friend algorithm, first introduced to the APT data by Hyde et al. [161] involves a set of parameters that define what a cluster is: a threshold distance that defines whether 2 atoms are part of the same cluster, a minimum cluster size in terms of the number of atoms within a cluster, and the number of nearest neighbor solute atoms on which the threshold distance is applied. This approach works very well for dilute solutes with clear clustering behaviour. However, its limitations in terms of subjective parameter selection and increasing identification errors for complex microstructures have led to significant results variability and at times erroneous interpretation of the data. The APT community has organized round robin experiments to understand and quantify the origins of quantification variability, raise awareness around the pitfalls, and establish standardized analysis and reporting habits [162]. To expand the range of available methods, new algorithms are also needed and should use

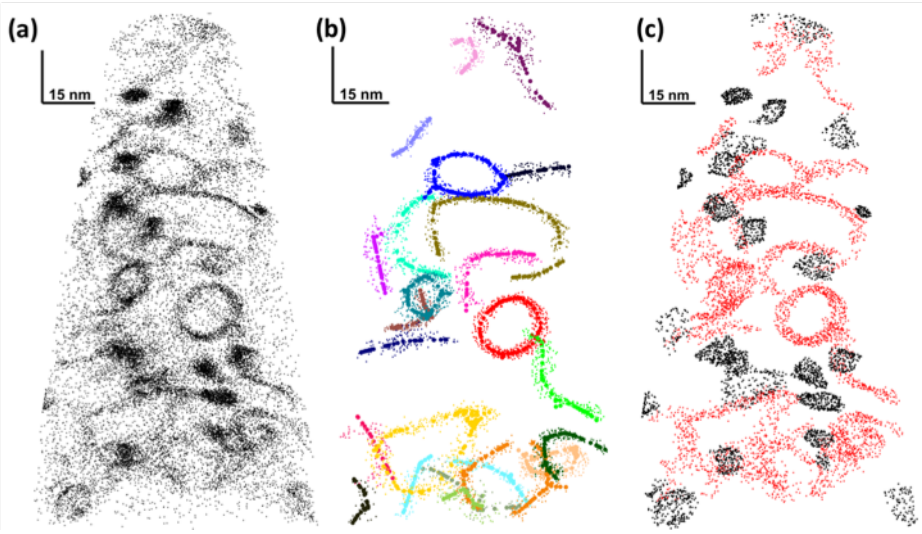

Figure 14: Automated cluster and dislocation loop analysis from APT data. (a) 3D reconstruction showing Si atoms only; (b) identification of individual dislocation loops and lines; (c) identification of Si rich clusters and decorated dislocation lines. From [160].

the advancements in data analysis methods developed in other scientific fields.

Following the first use of the DBSCAN algorithm for APT data by Stephenson et al. [163], Ghamarian et al. recently adapted the HDBSCAN and DeBaCl algorithms to the detection and quantification of solute clusters in APT data [164]. This approach can be applied to a wider range of microstructures by allowing clusters of different density and accounting for variable matrix density. Building on these algorithms, Ghamarian et al. also proposed an automated detection algorithm for dislocation loops that are apparent in APT data via solute segregation. This approach was recently demonstrated for dislocation loops that form in a proton-irradiated Alloy 625 and are decorated with Si [160]. Until now, such analysis was performed by hand and subject to significant subjectivity. Figure 14 illustrates the detection and classification of Si decorated features into two categories: dislocation loops and Ni_3Si clusters. Following the round robin recommendations, it is important to emphasize the need for thorough reporting of the analysis methods, including details of the algorithm and selection of relevant parameters. This information is not only essential for the reproducibility of the results, but also ensures that the analyzed results with their likely biases can be accurately interpreted by future researchers and data can be compared with future analyses, thereby optimizing research activities and limiting waste of research resources.

3.6. Transmutation-induced segregation of Re in W

A somewhat different picture is offered by the behaviour of Re solutes in W. Re forms concentrated solid solutions with W, resulting in commercially

available alloys with a significantly improved fracture toughness [165]. Between 300 and 600°C W-Re exists as a bcc solid solution up to Re concentrations of 15-to-25% atomic [166], after which the alloy goes through an intermediate precipitation region dominated by the formation of brittle σ and χ intermetallic phases [166, 167]. However, exposure of initially unalloyed W to moderate levels of mixed-spectrum neutron irradiation is seen to result in exceedingly high hardening levels, and severe degradation of the fracture toughness and the thermal conductivity [168, 169]. However, while inventory calculations have shown that the level of accumulation of Re in W under ITER-like conditions is approximately 0.1 at.% Re/dpa [170], independent irradiation tests to doses of less than 2.0 dpa conclusively show the formation of elongated Re precipitates in W with σ and χ structure [168, 171, 167]. While segregation in nominally subsaturated conditions is a common phenomenon under irradiation, the formation of Re-rich precipitates (as well as precipitates containing Os and Pt [172]) has been observed to take place homogeneously, not necessarily associated to defect sinks [166].

Recent models based on alloy cluster expansion Hamiltonians fitted to DFT results [166, 173] and coupled to detailed defect energetics calculations [174, 175] have revealed that a potential mechanism that can explain the formation of Re-precipitate precursors is the immobilization of solute due to mixed-dumbbell migration and clustering. DFT calculations have revealed a two-step process by which Re-W dumbbells alternate $\langle 111 \rangle$ translations with $\langle 110 \rangle$ rotations in such a way as to remain in the bound dumbbell configuration. In this fashion, Re atoms in the dumbbell are transported effectively along $\langle 100 \rangle$ directions [175]. Figure 15 illustrates the two-step process with the associated energy landscape (this mechanism can take place also for other transition metal solutes dissolved in W). Migration continues until W-Re dumbbells encounter (i) one another, forming immobile di-interstitials (or larger) clusters, or (ii) vacancies, resulting in a substitutional solute. This mechanism of Re by way of mixed-dumbbell migration – with W and Re atoms being transported in pairs – is consistent with the formation of non-compact Re clusters with Re concentrations approaching the stoichiometry found in σ and χ phases (20%-50% atomic). Another important aspect of this mechanism is that interstitial migration is rendered three-dimensional, as opposed to primarily one-dimensional as for pure self-interstitial defects. This is also consistent with an enhanced recombination and the suppression of the swelling peak in neutron-irradiated W-Re alloys compared to pure W [166].

The effect of the above mechanism on microstructural evolution and mechanical property degradation can be captured in kinetic reaction-diffusion models of the types discussed later in Section 4.2. In these models, Re transmutation is included as a valid microstructural transformation resulting from neutron irradiation. As shown in Figure 16, under these conditions, Re precipitates are seen to account for the majority of the hardening calculated in neutron irradiated W-Re alloys (with three different spectra), in agreement with experimental measurements. These results support the notion that segregation models of defect-solute co-evolution must include transmutation in cases where

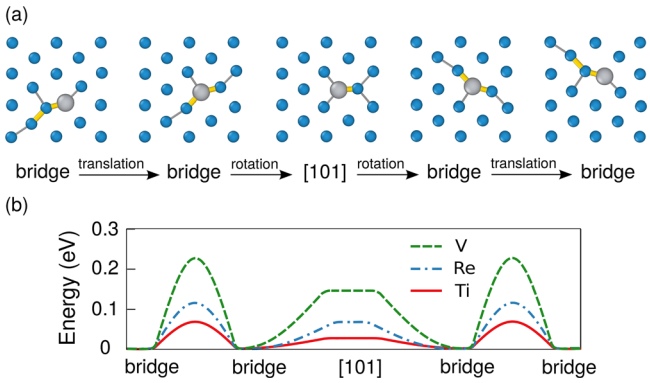

Figure 15: (a) Composite mechanism of migration of Re by alternate translation-rotation-translation steps between the dumbbell and 'bridge' configurations. (b) Associated migration energy landscape. Both rotations and translations display similar energy barriers. From [175].

its impact is crucial to predict and understand microstructural evolution under irradiation, see [166, 176].

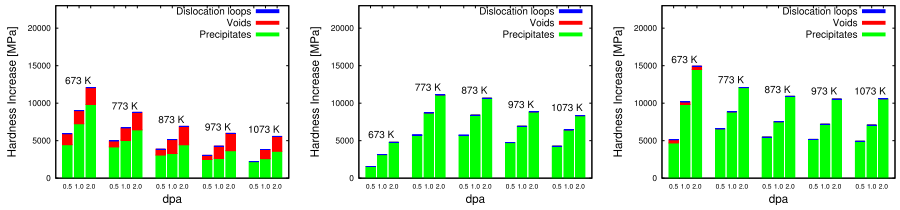

(a) DEMO. (b) HFIR. (c) JOYO.

Figure 16: Computed irradiation hardening levels obtained using a mean-field cluster dynamics approach due to the formation of SIA loops, voids, and Re precipitates in neutron irradiated W with Re transmutation. Results for (a) fusion, (b) mixed, and (c) fast neutron spectra are shown for comparison. From [177].

3.7. Macroscopic stress and swelling: from microstructure to continuum

New methods have been developed for transferring the information now available from microstructural evolution simulations back to making real-life engineering predictions about material swelling due to irradiation [178, 179]. Fundamentally, swelling is a property measurable with calipers - indeed, it is just a measure of the changing dimensions of a reactor component, but there are three possible origins to a dimensional change. The first is transport of material from the interior to the surface or to grain boundaries, leaving voids behind in the bulk and steps on the surface, or altered atomic arrangements in the grain boundary regions, formed by the atoms emerging by self-interstitial

defect transport from the bulk. The second is an effective change in lattice parameter produced by the homogeneous strain induced in a component with free surfaces due to the presence of defects in the bulk. The third one is the growth and coalescence of spatially homogeneously distributed self-interstitial dislocation loops, resulting in the formation of a grain-spanning dislocation network and new complete crystallographic planes, and giving rise to the overall expansion of the material [180]. This latter mechanism incorporates self-interstitial atom defects in the perfect crystal lattice, effectively removing them as 'lattice defects', and generating high residual concentration of vacancies, leaving them free to diffuse and coalesce into voids.

Historically only the first case, transport of material, and partially the third one, the formation of new atomic planes by dislocation climb, were considered in detail [19, 181, 182, 183, 184]. This approach is correct in the limit where all the microstructural features present are large. In this limit the relaxation volume *per vacancy* of a large void is zero, and the relaxation volume *per interstitial* of a dislocation loop is one atomic volume [33]. Therefore it is immaterial whether a large interstitial loop is trapped in the interior or at the surface, the total change of volume of the component can be found by a simple count of the number of vacancies in all the voids, which matches the total number of self-interstitials contained in large dislocation loops or in steps and atomic islands formed at the surface.

But in the limit where small, in comparison a certain chosen scale of microstructure, defects dominate internal stresses and strains, the treatment of swelling is far less obvious, and has only recently been elucidated in Ref. [185]. In the limit where defects can be homogenised and treated in terms of a field of continuously distributed density of relaxation volumes, it is possible to compute the resulting effects using notions of solid mechanics. For example, the body force acting on a volume of a finite element, $\mathbf{f}(\mathbf{r})$, can be written as a simple gradient of the *local* relaxation volume density of defects, $\omega_{\mathrm{rel}}(\mathbf{r})$, accumulated in the microstructure at a given location, i.e.

$$\mathbf{f}(\mathbf{r}) = -B\nabla\omega_{\mathrm{rel}}(\mathbf{r}), \tag{7}$$

where B is the bulk modulus of the material.[1] Using this equation, strains, stresses and swelling of arbitrarily complex components in a reactor can be computed given the internal microstructure [185]. Furthermore, since the scale of a reactor component is macroscopic, even gigantic defect structures forming under irradiation can be treated as microscopic, and hence the above equation has a very broad range of validity if viewed from the macroscopic perspective.

To parameterize equation (7), a comprehensive survey the relaxation volumes of point defects in bcc and fcc metals, computed using Density Functional

[1] In full tensorial representation, taking into account effects of anisotropic elasticity and the anisotropy of the structure of defects themselves, the above equation acquires the form $f_i(\mathbf{r}) = -\partial\Pi_{il}(\mathbf{x})/\partial x_l$, where the density of elastic dipole tensors of defects $\Pi_{il}(\mathbf{x})$ is defined in terms of dipole tensors of individual defects $p_{il}^{(a)}$ as $\Pi_{il}(\mathbf{x}) = \sum_a p_{il}^{(a)}\delta(\mathbf{x}-\mathbf{R}_a)$.

Theory, has been published recently [16, 17]. Relaxation volumes of clusters of defects and dislocation loops in tungsten, spanning the entire range of sizes of defect clusters, were explored in Ref. [33]. These studies show that the relaxation volume per an interstitial defect can be significantly greater than one atomic volume, $1.7\Omega_0$ in Fe and W, and the value only slowly decreases to $1\Omega_0$ in the limit where defects form large dislocation loops containing hundreds or even thousands of interstitial point defects. The corresponding relaxation volume per vacancy is approximately $-0.2\Omega_0$ (Fe) or $-0.3\Omega_0$ (W), and the relaxation volume per vacancy gradually vanishes in the limit where vacancies agglomerate in large voids [33]. On the other hand, vacancies forming dislocation loops exhibit a large *negative* relaxation volume, approaching minus one atomic volume per vacancy, $-1\Omega_0$. Hence, vacancy dislocation loops give rise to the much larger degree of elastic contraction of the material than quenched-in individual vacancies [20]. The above values show that there is effectively instantaneous volumetric swelling occurring in irradiated components due to the accumulation of the primary damage cascade, which gradually evolves as defects interact and recombine, and new defects form as a result of continuing exposure to irradiation. At low temperatures, where mobility of defects is suppressed, the density of defects and volumetric swelling gradually saturates as a function of dose [180].

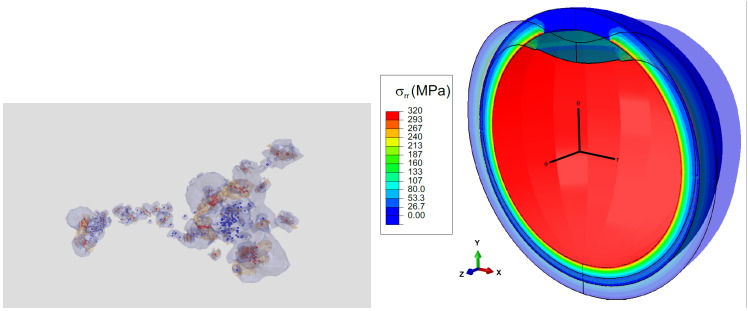

Figure 17: Left: stress isosurfaces induced by a typical 150 keV cascade in tungsten[27]. Vacancies (blue spheres) and interstitials (red spheres) are identified by a Wigner-Seitz cell analysis and isosurfaces of stress are indicated (yellow- trace of dipole tensor = +0.1eV, blue-trace of dipole tensor = -0.01eV). Right: Radial stress computed using the finite element method for a spherical model reactor pressure vessel with the cap of the sphere shielded[185]. These two calculations are linked together by the simple formula, equation (7), relating internal body forces to the density of relaxation volumes of defects in the microstructure of irradiated material. Figure reproduced from Ref. [185].

4. Microstructure to properties

This section reviews the recent efforts to take the final step in the multi-scale framework – using the simulations, modelling and experimental analysis to make predictions about the change in material properties in the fusion environment. After describing the challenges that need to be solved below, we

discuss (Section 4.2) the advanced simulation techniques being developed to overcome the limitations of the traditional techniques (MD, DFT, kMC, etc.). These include a kMC method applied in the semigrand canonical ensemble to study He segregation in irradiated W, the use of adaptive kMC (4.2.1) to study complex problems where transition states are not known in advance, and continuum methods such as stochastic cluster dynamics (4.2.2). After discussing the ongoing challenges of developing multiscale frameworks (Section 4.2.3), as exemplified by the modelling needs of a new generation of smart alloys, we discuss examples of new experimental characterisation techniques that are suitable for validating the predictions coming from the multiscale approaches (Section 4.3).

4.1. The fusion challenge

Exposure of first wall materials to fusion plasmas and their ensuing property degradation has long been recognized as one of the most important challenges facing fusion energy [186, 187, 188, 189]. The current ITER plan calls for a divertor design consisting of support structures (monoblocks) with plasma-facing components made out of W to withstand heat loads of 10-20 MW m^{-2} [190]. The behaviour of W-based components under such extreme conditions has been reported to involve surface erosion/exfoliation [191, 192], and the formation of quasi-porous, filamentous structures widely referred to as nanofuzz under high flux, high fluence plasma conditions [193, 194, 195, 196]. While the near plasma edge and material surface evolution have attracted and continue to attract a considerable amount of interest under the umbrella of plasma-materials interface (PMI) and plasma-facing materials (PFM) research programs, the bulk response of reactor structures, such as structural and blanket materials, to fusion energy conditions has received comparatively less attention. Defect formation within the bulk microstructure has often been explored independently of the PMI using a combination of neutron and ion irradiation techniques with a focus on the formation of dislocation loops, voids, and precipitates (resulting both from radiation induced segregation and transmutation) [197, 172, 198, 199, 200, 201]. However, the coupling of near-surface phenomena with bulk microstructure evolution and its implications for the thermomechanical response of structural and blanket materials have received considerably less attention, but are critical from both design and engineering viewpoints.

Knowledge of defect distributions with high temporal and spatial resolution is required to link to meso and macroscopic level formulations of property degradation to inform reactor design and/or operation. For example, the accumulation of plasma ion clusters in the subsurface region of the divertor and its interaction with neutron damage and transmutation atoms in the bulk creates nontrivial concentration gradients that can lead to the internal accumulation of complex species and defects. The effect of this accumulation on component performance, e.g. via irradiation hardening, swelling, loss of thermal conductivity, etc., is of critical importance for fusion materials development. Owing to certain intrinsic limitations, experiments can only provide incomplete or indirect information about processes occurring in the subsurface region. In principle, however, these processes are amenable to large-scale modelling and

simulation building on atomistic information from DFT or MD, provided that several difficulties are addressed in algorithm development, model scale-up, and computational efficiency. Some essential features of models designed to predict and quantify material property degradation in the surface-to-whole-device transitional regions are (i) full spatio-temporal resolution, (ii) ability to connect atomistic scale behaviour with mesoscopic response models, (iii) ability to consider multiple chemical species simultaneously, and (iv) a capability to take into account spatial fluctuations. State-of-the-art computational methods to study fusion materials degradation lack many of these features at present.

4.2. Advanced & hybrid simulation techniques

Limitations in direct atomistic methods such as DFT or MD, where time and length scale constraints restrict deposition fluxes to several orders of magnitude higher than real device fluxes [202, 203, 204, 205], are being addressed through the development of hybrid simulation techniques. Accelerated MD methods, such as parallel replica dynamics [206], hyperdynamics [207] or temperature accelerated dynamics [208], help in the time scale albeit fail to reach experimental times because of the high computational resources needed to track events with high rates (i.e. low energy barriers). Parallel replica dynamics is also limited in the way that structural transitions are detected and the parallel replicas, etc. are updated. Newer techniques, such as adaptive kMC, help overcome these barriers by searching for events and developing the list of possible transitions on-the-fly [209, 210, 211]. Other hybrid Monte Carlo (MC) methods can be applied to achieve representative microstructures in the presence of impurities or alloying elements in a material and explore how the microstructure evolves as they segregate to sinks (grain boundaries, interfaces, or dislocations). These methods are based on statistical mechanical descriptions of the system to sample probable configurations identified using the Metropolis algorithm in the canonical ensemble. Semigrand-Canonical algorithms have also been developed where particles are exchanged with a reservoir at a prescribed chemical potential. However, these methods cannot be applied in regions of the phase diagram where different phases have equal chemical potentials (i.e., miscibility gaps), as is the case to study He in metals, since its solubility is negligible. To address this limitation, the Variance-Constrained Semigrand-Canonical algorithm [212] was developed, which introduces an extra constraint in the statistical mechanical derivation of the probability function to extend to alloys inside the miscibility gap. This algorithm has been used to understand He segregation to different grain boundaries in W [213]. Six different bicrystals with different misorientations were studied and in all cases, He was observed to segregate to the grain boundaries and form bubbles as shown in Figure 18. The presence of He significantly modified the mechanical response of the material [214, 215, 216], promoting decohesion in a manner that depends on the atomic details of the interface and the bubble pressure. It also augmented the response of the material under shear stress, in this case increasing the yield strength (see Figure 18c).

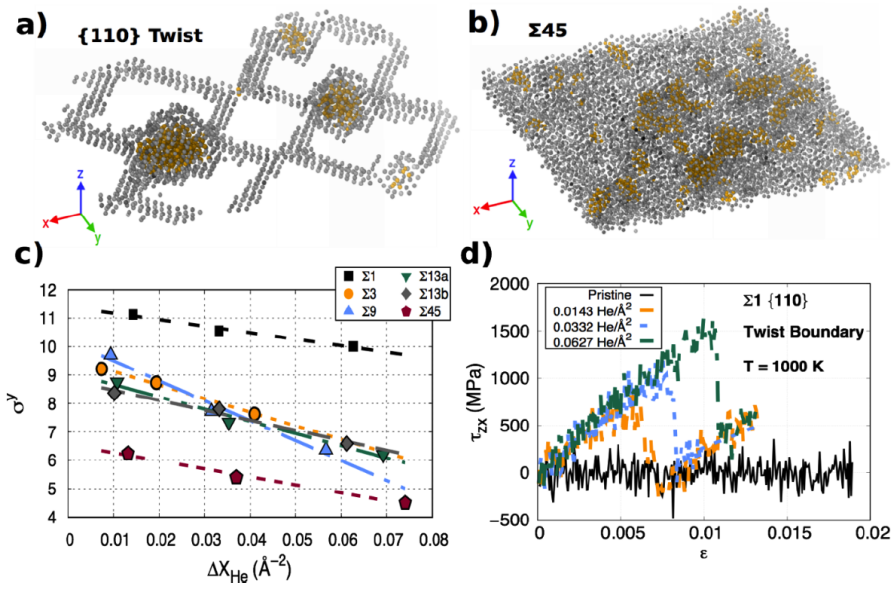

Figure 18: He segregation to a) {110} twist and b) Σ45 interfaces. W and He atoms are shown in gray and orange, respectively. c) Yield stress upon normal loading depending on interface misorientation and He content. d) Stress-strain response of the system containing a {110} twist interface upon shear depending on He content. Images courtesy of E. Martinez, Los Alamos National Laboratory.

4.2.1. Adaptive kMC

kMC methodologies instead coarse-grain the atomic vibrations and rely on different levels of approximation to compute the rates for all possible events occurring in the system. Provided that all transitions and their rates are known (or at least pre-specified), kMC can push the time and length scale envelope w.r.t. direct atomistics, but is still limited in capturing surface morphological evolution [217, 218, 219]. Additionally, considering the atomistic details of microstructural features in materials including grain and phase boundaries is cumbersome. Adaptive kMC (AkMC) [209, 220] methods dynamically compute possible events and in principle can find transitions in the presence of grain boundaries; however, the rough potential energy landscape reduces the ability of this method to reach the required timescale. Object kMC (OkMC) [221] models further coarse-grain the atomic positions and follow the evolution of objects of interest, such as irradiation-induced defects and impurities, but lose the atomistic details of the interfaces through the coarse-grain homogenization of the landscape. This is a serious limitation for capturing property evolution due to irradiation, which often involves processes where small clusters of atoms interact with microstructural features. A method to map homogenized configurations back into full atomistic structures will open the possibility of understanding the effect of irradiation-induced damage on the basic mechanisms of materials under

stress and thus be extremely valuable for the radiation damage community.

4.2.2. Continuum methods

For their part, continuum methods such as mean field rate theory (MFRT) can be implemented on regular or irregular spatial grids to solve spatially-dependent problems [222]. However, they fail to capture essential fine-scale features of the involved processes and, in the current, most-advanced implementations, they can only deal with two distinct chemical species (point defects and He [223], or point defects and H [224]), making them insufficient to capture the complex chemistry expected in fusion environments. The stochastic cluster dynamics method (SCD) is a stochastic variant of the MFRT technique that eliminates the need to solve exceedingly large sets of ordinary differential equations (ODEs) and relies instead on sparse stochastic sampling of the underlying kinetic master equation [225]. Rather than dealing with continuously varying defect concentrations in an infinite volume, SCD evolves an integer-valued defect population in a finite material volume, thus avoiding combinatorial explosion in the number of ODEs. This makes SCD ideal to treat problems where the dimensionality of the cluster size space is high, e.g., when multispecies simulations for example involving energetic particles, He, H, etc., simultaneously are of interest. In practice, SCD sits at the intersection between MFRT and KMC, and can thus take advantage of the mean-field approximation for computational expediency while avoiding combinatorial explosion and allowing for statistical fluctuations. SCD has been applied successfully to fusion irradiation problems involving multispecies clusters [225, 226].

As well, there are other interesting methods that have been employed in materials simulations that could be adopted for fusion materials modelling. For example, the family of so-called quasi-continuum methods is predicated on the combination of highly-accurate atomistic descriptions of the environment around defects with computationally-efficient linear elastic descriptions of the surrounding volume, all in a seamless fashion, without the presence of numerical artifacts [227]. The Quasi-continuum method takes advantage of the local nature of nonlinear stress fields around defects while describing unstressed or smoothly-stressed regions of the crystal using mean-field treatments. This has proven to be an effective computational strategy to concurrently simulate large systems containing an arbitrary number of heterogeneities. However, while these methods hold substantial potential, and have been successfully applied in a number of materials deformation processes [228, 229], stiff challenges still remain unresolved, the most pressing of which being how to accurately avoid spurious reflections of elastic waves in unstructured meshes in dynamic simulations [230].

4.2.3. A multiscale future?

Combining the aforementioned modelling approaches in a multiscale framework to bridge surface phenomena to bulk microstructural effects in materials for DEMO introduces additional challenges related to their increased chemical and microstructural complexity. For example, the limitations of W as a PFM including its recrystallization temperature [231] ($\sim$1300°C), oxidation resistance [232],

radiation tolerance [233], and mechanical performance [234] have motivated the development of advanced W based alloys [234, 235, 236, 237]. A synergistic alloy design strategy that combines nanostructuring with targeted doping of grain boundaries has been pursued to improve the thermal stability and radiation tolerance of W relative to its pure, coarse-grained counterpart [238, 239]. Lattice based MC (LMC) techniques [240], which reveal the lowest free energy state of an alloy from a configurational space incorporating chemical mixing with grain boundary energetics, have played an important role in mapping dopant species and concentrations for the design of solute-stabilized nanostructured W alloys. As shown in Figure 19a, Ti has a thermodynamic preference to segregate to grain boundaries while Cr clusters to form nanoprecipitates. Guided by modelling, nanocrystalline W-Ti-Cr powders ($\geq$ 80 at.% W) have been produced via powder metallurgy synthesis (nanostructure depicted in the bright-field image in Figure 19b) and consolidated to form bulk nanostructured W alloys as shown in Figure 19c. modelling the behaviour of these materials under coupled extremes, specifically quantifying defect production in cascades, gas behaviour, and their implications for microstructural evolution, requires W-alloy potentials to complement the more or less reliable W-He and W-He-H interatomic potentials [205, 206, 207].

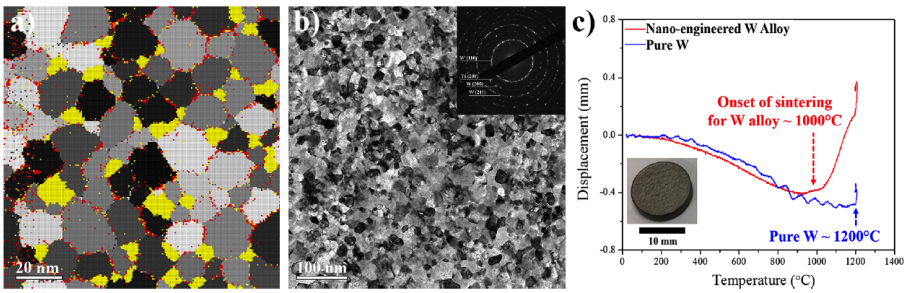

Figure 19: (a) LMC model for a nanostructured W-Ti-Cr alloy with W-rich grains shown in grey-scale, Ti atoms in red, and Cr atoms yellow. (b) Bright-field TEM micrograph of a binary W-Ti alloy revealing a nanocrystalline grain structure. (c) Sintering curves for the consolidation of a nanoengineered W alloy relative to pure W demonstrating a considerable reduction in the sintering temperature. Image courtesy of J.R. Trelewicz, Stony Brook University.

Mesoscale phase-field approaches could also be a potential tool in predicting microstructure evolution and property degradation in irradiated materials, especially in materials where initial microstructures (i.e., grain morphology, different phases and interface) and radiation-induced microstructure evolution (i.e., the system never reaches steady state, high volume fraction of evolving phases, high doses) importantly impacts radiation defect accumulation and material properties [241]. However, there are still there are still grand challenges to make quantitative simulations (how to correctly capture the length scale of microstructures; the thermodynamic and kinetic properties of defects; how to use high performance computers to perform the large-scale modelling; how to

integrate machine learning to efficiently solve the evolution equations).

The operation of a fusion power plant will inevitably present new challenges that fall beyond the capabilities of our existing and envisioned modelling frameworks. For example, the behaviour of W based PFCs under accident scenarios introduces the need for predictive models describing oxidation. Indeed, self-passivating, smart W alloys are under development with an aim to minimize radioactive hazards by suppressing W oxidation and sublimation at high temperatures [242, 243, 244]. In the case of a loss-of-coolant-accident (LOCA) where the temperature of the W first wall cladding may reach 1000°C and above due to nuclear decay heat [245], neutron-activated W and its isotopes will form volatile oxides upon air ingress, which can be mobilized to the environment at the rate of 10-150 kg per hour [246]. Under such conditions, alloying elements will form their own dense oxide layer protecting W from oxidation and subsequent sublimation of W oxide. Present smart W alloy systems contain Cr as a passivating element and Y as a so-called active element [247]. Bulk alloys have been realized through powder metallurgical routes with a 10^5-fold reduction in the oxidation rate relative to that of pure W with complementary studies of accident conditions and plasma performance at the timescale corresponding to a lifetime of a first wall PFC in DEMO [248, 249]. Direct measurements of W sublimation from a smart alloy exhibited more than a 40-fold reduction relative to pure W as shown in Figure 20 while preserving its geometrical shape through testing.

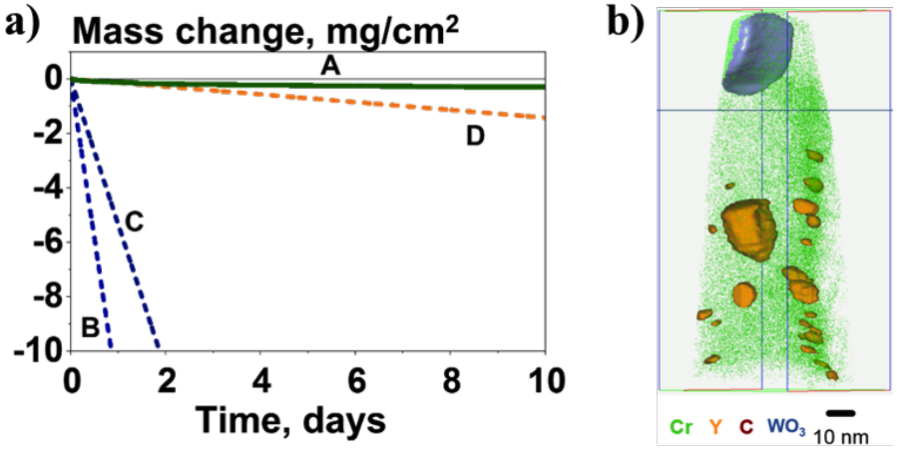

Figure 20: a) Mass reduction due to sublimation as a function of exposure time for W-Cr-Y smart alloy (curve A), fully oxidized W thin film (curve B), oxidized bulk W sample (curve C) and for oxidized pure Cr film (curve D) in humid air at 1000°C. b) APT analysis of post-oxidation W-Cr-Y alloy, showing clusters of Y and W oxide. Image courtesy of A. Litnovsky, Forschungszentrum Jlich GmbH.

modelling needs in the aforementioned alloys are centered on the impact of alloying elements for material behaviour under regular plasma operation and accident conditions. Specific phenomena critical to understanding the response of

advanced alloys for a fusion reactor include: (i) quantifying solute distribution among different microstructural features and its impact on thermomechanical properties, (ii) diffusive transport of bulk alloying elements toward the surface and potential biasing of fundamental processes at the PMI (e.g., selective sputtering, He and H retention, etc.), (iii) bulk damage evolution as a result of neutron irradiation and its interaction with surface damage, and (iv) the implication of these complex, intertwined processes on the evolution of thermomechanical properties and oxidation resistance. Using ab initio calculations, progress has been made in understanding the behaviour of Y at grain boundaries in W-Cr-Y alloys: segregation of Y-containing nanoclusters to the grain boundaries of the W-Cr solid solution was predicted and subsequently observed experimentally using atom probe tomography (APT) as shown in Figure 20b. However, as noted above with the W-Ti-Cr alloys, the limited availability of interatomic potentials for alloy systems of interest severely hinders steps toward multiscale models for advanced fusion materials.

4.3. Validation from experiment

As multiscale modelling techniques continue to be advanced to address critical knowledge gaps linking microstructure to thermomechanical properties, new opportunities for accelerating model validation are being realized through advanced characterization techniques. X-ray techniques available at advanced synchrotron light sources offer ultra-high brightness relative to standard laboratory sources, and in turn provide rapid measurements facilitating both high-throughput and in situ experiments [250, 251, 252]. When leveraged in a multimodal fashion with conventional characterization methods (e.g., TEM [253, 254, 255], PAS [256, 257], APT [258, 259], and SANS [260]), these techniques provide a fundamental understanding of key parameters that lead to microstructural changes and thermomechanical performance degradation. Such approaches also facilitate direct validation of mechanistic models for material performance through unprecedented access to realistic morphology and microstructural information [261, 262, 263]. For example, synchrotron x-ray diffraction (XRD) and small angle x-ray scattering (SAXS) experiments were employed in the quantification of MX and M23C6 precipitate fractions in castable nanostructured alloys (CNAs), which represent a special class of reduced activation ferritic-martensitic (RAFM) steels. Combined with atomic information in both the host matrix and these minor phases, computational thermodynamics predictions originally used in designing the CNAs [264] were validated as summarized here in Figure 21.

Laser based material property measurements also have the potential to further reduce the temporal gap in the generation of experimental data for verification of computational models. Most techniques begin with the same initiating mechanism: the transmission of heat into a material of interest. This can be a simple Gaussian pulse for techniques like laser flash [265] or time-domain thermal reflectance (TDTR) [266], both of which measure thermal diffusivity, to creating a spatially periodic pattern, such as in transient grating spectroscopy (TGS) [267], to the rapid imposition of a large amount of energy resulting in a shock wave [268]. Then, the propagation of this energy in the form of heat

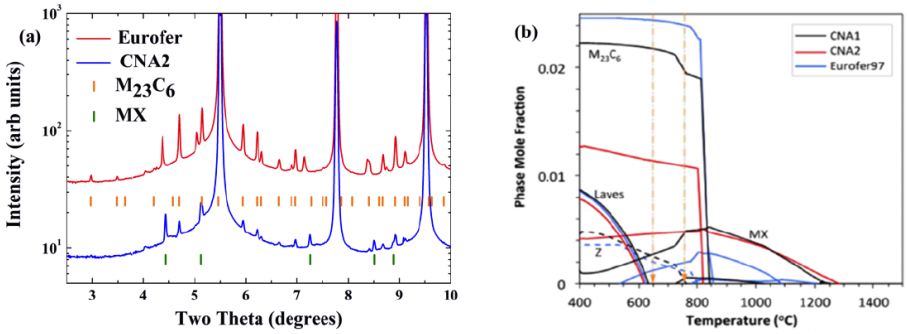

Figure 21: (a) XRD patterns for RAFM alloys Eurofer97 and CNA2. Phases overlaid for reference. (b) Phase fractions predicted from computational thermodynamics for Eurofer97 and CNA alloys shown in (a) (reproduced from [252]). Images courtesy of D.J. Sprouster, Stony Brook University.

diffusion, acoustic wave generation, or wave scattering can reveal desired information about a materials properties and how they change under imposed stimuli. In some cases, the properties measured (thermal diffusivity, Rayleigh wave velocity, stiffness, acoustic damping) may be the material properties of ultimate interest. For example, studying the degradation in thermal diffusivity of W under combined plasma impingement and light ion irradiation is poised to reveal information on the underlying mechanisms. Monitoring thermal diffusivity degradation will be particularly important in developing radiation-robust materials for divertors. In other cases, an indirect measure of one or more material properties correlated to the one(s) of ultimate interest can yield rapid insights into the kinetics of the changes to materials, allowing for more targeted identification of exposure conditions for more time-consuming, destructive analyses. Examples include monitoring Rayleigh wave speed to detect the onset of radiation void swelling [269], revealing corrosion kinetics via transmission-mode TGS compressibility measurements [270], and identifying the onset of W nanofuzz [196] via a reduction in effective thermal diffusivity. Thus, the growing need to validate multiscale models by building a mechanistic understanding of material property evolution during the application of external stimuli will continue to drive the implementation of ultra-rapid direct and indirect advanced characterization methods in fusion materials R&D.

5. Gas behaviour in solids

This final section discusses modelling of a unique material challenge for fusion; that of neutron-induced gas production and evolution. Section 5.1 reviews the current understanding and outstanding questions for He and H-induced bubble formation. The remainder of the section is devoted to tritium: the behavioural understanding obtained from the real world experience in fission

(5.2), and the latest simulation approaches to understand fuel retention in fusion plasma-facing materials (Section 5.3).

The extremely harsh fusion environment, characterized by a combination of high temperature, high thermal flux, and intensive flux of gaseous species (i.e., D, T, He) and neutrons, imposes significant challenges to plasma facing and structural materials in fusion reactors. Fundamental understanding of gas behaviour in fusion materials is needed to accurately predict the long-term performance of materials when in service. Of particular importance is the impact of the synergism of radiation damage, He and H isotopes on gas behaviour in fusion materials, which encompass both structural materials subject to high fluxes of 14 MeV neutrons, the breeding blanket that will generate significant quantities of tritium, and the plasma facing components which will experience injection of high fluxes of H isotopes and tritium. As well, the behaviour of H isotopes, and to a lesser extent He, is critically important in fission cladding and tritium production for national security needs. The behaviour of H in Zr-alloys will not be discussed here, but the interested reader is referred to an excellent recent review article by Motta and co-workers [271].

5.1. Bubble formation

The role of H in the nucleation and growth of He bubbles into cavities remains largely unanswered and poorly understood since the existing data are both sparse and conflicting. Yet the role of H and He in bubble nucleation and growth is critical to assessing performance of candidate ferritic alloys in a fusion blanket environment. Key questions to answer are the following. First, how and to what extent does the generation of H simultaneously with He affect the nucleation and growth of cavities? Second, what is the mechanism by which H affects the nucleation and growth of cavities? H has been variously purported to stabilize small He bubbles, enhance cavity growth beyond the nucleation stage, alter the surface energy of the bubbles/cavities, and change the critical bubble size at which a bubble transitions to bias driven cavity growth. Finally, and of equal importance, is whether there is an interaction between H and other defect/solute clusters in the alloy.

The starting dislocation microstructure and precipitate distribution and their evolution under irradiation are sites for interaction with H that could affect its efficacy in altering cavity evolution. The experiments conducted to date have established that the existing body of data is too sparse and lacking the systematic rigor required to answer these questions, and in fact there is conflicting data in the literature as to whether H enhances or reduces swelling in ferritic martensitic steels [272, 273]. While there seems to be substantial evidence that H plays a role, it is neither qualitatively nor quantitatively established. There are a number of mechanisms by which H could interact with bubbles and small defect clusters containing He and vacancies, including the possibility that H is stored within bubbles or cavities in the form of H_2 gas or that H is trapped at the bubble interfaces as a result of the stress field associated with the interface. H may stabilize the small defect clusters but with a

relatively low binding energy, such that the impact of H on cavity nucleation would be greater at low temperatures relative to high temperatures.

Notably, there is data to support the idea that H is stored within bubbles in molecular form, as observed by Garner and co-workers [274] in austenitic steels irradiated in fission reactors, in which the H is at much higher concentrations in the bubble or voids than He. As well, there are numerous indications that atomic H that is trapped at the interface of high pressure He bubbles, as was identified in work on He implanted bcc Fe by Meyers and co-workers [275] and in the nickel base alloy X-750 irradiated in CANDU reactors with very large He production by Judge and co-workers [276]. The experimental assessments indicating the segregation and trapping of atomic H at high pressure He bubbles is consistent with atomic-scale modelling in the form of MD [277] and DFT calculations in both bcc Fe [278] and W [279], which finds that the segregation and trapping of atomic H to the interface of noble gas bubbles which is relatively insensitive to gas densities of over-pressurized bubbles. Thus, a strong interaction between H and He bubbles in bcc Fe and W leading to segregation and trapping of H appears to be a robust conclusion, although future work remains to fully quantify the trapping energies as a function of He density (pressure) of the bubbles and to address the extent to which the trapping interactions involve atomic H at the bubble matrix interface versus molecular H within the bubble or void, which also is likely gas pressure dependent.

Various experimental techniques available to study these synergistic interactions between H and He in steels and W. There are advantages and disadvantages involved with using multiple ion beams to simultaneously introduce displacement damage while implanting gas species. The use of multiple ion beams does provide for the potential to carefully and systematically perform experimental investigations with proper care taken for the beam dosimetry, sample temperature and avoiding carbon or other beam contamination concerns [280]. In addition to the use of transmission electron microscopy and thermal desorption spectroscopy, laser based ablation techniques have been developed to destructively quantify the depth dependence of H and He in W [281], and there is also the non-destructive use of neutron depth profiling to assess the spatial dependence of He-3. There are also various techniques of gas driven permeation to assess H isotope permeation in ferritic martensitic steels as well as W. Again, however, the experimental understanding of He-H interaction synergies in fusion materials is incomplete, and much more work is required in the future.

There is a strong trapping interaction of grain boundaries for He in bcc Fe and W, respectively, and grain-boundary He bubbles can influence the tensile behaviour of Fe [282] and W [283]; both small and highly pressurized He-vacancy clusters reduce the grain boundary strength and fracture strain [284, 213]. In particular, upon tension, the presence of He significantly decreases the yield stress, which depends considerably on the bubble pressure. Increasing pressure reduces cohesion, as expected. More complex stress states result in more convoluted behaviour, with He hindering grain boundary sliding upon simple shear [213]. The topic of grain boundary He bubble formation is an area ripe for additional research, both in terms of predictably assessing the bubble density

and pressure at grain boundaries as a function of irradiation conditions, but also to evaluate the impact on both low and high temperature (e.g., creep) deformation and fracture behaviour. There is enormous potential in the future to utilize machine learning aspects within the computational modelling framework to impact our understanding of nuclear materials behaviour, incorporating an example involving the use of a neural network regression to predict aluminum segregation to grain boundaries in magnesium [285].

5.2. Tritium production

An important topic in gas behaviour research concerns the experience with national tritium production in support of US national security, called the Tritium Modernization program, which concerns the use of a commercial reactor to produce tritium via the irradiation of components known as Tritium-producing Burnable Absorber Rods (TPBAR). Development of fundamental scientific understanding of TPBAR material's irradiation performance reduced the technical and programmatic risk. Key findings from the fundamental studies clearly indicate the importance of the H partial pressure on the tritium pressure through the SS-316 cladding, and that the hydride phases observed to form in the Zircaloy-4 getter that absorbs the tritium may include γ-ZrH, which has been observed to form in rapidly loaded getters in ex-reactor settings (work is ongoing to determine if the γ-phase also forms at reactor temperatures in getters loaded slowly over $\sim$18-month reactor cycles) and is a transition phase between α-Zr and δ-$ZrH_{1.66}$ [286, 287]. Additionally, results from in-reactor permeation experiments clearly identify a 3-5 times enhancement of tritium permeation through 316 stainless steel in-reactor as compared to ex-reactor testing, which occurs with the expected square root pressure dependence, although the precise mechanistic cause for the enhanced permeation is not yet well established, but may relate to complex interactions between H and irradiation induced interstitial defects [288, 289]. Thus, significant work remains to understand H interactions with radiation induced defects across a range of nuclear materials, although there are numerous new experimental techniques and improving computational modelling capability to continue addressing the issues.

For example, The $LiAlO_2$ pellets used for tritium production in the Tritium Modernization Program exhibit remarkable dimensional and structural stability during irradiation, even to relatively high burnup ($\sim$12% total Li) [290, 291]. Characterization of irradiated pellets coupled with computational modelling reveal that the radiation damage is isolated to the interior of the grains, resulting from the tendency of Li to migrate to the grain boundaries in the radiation-damaged lattice while Al and O are relatively immobile. Consequently, the pellets have dense $LiAlO_2$ regions adjacent to the grain boundaries with Li-poor $LiAl_5O_8$ precipitates and porosity in the grain interiors, forming a stable microstructure capable of accommodating significant radiation damage without deleterious dimensional changes.

5.3. Simulations of hydrogen retention in damaged W

Fuel retention in plasma facing W components is a critical phenomenon affecting the mechanical integrity and radiological safety of fusion reactors. It is known that H can become trapped in small defect clusters, internal surfaces, dislocations, and/or impurities, and so it is common practice to seed W subsurfaces with irradiation defects in an attempt to precondition the system to absorb H. The amount of H can later be tallied by performing careful thermal desorption tests where released temperature peaks are mapped to specific binding energies of H to defect clusters and/or microstructural features of the material. While this provides useful information about the potential trapping processes, modelling can play an important role in elucidating the detailed microscopic mechanisms that lead to H retention in damaged W. During H exposure tests, one can study H absorption in materials (i) in the as-received condition, (ii) pre-irradiated with heavy ions, (iii) pre-implanted with He ions, or (iv) under concurrent irradiation/implantation and H exposure conditions. These scenarios can be captured using kinetic models of H penetration and trapping with spatial resolution [292]. A crucial requirement of these models is that they be parameterized using detailed DFT calculations of H-vacancy cluster energetics [293, 294]. This enables models to directly identify the dominant defect clusters responsible for H trapping in each temperature range.

In a recent study [292], spatially-resolved SCD simulations have been instrumental in interpreting H thermal desorption spectra of pre-damaged W specimens. As Figure 22 shows, the emission spectra are characterized by distinct regions: (i) a low temperature regime where dislocations and grain boundaries are the main contributors to the release peaks; (ii) an intermediate one governed by H release from small overpressurized clusters with multiple overlapping peaks, and (iii) a high temperature one defined by clean isolated emission peaks from large underpressurized bubbles. These three temperature intervals are seen to largely correlate with the depth at which the clusters are found. A key finding of these simulations is the pivotal role played by the super abundant vacancy mechanism, which is fundamentally analogous to the 'trap-mutation' mechanism in He-implanted materials [295, 296]. Such mechanism allows H-vacancy clusters to grow 'on demand' by emitting a self-interstitial atom and increasing their capacity to further absorb H atoms.

6. Summary and outlook

A fusion materials workshop arranged under the auspices of the IEA was held in June 2019. More than 25 leading researchers from the US, Europe and Japan discussed the current state of the art and ongoing challenges in the multiscale modelling of materials for nuclear fusion applications, as well as highlighting the latest advances in experimental characterisation techniques, which are helping to provide improved data to modelling. This paper has reviewed the key topical areas discussed, including modelling of irradiation-induced defect production at the atomic scale, larger length and timescale modelling of defect evolution

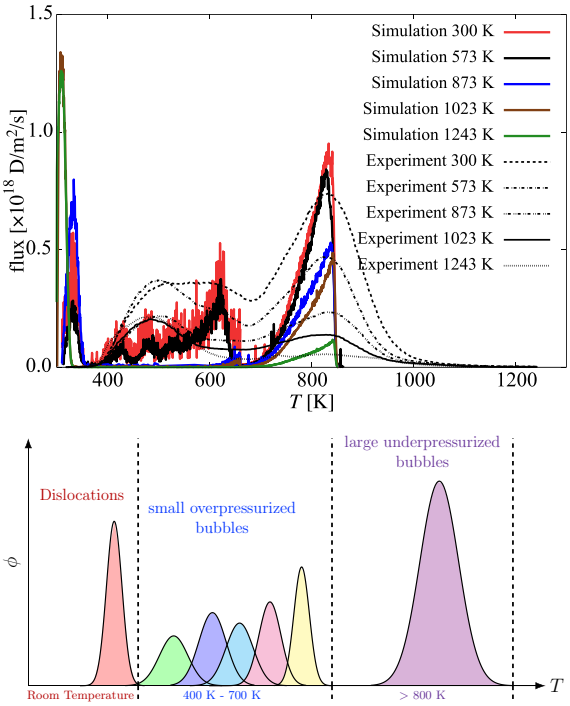

Figure 22: Results of spatially-resolved SCD simulations of H exposure and trapping of 3.4-MeV Cu ion implanted W. The top image compares the calculated and experimental thermal desorption spectra, while the bottom one is a cartoon with the interpretation of the different cluster species participating in the release peaks. From [292].

and interactions, the importance of gas behaviour in irradiated materials, and how to predict and interpret material behaviour based on multiscale modelling approaches.

Atomistic simulations, including MD and DFT, have struggled to reach the scales (time, length, statistics) needed to provide meaningful engineering inputs. However, the situation is improving; computing resourcing and power has now reached the point where it is possible to produce statistically significant databases of damage cascade simulations with MD [107, 125], particularly for pure fusion-material systems such as W and Fe, enabling, for example, analysis of the cascade overlap behaviour that will characterize evolution at higher doses under fusion conditions in materials with pre-existing defects [297, 298] or to study sub-cascade formation [22]. Recent simulations [26] show, for example, that interconnected sub-cascades in W allow large defect structures to form, indicating that the assumption, perhaps valid for Fe, that high-energy damage events can be modeled using random distributions of the defects produced in constituent sub-cascades might not be valid in W.

It is also possible, using an approach involving MD but avoiding direct cas-

cade simulations, to model microstructures corresponding to very high exposure to irradiation approaching the dose of 20 dpa [180]. Experimental observations of radiation damage in heavily irradiated W [299] show good agreement with predictions derived from simulations based on [180] and also exhibit a surprisingly significant effect of self-stress on the microstructure developing as a result of accumulation of defects during irradiation.

Large-scale atomistic simulations can also start to treat surface phenomena and bulk evolution together, which is needed to understand engineering performance of materials under reactor conditions. Experiments have difficulty probing these characteristics but acceleration methods and hybrid techniques are beginning to quantify some of the material degradation phenomena and shed light on the behaviour hidden from experiments.

In parallel, AI methods are being employed to offer a bridge between accurate but slow quantum-based *ab initio* DFT methods and the less-accurate but fast classical MD. While acknowledging that these approaches cannot replace full understanding of the physics, statistical machine-learning (ML) methods trained on carefully obtained physical data can be of great help when the traditional methods are limited or/and their direct application is hindered by such factors as high computational cost. The synergy of ML approaches with traditional methods opens many avenues in material science. Reinforcing materials modelling with ML methods gives an access to the crucial physical properties, such as accurate total energy and MD trajectories [63, 82, 300, 49, 51, 52], accurate defects characterization based on distortion score [54], free energy sampling with *ab initio* accuracy [66, 65], or even investigation of continuum domains of materials science [301].

At the same time, dynamic simulations are now becoming possible with ab-initio DFT methods (e.g. to calculate threshold displacement energies [4]), highlighting discrepancies with results based on semi-classical models, although careful acceleration methods [8], where the greatest precision (largest number of valence electrons) is only used in the most active regions of the cascade, are part of ongoing development to reduce the high computational cost required to treat larger number of atoms in quantum MD.

The availability of real statistics from MD simulations or otherwise is also allowing for new interpretations of experiments by helping to understand the damage populations in irradiated materials; for example quantifying the defects missed in experimental counting (due to resolution limits, defect shadowing, invisibility, etc.). This, combined with improved and automatic experimental counting approaches is allowing more direct quantitative comparisons between simulation methods, such as kMC, and TEM observations [127] and the improved understanding of how small defect clusters can dominate microstructure in irradiated materials has led to development of new theories to explain how swelling occurs in these circumstances. This subject might not have received attention if the traditional view of large-defect dominated microstruture had persisted, illustrating the power of combining modelling with experimental analysis; this will likely prompt future combined experimental-simulation research collaborations.

kMC, along with rate theory based approaches, is also being used to explore evolution beyond the the immediate cascade collapse timescales (several picoseconds) that MD cannot currently reach with regularity. These techniques are able to reach the time and length scales of irradiation experiments and can begin to provide understanding of the defect evolution behaviour that will occur in the harsh neutron irradiation fields of fusion reactors.

However, there are still complexities of real materials that modelling has yet to satisfactorily address, including the role of impurities in trapping or otherwise altering the behaviour of dislocations and other defects and the corresponding influence on behaviour; such as carbon's effect on grain boundary strength [302] or as a contaminate influencing the interpretation of ion-irradiation experiments [303]. Direct comparison between kMC simulations of non-pure systems (e.g. alloys) and advanced experimental techniques such as APT that allow direct observation of clustering is an ongoing challenge, despite examples of qualitative agreement (e.g. [304] for clustering in RPV steels). Recent improvements in the cluster analysis approaches for APT data are helping to define where modelling effort should be directed in the future. Also, it is not yet clear how to seamlessly relate kMC simulations, typically neglecting effects of elastic deformation and the associated stresses, to dislocation dynamics and to the dislocation-based treatment of plasticity of irradiated materials.

Meanwhile, new multiscale modelling frameworks combining several of the advanced techniques, such as MD with Monte-Carlo methods (e.g. [213]), or DFT with mean-field theory (e.g. stochastic cluster dynamics or SCD [226]), and combined with modern computational approaches such as machine learning, are allowing simulations to predict changes in material behaviour and can bridge surface phenomena to bulk effects. For example they are helping to model the limitations of W as a plasma-facing material and thus to design advanced W solutions such as solute-stabilized W-alloys [240]. However, these integrated approaches are limited by the loss of atomistic details through the coarse-graining and homogenization required to reach the reactor-relevant time and length scales; a method to map back to full atomistic structures remains an outstanding challenge, which, if solved, would allow for the possibility of matching irradiation-induced damage to basic mechanisms driving material performance.

An ongoing area of innovation concerns modelling of alloys, both in the low impurity concentration limit, which is more representative of real engineering materials, but also at higher "additive" concentrations characteristic of alloys engineered to solve specific issues in the nuclear environment (e.g. so-called W smart alloys designed to prevent WO_3 formation [248]).

Various advanced experimental characterisation techniques are helping to accelerate model validation by reducing the spatial and temporal gap been simulations/models and experiments, including X-ray diffraction imaging [305] and laser-based measurements [267, 306].

The behaviour of gas, helium and hydrogen, in structural fusion materials, either created directly in structural materials due to reactions with high energy neutrons or originating from exhaust gases of the fusion plasma impinging on

reactor walls, is a key and unique (to fusion) issue where understanding is still developing. Recent modelling effort has looked at the influence of H on the formation of He bubbles, where experimental data has so far proved inconclusive (although it generally suggests that H plays a role) [307]. Atomistic simulations (MD and ab-initio) appear to be consistent with the idea that H is trapped within He bubbles. Helium is strongly trapped at grain boundaries and can dramatically change material performance. However, both the mechanism of bubble formation at GBs, and the impact they have on, for example, deformation and fracture behaviour is still a new research area, with many opportunities for modelling to contribute in the future.

There is an open question as to whether H enhances [308] or reduces [272] swelling in steels. Similarly, helium can both increase and decrease swelling depending on the density of pre-existing or irradiation-induced cavities [309].

Even in mature industries, such as tritium production in fission reactors for strategic stockpiles, there is still ongoing questions that require attention, such as how hydrogen isotopes propagate through materials exposed to irradiation and therefore containing defects. In fusion, tritium (i.e. fuel) propagation and retention in materials is even more critical because it can severely effect both material (degredation) and reactor (efficiency) performance and will impact on radiological safety. This important issue is receiving significant experimental attention, for example via thermal desorption spectroscopy (TDS) (e.g. [310, 311], and innovative modelling approaches are being developed such as spatially-resolved SCD [292].

As the foregoing illustrates, the field of modelling applied to the problem of materials for nuclear fusion applications is active and multi-faceted, and involves experts from around the world. Amazing progress has been made, particularly in using modelling to interpret experiments, but there is still a long way to go to make modelling the truly predictive tool that is required for the next phase of fusion development; that of engineering realization of commercial and near-commercial fusion power plants.

Acknowledgements

MRG, SLD, DM acknowledge funding by the RCUK Energy Programme [grant number EP/T012250/1]. Part of this work has been carried out within the framework of the EUROFusion Consortium and has received funding from the Euratom research and training programme 2019-2020 under grant Agreement No. 633053. The views and opinions expressed herein do not necessarily reflect those of the European Commission. JRT acknowledges funding from the US Department of Energy (DOE) through grant DE-SC0017899. ZB, LY and BDW acknowledge funding through the US DOE Fusion Energy Sciences grant DE-SC0006661, as well as partial support from the US DOE Office of Science, Office of Fusion Energy Sciences and Office of Advanced Scientific Computing Research through the Scientific Discovery through Advanced Computing (SciDAC) project on Plasma-Surface Interactions. JMa acknowledges support

from the US-DOEs Office of Fusion Energy Sciences (US-DOE), project DE-SC0019157. Pacific Northwest National Laboratory is operated by Battelle Memorial Institute for the US Department of Energy (DOE) under contract DE-AC05-76RL01830. YO and YZ were supported as part of the Energy Dissipation to Defect Evolution (EDDE), an Energy Frontier Research Center funded by the U.S. Department of Energy, Office of Science, Basic Energy Sciences under contract number DE-AC05-00OR22725. TS and TT are supported by JSPS KAKENHI Grant Number 19K05338.

References

[1] L. Malerba, A. Caro, J. Wallenius, Multiscale modelling of radiation damage and phase transformations: The challenge of FeCr alloys, Journal of Nuclear Materials 382 (2) (2008) 112 – 125, microstructural Processes in Irradiated Materials. doi:10.1016/j.jnucmat.2008.08.014.

[2] K. Nordlund, S. J. Zinkle, A. E. Sand, F. Granberg, R. S. Averback, R. E. Stoller, T. Suzudo, L. Malerba, F. Banhart, W. J. Weber, F. Willaime, S. L. Dudarev, D. Simeone, Primary radiation damage: A review of current understanding and models, Journal of Nuclear Materials 512 (2018) 450 – 479. doi:10.1016/j.jnucmat.2018.10.027.

[3] K. Trachenko, E. Zarkadoula, I. Todorov, M. Dove, D. Dunstan, K. Nordlund, Modeling high-energy radiation damage in nuclear and fusion applications, Nuclear Instruments and Methods in Physics Research Section B: Beam Interactions with Materials and Atoms 277 (2012) 6 – 13, basic Research on Ionic-Covalent Materials for Nuclear Applications. doi:10.1016/j.nimb.2011.12.058.

[4] P. Olsson, C. S. Becquart, C. Domain, Ab initio threshold displacement energies in iron, Materials Research Letters 4 (4) (2016) 219–225. doi:10.1080/21663831.2016.1181680.

[5] E. Holmström, A. Kuronen, K. Nordlund, Threshold defect production in silicon determined by density functional theory molecular dynamics simulations, Phys. Rev. B 78 (2008) 045202. doi:10.1103/PhysRevB.78.045202.

[6] H. Y. Xiao, F. Gao, X. T. Zu, W. J. Weber, Threshold displacement energy in GaN: Ab initio molecular dynamics study, Journal of Applied Physics 105 (12) (2009) 123527. doi:10.1063/1.3153277.

[7] H. Y. Xiao, Y. Zhang, W. J. Weber, Ab initio molecular dynamics simulations of low-energy recoil events in ThO_2, CeO_2, and ZrO_2, Phys. Rev. B 86 (2012) 054109. doi:10.1103/PhysRevB.86.054109.

[8] D. Karlsson, A. Rasmussen, Optimization of vasp simulations relating to radiation damage in materials, 2017.

URL https://pdfs.semanticscholar.org/74ce/c04a386beeb75377949365d5e664ab0a6c84.pdf

[9] M. Samaras, P. M. Derlet, H. V. Swygenhoven, M. Victoria, Computer Simulation of Displacement Cascades in Nanocrystalline Ni, Phys. Rev. Lett. 88 (2002) 125505. doi:10.1103/PhysRevLett.88.125505.

[10] O. El-Atwani, J. E. Nathaniel, A. C. Leff, K. Hattar, M. L. Taheri, Direct observation of sink-dependent defect evolution in nanocrystalline iron under irradiation, Scientific Reports 7 (2017) 1836. doi:10.1038/s41598-017-01744-x.

[11] F. Granberg, F. Djurabekova, E. Levo, K. Nordlund, Damage buildup and edge dislocation mobility in equiatomic multicomponent alloys, Nuclear Instruments and Methods in Physics Research B 393 (2017) 114–117.

[12] S. L. Dudarev, Density functional theory models for radiation damage, Annual Review of Materials Research 43 (2013) 35–61. doi:10.1146/annurev-matsci-071312-121626.

[13] C.-C. Fu, J. Dalla Torre, F. Willaime, J.-L. Bocquet, A. Barbu, Multiscale modelling of defect kinetics in irradiated iron, Nature Materials 4 (2005) 68–74.

[14] C. J. Ortiz, M. J. Caturla, Cascade damage evolution: rate theory versus kinetic Monte Carlo simulations, Journal of Computer-Aided Mater Design 14 (2007) 171–181.

[15] P.-W. Ma, S. L. Dudarev, Symmetry-broken self-interstitial defects in chromium, molybdenum, and tungsten, Physical Review Materials 3 (2019) 043606.

[16] P.-W. Ma, S. L. Dudarev, Universality of point defect structure in body-centered cubic metals, Physical Review Materials 3 (2019) 013605. doi:10.1103/PhysRevMaterials.3.013605.

[17] P.-W. Ma, S. L. Dudarev, Nonuniversal structure of point defects in face-centered cubic metals, Physical Review Materials 5 (2021) 013601. doi:10.1103/PhysRevMaterials.5.013601.

[18] Y. Kraftmakher, Equilibrium vacancies and thermophysical properties of metals, Physics Reports 299 (1998) 79–188.

[19] W. G. Wolfer, The dislocation bias, Journal of Computer-Aided Materials Design 14 (2007) 403 – 417. doi:10.1007/s10820-007-9051-3.

[20] W. Hertz, W. Waidelich, H. Peisl, Lattice contraction due to quenching in vacancies in platinum and gold, Physics Letters A 43 (1973) 289–290. doi:10.1016/0375-9601(73)90310-1.

[21] E. Antoshchenkova, L. Luneville, D. Simeone, R. E. Stoller, M. Hayoun, Fragmentation of displacement cascades into subcascades: A molecular dynamics study, Journal of Nuclear Materials 458 (0) (2015) 168–175.

[22] A. De Backer, C. Domain, C. S. Becquart, L. Luneville, D. Simeone, A. E. Sand, K. Nordlund, A model of defect cluster creation in fragmented cascades in metals based on morphological analysis, Journal of Physics: Condensed Matter 30 (40) (2018) 405701. doi:10.1088/1361-648x/aadb4e.

[23] W. Setyawan, A. P. Selby, N. Juslin, R. E. Stoller, B. D. Wirth, R. J. Kurtz, Cascade morphology transition in bcc metals, Journal of Physics: Condensed Matter 27 (22) (2015) 225402.

[24] A. E. Sand, K. Nordlund, S. L. Dudarev, Radiation damage production in massive cascades initiated by fusion neutrons in tungsten, Journal of Nuclear Materials 455 (1-3) (2014) 207–211.

[25] A. F. Calder, D. J. Bacon, A. V. Barashev, Y. N. Osetsky, On the origin of large interstitial clusters in displacement cascades, Philosophical Magazine 90 (7-8) (2010) 863–884.

[26] W. Setyawan, G. Nandipati, K. J. Roche, H. L. Heinisch, B. D. Wirth, R. J. Kurtz, Displacement cascades and defects annealing in tungsten, part I: Defect database from molecular dynamics simulations, Journal of Nuclear Materials 462 (2015) 329 – 337. doi:10.1016/j.jnucmat.2014.12.056.

[27] A. E. Sand, S. L. Dudarev, K. Nordlund, High-energy collision cascades in tungsten: Dislocation loops structure and clustering scaling laws, EPL (Europhysics Letters) 103 (4) (2013) 46003. doi:10.1209/0295-5075/103/46003.

[28] P.-W. Ma, D. R. Mason, S. L. Dudarev, Multiscale analysis of dislocation loops and voids in tungsten, Physical Review Materials 4 (2020) 103609. doi:10.1103/PhysRevMaterials.4.103609.

[29] C. Theodosiu, Elastic Models of Crystal Defects, Springer Verlag, Berlin, 1982.

[30] G. Leibfried, N. Breuer, Point Defects in Metals, Springer, Berlin, 1978.

[31] E. Clouet, C. Varvenne, T. Jourdan, Elastic modeling of point-defects and their interaction, Computational Materials Science 147 (2018) 49–63. doi:10.1016/j.commatsci.2018.01.053.

[32] S. L. Dudarev, P.-W. Ma, Elastic fields, dipole tensors, and interaction between self-interstitial atom defects in bcc transition metals, Phys. Rev. Mat. 2 (2018) 033602.

[33] D. R. Mason, D. Nguyen-Manh, M.-C. Marinica, R. Alexander, A. E. Sand, S. L. Dudarev, Relaxation volumes of microscopic and mesoscopic irradiation-induced defects in tungsten, J. Appl. Phys 126.

[34] S. L. Dudarev, Coherent motion of interstitial defects in a crystalline material, Philosophical Magazine 83 (2003) 35773597. doi:10.1080/14786430310001599388.

[35] M. Boleininger, T. D. Swinburne, S. L. Dudarev, Atomistic-to-continuum description of edge dislocation core: Unification of the Peierls-Nabarro model with linear elasticity, Physical Review Materials 2 (2018) 083803. doi:10.1103/PhysRevMaterials.2.083803.

[36] M. Boleininger, S. L. Dudarev, Continuum model for the core of a straight mixed dislocation, Physical Review Materials 3 (2019) 093801. doi:10.1103/PhysRevMaterials.2.083803.

[37] M. S. Daw, M. I. Baskes, Semiempirical, quantum mechanical calculation of hydrogen embrittlement in metals, Phys. Rev. Lett. 50 (1983) 1285. doi:10.1103/PhysRevLett.50.1285.

[38] M. S. Daw, M. I. Baskes, Embedded-atom method: Derivation and application to impurities, surfaces, and other defects in metals, Phys. Rev. B 29 (1984) 6443. doi:10.1103/PhysRevB.29.6443.

[39] M. W. Finnis, J. E. Sinclair, A simple empirical N-Body potential for transition metals, Philos. Mag. A 50 (1984) 45.

[40] V. Rosato, M. Guillope, B. Legrand, Philos. Mag. A 59 (1989) 321.

[41] J. Luo, B. Legrand, Phys. Rev. B 38 (1988) 1728.

[42] M. S. Daw, S. M. Foiles, M. I. Baskes, The embedded-atom method: a review of theory and applications, Mater. Sci. Reports 9 (7-8) (1993) 251. doi:10.1016/0920-2307(93)90001-U.

[43] P. M. Derlet, D. Nguyen-Manh, S. L. Dudarev, Multiscale modeling of crowdion and vacancy defects in body-centered-cubic transition metals, Phys. Rev. B 76 (2007) 054107. doi:10.1103/PhysRevB.76.054107.

[44] M.-C. Marinica, L. Ventelon, M. R. Gilbert, L. Proville, S. L. Dudarev, J. Marian, G. Bencteux, F. Willaime, Interatomic potentials for modelling radiation defects and dislocations in tungsten, J. Phys.: Cond. Mater. 25 (39) (2013) 395502. doi:10.1088/0953-8984/25/39/395502.

[45] G. J. Ackland, M. I. Mendelev, D. J. Srolovitz, S. Han, A. V. Barashev, Development of an interatomic potential for phosphorus impurities in α-iron, J. Phys.: Condens. Matter 16 (27) (2004) S2629. doi:10.1088/0953-8984/16/27/003.

[46] L. Malerba, M.-C. Marinica, N. Anento, C. Björkas, H. Nguyen, C. Domain, F. Djurabekova, P. Olsson, K. Nordlund, A. Serra, D. Terentyev, F. Willaime, C. S. Becquart, Comparison of empirical interatomic potentials for iron applied to radiation damage studies, J. Nucl. Mater. 406 (1) (2010) 19. doi:10.1016/j.jnucmat.2010.05.017.

[47] M.-C. Marinica, F. Willaime, J.-P. Crocombette, Irradiation-induced formation of nanocrystallites with $c15$ laves phase structure in bcc iron, Phys. Rev. Lett. 108 (2012) 025501. doi:10.1103/PhysRevLett.108.025501.

[48] D. R. Mason, D. Nguyen-Manh, C. S. Becquart, An empirical potential for simulating vacancy clusters in tungsten, Journal of Physics: Condensed Matter 29 (50) (2017) 505501. doi:10.1088/1361-648x/aa9776.

[49] A. M. Goryaeva, J.-B. Maillet, M.-C. Marinica, Towards better efficiency of interatomic linear machine learning potentials, Comp. Mater. Sci. 166 (2019) 200 – 209. doi:https://doi.org/10.1016/j.commatsci.2019.04.043.

[50] J. Dérès, A. M. Goryaeva, C. Lapointe, P. Grigorev, T. Swinburne, J. Kermode, M.-C. Marinica, Machine learning potentials for irradiation defects in Fe and W, arXiv:1702.07042v1 [physics.comp-ph].

[51] W. J. Szlachta, A. P. Bartók, G. Csányi, Accuracy and transferability of gaussian approximation potential models for tungsten, Phys. Rev. B 90 (2014) 104108. doi:10.1103/PhysRevB.90.104108.

[52] J. Byggmästar, A. Hamedani, K. Nordlund, F. Djurabekova, Machine-learning interatomic potential for radiation damage and defects in tungsten, Phys. Rev. B 100 (2019) 144105. doi:10.1103/PhysRevB.100.144105.

[53] J. Behler, M. Parrinello, Generalized neural-network representation of high-dimensional potential-energy surfaces, Phys. Rev. Lett. 98 (2007) 146401. doi:10.1103/PhysRevLett.98.146401.

[54] A. M. Goryaeva, C. Lapointe, C. Dai, J. Drs, J.-B. Maillet, M.-C. Marinica, Reinforcing materials modelling by encoding the structures of defects in crystalline solids into distortion scores, Nature Communications 11 (2020) 4691. doi:10.1038/s41467-020-18282-2.

[55] A. P. Bartók, Gaussian approximation potential : an interatomic potential derived from first principles quantum mechanics, Ph.D. thesis, University of Cambridge (2009).

[56] A. P. Bartók, R. Kondor, G. Csányi, On representing chemical environments, Phys. Rev. B 87 (2013) 184115. doi:10.1103/PhysRevB.87.184115.

[57] A. Shapeev, Moment tensor potentials: A class of systematically improvable interatomic potentials, Multiscale Model. Sim. 14 (3) (2016) 1153–1173. doi:10.1137/15M1054183.

[58] E. V. Podryabinkin, A. V. Shapeev, Active learning of linearly parametrized interatomic potentials, Comput. Mater. Sci. 140 (2017) 171–180. doi:10.1016/j.commatsci.2017.08.031.

[59] M. Eickenberg, G. Exarchakis, M. Hirn, S. Mallat, Solid harmonic wavelet scattering: Predicting quantum molecular energy from invariant descriptors of 3d electronic densities, in: I. Guyon, U. V. Luxburg, S. Bengio, H. Wallach, R. Fergus, S. Vishwanathan, R. Garnett (Eds.), Advances in Neural Information Processing Systems 30, Curran Associates, Inc., 2017, p. 65406549.

[60] M. Hirn, S. Georges Mallat, N. Poilvert, Wavelet scattering regression of quantum chemical energies, Multiscale Modeling Simulation 15.

[61] G. Ferre, J.-B. Maillet, G. Stoltz, Permutation-invariant distance between atomic configurations, J. Chem. Phys. 143 (10) (2015) 104114. doi:10.1063/1.4930541.

[62] G. Ferré, T. Haut, K. Barros, Learning molecular energies using localized graph kernels, J. Chem. Phys. 146 (11) (2017) 114107. doi:10.1063/1.4978623.

[63] K. T. Schütt, F. Arbabzadah, S. Chmiela, K. R. Müller, A. Tkatchenko, Quantum-chemical insights from deep tensor neural networks, Nat. Commun. 8 (2017) 1–8. doi:10.1038/ncomms13890.

[64] K. T. Schütt, M. Gastegger, A. Tkatchenko, K.-R. Müller, R. J. Maurer, Unifying machine learning and quantum chemistry with a deep neural network for molecular wavefunctions, Nature Commun. 10 (1) (2019) 5024. doi:10.1038/s41467-019-12875-2.

[65] F. Noe, C. Clementi, Kinetic Distance and Kinetic Maps from Molecular Dynamics Simulation, Journal of Chemical Theory and Computation 11 (10) (2015) 5002–5011.

[66] F. Noé, S. Olsson, J. Köhler, H. Wu, Boltzmann generators: Sampling equilibrium states of many-body systems with deep learning, Science 365 (6457).

[67] A. P. Thompson, L. P. Swiler, C. R. Trott, S. M. Foiles, G. J. Tucker, Spectral neighbor analysis method for automated generation of quantum-accurate interatomic potentials, J. Comp. Phys. 285 (2015) 316. doi:10.1016/j.jcp.2014.12.018.

[68] M. A. Wood, A. P. Thompson, Quantum-accurate molecular dynamics potential for tungsten, arXiv:1702.07042v1 [physics.comp-ph].

[69] M. A. Wood, A. P. Thompson, Extending the accuracy of the snap interatomic potential form, J. Chem. Phys. 148 (24). doi:10.1063/1.5017641.

[70] C. Chen, Z. Deng, R. Tran, H. Tang, I.-H. Chu, S. P. Ong, Accurate force field for molybdenum by machine learning large materials data, Phys. Rev. Materials 1 (2017) 043603. doi:10.1103/PhysRevMaterials.1.043603.

[71] C. Lapointe, T. D. Swinburne, L. Thiry, S. Mallat, L. Proville, C. S. Becquart, M.-C. Marinica, Machine learning surrogate models for prediction of point defect vibrational entropy, Phys. Rev. Materials 4 (2020) 063802. doi:10.1103/PhysRevMaterials.4.063802.

[72] J. Behler, Atom-centered symmetry functions for constructing high-dimensional neural network potentials, J. Chem. Phys. 134 (7) (2011) 074106. doi:10.1063/1.3553717.

[73] N. Artrith, A. Urban, An implementation of artificial neural-network potentials for atomistic materials simulations: Performance for TiO2, Comp. Mater. Sci. 114 (2016) 135–150. doi:10.1016/j.commatsci.2015.11.047.

[74] J. Behler, Perspective: Machine learning potentials for atomistic simulations, J. Chem. Phys. 145 (17) (2016) 170901. doi:10.1063/1.4966192.

[75] E. Cubuk, S. Schoenholz, J. Rieser, B. Malone, J. Rottler, D. Durian, E. Kaxiras, A. Liu, Identifying Structural Flow Defects in Disordered Solids Using Machine-Learning Methods, Phys. Rev. Lett. 114 (10) (2015) 108001. doi:10.1103/PhysRevLett.114.108001.

[76] A. P. Bartók, G. Csányi, Gaussian approximation potentials: A brief tutorial introduction, Int. J. Quantum Chem. 115 (16) (2015) 1051–1057. doi:10.1002/qua.24927.

[77] T. Hofmann, B. Schlkopf, A. J. Smola, Kernel methods in machine learning, Ann. Statist. 36 (3) (2008) 1171–1220. doi:10.1214/009053607000000677.

[78] V. Botu, R. Batra, J. Chapman, R. Ramprasad, Machine Learning Force Fields: Construction, Validation, and Outlook, J. Phys. Chem. C 121 (1) (2017) 511–522. doi:10.1021/acs.jpcc.6b10908.

[79] V. Botu, R. Ramprasad, Adaptive machine learning framework to accelerate ab initio molecular dynamics, Int. J. Quantum Chem. 115 (16) (2015) 1074–1083. doi:10.1002/qua.24836.

[80] V. Botu, R. Ramprasad, A learning scheme to predict atomic forces and accelerate materials simulations, arXiv:1505.02701 [cond-mat]ArXiv: 1505.02701.
URL http://arxiv.org/abs/1505.02701

[81] Z. Li, J. R. Kermode, A. De Vita, Molecular Dynamics with On-the-Fly Machine Learning of Quantum-Mechanical Forces, Phys. Rev. Lett. 114 (9) (2015) 096405. doi:10.1103/PhysRevLett.114.096405.

[82] A. P. Bartók, S. De, C. Poelking, N. Bernstein, J. R. Kermode, G. Csányi, M. Ceriotti, Machine learning unifies the modeling of materials and molecules, Sci Adv 3 (12) (2017) e1701816. doi:10.1126/sciadv.1701816.

[83] L. M. Ghiringhelli, J. Vybiral, S. V. Levchenko, C. Draxl, M. Scheffler, Big Data of Materials Science: Critical Role of the Descriptor, Phys. Rev. Lett. 114 (10) (2015) 105503. doi:10.1103/PhysRevLett.114.105503.

[84] B. Grabowski, Y. Ikeda, P. Srinivasan, F. Krmann, C. Freysoldt, A. I. Duff, A. Shapeev, J. Neugebauer, Ab initio vibrational free energies including anharmonicity for multicomponent alloys, npj Computational Materials 5 (1) (2019) 1–6. doi:10.1038/s41524-019-0218-8.

[85] A. P. Bartók, M. C. Payne, R. Kondor, G. Csányi, Gaussian approximation potentials: The accuracy of quantum mechanics, without the electrons, Phys. Rev. Lett. 104 (2010) 136403. doi:10.1103/PhysRevLett.104.136403.

[86] L. Ventelon, F. Willaime, C.-C. Fu, M. Heran, I. Ginoux, Ab initio investigation of radiation defects in tungsten: Structure of self-interstitials and specificity of di-vacancies compared to other bcc transition metals, J. Nucl. Mater. 425 (1-3) (2012) 16. doi:10.1016/j.jnucmat.2011.08.024.

[87] M. Muzyk, D. Nguyen-Manh, K. J. Kurzydłowski, N. L. Baluc, S. L. Dudarev, Phase stability, point defects, and elastic properties of w-v and w-ta alloys, Phys. Rev. B 84 (2011) 104115. doi:10.1103/PhysRevB.84.104115.

[88] A. Satta, F. Willaime, S. de Gironcoli, Vacancy self-diffusion parameters in tungsten: Finite electron-temperature lda calculations, Phys. Rev. B 57 (1998) 11184–11192.

[89] S. J. Zinkle, L. L. Snead, Opportunities and limitations for ion beams in radiation effects studies: Bridging critical gaps between charged particle and neutron irradiations, Scripta Materialia 143 (2018) 154 – 160. doi:10.1016/j.scriptamat.2017.06.041.

[90] G. S. Was, Emulating Neutron Irradiation Effects with Ions, 2017, pp. 631–665. doi:10.1007/978-1-4939-3438-6_11.

[91] G. S. Was, Challenges to the use of ion irradiation for emulating reactor irradiation, Journal of Materials Research 30 (9) (2015) 11581182. doi:10.1557/jmr.2015.73.

[92] A. Prokhodtseva, B. Décamps, R. Schäublin, Comparison between bulk and thin foil ion irradiation of ultra high purity fe, Journal of Nuclear Materials 442 (1, Supplement 1) (2013) S786 – S789, Fifteenth International Conference on Fusion Reactor Materials. doi:10.1016/j.jnucmat.2013.04.032.

[93] K. Arakawa, K. Ono, M. Isshiki, K. Mimura, M. Uchikoshi, H. Mori, Observation of the one-dimensional diffusion of nanometer-sized dislocation loops, Science 318 (5852) (2007) 956–959. doi:10.1126/science.1145386.

[94] D. Terentyev, N. Anento, A. Serra, V. Jansson, H. Khater, G. Bonny, Interaction of carbon with vacancy and self-interstitial atom clusters in α-iron studied using metalliccovalent interatomic potential, Journal of Nuclear Materials 408 (3) (2011) 272 – 284. doi:10.1016/j.jnucmat.2010.11.053.

[95] D. Terentyev, I. Martin-Bragado, Evolution of dislocation loops in iron under irradiation: The impact of carbon, Scripta Materialia 97 (2015) 5 – 8. doi:10.1016/j.scriptamat.2014.10.021.

[96] C. Varvenne, F. Bruneval, M.-C. Marinica, E. Clouet, Point defect modeling in materials: Coupling *ab initio* and elasticity approaches, Phys. Rev. B 88 (2013) 134102. doi:10.1103/PhysRevB.88.134102.

[97] P.-W. Ma, S. L. Dudarev, CALANIE: Anisotropic elastic correction to the total energy, to mitigate the effect of periodic boundary conditions, Computer Physics Communications 252 (2020) 107130. doi:10.1016/j.cpc.2019.107130.

[98] S. L. Dudarev, A. P. Sutton, Elastic interactions between nano-scale defects in irradiated materials, Acta Mater. 125 (2017) 425–430.

[99] S. L. Dudarev, M. R. Gilbert, K. Arakawa, H. Mori, Z. Yao, M. L. Jenkins, P. M. Derlet, Langevin model for real-time brownian dynamics of interacting nanodefects in irradiated metals, Phys. Rev. B 81 (2010) 224107. doi:10.1103/PhysRevB.81.224107.

[100] S. L. Dudarev, K. Arakawa, X. Yi, Z. Yao, M. L. Jenkins, M. R. Gilbert, P. M. Derlet, Spatial ordering of nano-dislocation loops in ion-irradiated materials, Journal of Nuclear Materials 455 (1) (2014) 16 – 20, proceedings of the 16th International Conference on Fusion Reactor Materials (ICFRM-16). doi:10.1016/j.jnucmat.2014.02.032.

[101] O. El-Atwani, E. Aydogan, E. Esquivel, M. Efe, Y. Wang, S. Maloy, Detailed transmission electron microscopy study on the mechanism of dislocation loop rafting in tungsten, Acta Materialia 147 (2018) 277 – 283. doi:10.1016/j.actamat.2018.01.003.

[102] D. R. Mason, X. Yi, M. A. Kirk, S. L. Dudarev, Elastic trapping of dislocation loops in cascades in ion-irradiated tungsten foils, Journal of Physics: Condensed Matter 26 (37) (2014) 375701. doi:10.1088/0953-8984/26/37/375701.

[103] B. N. Singh, S. J. Zinkle, Influence of irradiation parameters on damage accumulation in metals and alloys, Journal of Nuclear Materials 217 (1) (1994) 161 – 171. doi:10.1016/0022-3115(94)90316-6.

[104] H. Heinisch, H. Trinkaus, B. Singh, Kinetic monte carlo studies of the reaction kinetics of crystal defects that diffuse one-dimensionally with occasional transverse migration, Journal of Nuclear Materials 367-370 (2007) 332 – 337, proceedings of the Twelfth International Conference on Fusion Reactor Materials (ICFRM-12). doi:10.1016/j.jnucmat.2007.03.034.

[105] Y.-R. Lin, S. J. Zinkle, Cavity denuded zone in dual beam irradiated Fe and Fe-Cr alloys, Tech. Rep. DOE-ER-0313/66, ORNL Semiannual progress report, section 1.3 (2019).

[106] X. Yi, A. E. Sand, D. R. Mason, M. A. Kirk, S. G. Roberts, K. Nordlund, S. L. Dudarev, Direct observation of size scaling and elastic interaction between nano-scale defects in collision cascades, EPL (Europhysics Letters) 110 (3) (2015) 36001. doi:10.1209/0295-5075/110/36001.

[107] A. E. Sand, M. J. Aliaga, M. J. Caturla, K. Nordlund, Surface effects and statistical laws of defects in primary radiation damage: Tungsten vs. iron, EPL (Europhysics Letters) 115 (3) (2016) 36001.
URL http://stacks.iop.org/0295-5075/115/i=3/a=36001

[108] R. Schäublin, B. Décamps, A. Prokhodtseva, J. Löffler, On the origin of primary 1/2 a0 ⟨111⟩ and a0 ⟨100⟩ loops in irradiated fe(cr) alloys, Acta Materialia 133 (2017) 427 – 439. doi:10.1016/j.actamat.2017.02.041.

[109] M. L. Jenkins, C. A. English, B. L. Eyre, Heavy-ion irradiation of a-iron, Philosophical Magazine A 38 (1) (1978) 97–114. doi:10.1080/01418617808239220.

[110] Z. Yao, M. Hernández-Mayoral, M. Jenkins, M. Kirk, Heavy-ion irradiations of fe and fecr model alloys part 1: Damage evolution in thin-foils at lower doses, Phil. Mag. 88 (2008) 2851–2880.

[111] M. Jenkins, M. Kirk, Characterization of Radiation Damage by Transmission Electron Microscopy, Series in Microscopy in Materials Science, IOP, Bristol, 2001.

[112] P. M. Derlet, M. R. Gilbert, S. L. Dudarev, Simulating dislocation loop internal dynamics and collective diffusion using stochastic differential equations, Phys. Rev. B 84 (2011) 134109. doi:10.1103/PhysRevB.84.134109.

[113] J. Fikar, R. Gröger, R. Schäublin, Interaction of irradiation-induced prismatic dislocation loops with free surfaces in tungsten, Nuclear Instruments and Methods in Physics Research Section B: Beam Interactions with Materials and Atoms 393 (2017) 186 – 189, computer Simulation of Radiation effects in Solids Proceedings of the 13 COSIRES Loughborough, UK, June 19-24 2016. doi:10.1016/j.nimb.2016.10.006.

[114] A. F. Voter, Introduction to the kinetic monte carlo method, in: K. E. Sickafus, E. A. Kotomin, B. P. Uberuaga (Eds.), Radiation Effects in Solids, Springer Netherlands, Dordrecht, 2007, pp. 1–23.

[115] J. P. Balbuena, M. J. Caturla, E. Martinez, Kinetic Monte Carlo Algorithms for Nuclear Materials Applications, Springer International Publishing, Cham, 2018, pp. 1–22. doi:10.1007/978-3-319-50257-1_120-1.

[116] S. Hu, V. Joshi, C. A. Lavender, A rate-theoryphase-field model of irradiation-induced recrystallization in UMo nuclear fuelss, JOM 69 (2017) 2554–2562. doi:10.1007/s11837-017-2611-4.

[117] S. Hu, W. Setyawan, B. W. Beeler, J. Gan, D. E. Burkes, Defect cluster and nonequilibrium gas bubble associated growth in irradiated UMo fuels – a cluster dynamics and phase field model, Journal of Nuclear Materials 542 (2020) 152441. doi:https://doi.org/10.1016/j.jnucmat.2020.152441.

[118] S. Hu, D. Burkes, C. A. Lavender, V. Joshi, Effect of grain morphology on gas bubble swelling in UMo fuels – a 3D microstructure dependent booth model, Journal of Nuclear Materials 480 (2016) 323–331. doi:https://doi.org/10.1016/j.jnucmat.2016.08.038.

[119] L. Messina, T. Schuler, M. Nastar, M.-C. Marinica, P. Olsson, Solute diffusion by self-interstitial defects and radiation-induced segregation in ferritic Fe-X (X=Cr, Cu, Mn, Ni, P, Si) dilute alloys, Acta Materialia 191 (2020) 166–185. doi:https://doi.org/10.1016/j.actamat.2020.03.038.

[120] L. Thuinet, M. Nastar, E. Martinez, G. Bouobda Moladje, A. Legris, F. Soisson, Multiscale modeling of radiation induced segregation in iron based alloys, Computational Materials Science 149 (2018) 324–335. doi:https://doi.org/10.1016/j.commatsci.2018.03.024.

[121] M. R. Tonks, A. Cheniour, L. Aagesen, How to apply the phase field method to model radiation damage, Computational Materials Science 147 (2018) 353–362. doi:https://doi.org/10.1016/j.commatsci.2018.02.007.

[122] M. R. Tonks, L. K. Aagesen, The phase field method: Mesoscale simulation aiding material discovery, Annual Review of Materials Research 49 (1) (2019) 79–102. doi:10.1146/annurev-matsci-070218-010151.

[123] C. Liu, L. He, Y. Zhai, B. Tyburska-Püschel, P. M. Voyles, K. Sridharan, D. Morgan, I. Szlufarska, Evolution of small defect clusters in ion-irradiated 3C-SiC: Combined cluster dynamics modeling and experimental study, Acta Materialia 125 (2017) 377–389.

[124] B. C. Larson, Historical perspective on diffraction line-profile analyses for crystals containing defect clusters, Crystals 9 (2019) 257.

[125] A. E. Sand, D. R. Mason, A. De Backer, X. Yi, S. L. Dudarev, K. Nordlund, Cascade fragmentation: deviation from power law in primary radiation damage, Materials Research Letters 5 (5) (2017) 357–363. doi:10.1080/21663831.2017.1294117.

[126] A. Prokhodtseva, B. Décamps, A. Ramar, R. Schäublin, Impact of he and cr on defect accumulation in ion-irradiated ultrahigh-purity fe(cr) alloys, Acta Materialia 61 (18) (2013) 6958 – 6971. doi:10.1016/j.actamat.2013.08.007.

[127] D. R. Mason, X. Yi, A. E. Sand, S. L. Dudarev, Experimental observation of the number of visible defects produced in individual primary damage cascades in irradiated tungsten, EPL (Europhysics Letters) 122 (6) (2018) 66001. doi:10.1209/0295-5075/122/66001.

[128] D. Mason, A. Sand, X. Yi, S. Dudarev, Direct observation of the spatial distribution of primary cascade damage in tungsten, Acta Materialia 144 (2018) 905 – 917. doi:10.1016/j.actamat.2017.10.031.

[129] T. D. Swinburne, P.-W. Ma, S. L. Dudarev, Low temperature diffusivity of self-interstitial defects in tungsten, New Journal of Physics 19 (7) (2017) 073024. doi:10.1088/1367-2630/aa78ea.

[130] C. Becquart, C. Domain, U. Sarkar, A. De Backer, M. Hou, Microstructural evolution of irradiated tungsten: Ab initio parameterisation of an okmc model, Journal of Nuclear Materials 403 (1) (2010) 75 – 88. doi:10.1016/j.jnucmat.2010.06.003.

[131] G. S. Was, S. Taller, Z. Jiao, A. M. Monterrosa, D. Woodley, D. Jennings, T. Kubley, F. Naab, O. Toader, E. Uberseder, Resolution of the carbon contamination problem in ion irradiation experiments, Nuclear Instruments and Methods in Physics Research Section B: Beam Interactions with Materials and Atoms 412 (2017) 58–65. doi:10.1016/j.nimb.2017.08.039.

[132] P. Alberry, C. Haworth, Interdiffusion of cr, mo, and w in iron, Metal Science 8.

[133] R. Braun, M. Feller-Kniepmeier, Diffusion of chromium in a-iron, Phys. Stat. Sol. (a) 90 (1985) 553.

[134] S. Dubiel, G. Inden, On the miscibility gap in the fe-cr system: A moessbauer study on long term annealed alloys, Z. Metallkde 78 (1987) 544–549.

[135] M. Bachhav, G. R. Odette, E. A. Marquis, alpha ' precipitation in neutron-irradiated fe-cr alloys, Scripta Materialia 74 (2014) 48–51. doi:10.1016/j.scriptamat.2013.10.001.

[136] F. Bergner, C. Pareige, V. Kuksenko, L. Malerba, P. Pareige, A. Ulbricht, A. Wagner, Critical assessment of cr-rich precipitates in neutron-irradiated fe12at%cr: Comparison of sans and apt, Journal of Nuclear Materials 442 (1-3) (2013) 463–469. doi:10.1016/j.jnucmat.2013.05.023.

[137] F. Bergner, A. Ulbricht, C. Heintze, Estimation of the solubility limit of cr in fe at 300 c from small-angle neutron scattering in neutron-irradiated fecr alloys, Scripta Materialia 61 (11) (2009) 1060–1063. doi:10.1016/j.scriptamat.2009.08.028.

[138] W.-Y. Chen, Y. Miao, Y. Wu, C. A. Tomchik, K. Mo, J. Gan, M. A. Okuniewski, S. A. Maloy, J. F. Stubbins, Atom probe study of irradiation-enhanced precipitation in neutron-irradiated fecr model alloys, Journal of Nuclear Materials 462 (2015) 242–249. doi:10.1016/j.jnucmat.2015.04.005.

[139] V. Kuksenko, C. Pareige, C. Genevois, F. Cuvilly, M. Roussel, P. Pareige, Effect of neutron-irradiation on the microstructure of a fe12at.%cr alloy, Journal of Nuclear Materials 415 (1) (2011) 61–66. doi:10.1016/j.jnucmat.2011.05.042.

[140] V. Kuksenko, C. Pareige, P. Pareige, Cr precipitation in neutron irradiated industrial purity fecr model alloys, Journal of Nuclear Materials 432 (1-3) (2013) 160–165. doi:10.1016/j.jnucmat.2012.07.021.

[141] O. Anderoglu, J. Van den Bosch, P. Hosemann, E. Stergar, B. H. Sencer, D. Bhattacharyya, R. Dickerson, P. Dickerson, M. Hartl, S. A. Maloy, Phase stability of an ht-9 duct irradiated in fftf, Journal of Nuclear Materials 430 (1) (2012) 194–204. doi:10.1016/j.jnucmat.2012.06.038.

[142] M. H. Mathon, Y. de Carlan, G. Geoffroy, X. Averty, A. Alamo, C. H. de Novion, A sans investigation of the irradiation-enhanced phases separation in 712 cr martensitic steels, Journal of Nuclear Materials 312 (23) (2003) 236–248. doi:10.1016/S0022-3115(02)01630-6.

[143] E. Reese, M. Bachhav, P. Wells, Y. Yamamoto, G. R. Odette, E. Marquis, On composition in thermally annealed and neutron-irradiated fe- 9-18cr alloys, Journal of Nuclear Materials 500 (2018) 192–198.

[144] E. A. Marquis, R. Hu, T. Rousseau, A systematic approach for the study of radiation-induced segregation/depletion at grain boundaries in steels, Journal of Nuclear Materials 413 (1) (2011) 1–4. doi:10.1016/j.jnucmat.2011.03.023.

[145] E. A. Marquis, B. Wirth, G. S. Was, G. R. Odette, R. Mathew, A. Selby, L. Yao, M. Bachhav, B. Ramirez, Characterization and modeling of grain boundary chemistry evolution in ferritic steels under irradiation, Report (2014).

[146] C. Pareige, V. Kuksenko, P. Pareige, Behaviour of p, si, ni impurities and cr in self ion irradiated fecr alloys comparison to neutron irradiation, Journal of Nuclear Materials 456 (2015) 471–476. doi:10.1016/j.jnucmat.2014.10.024.

[147] E. R. Reese, N. Almirall, T. Yamamoto, S. Tumey, G. Robert Odette, E. A. Marquis, Dose rate dependence of cr precipitation in an ion-irradiated fe18cr alloy, Scripta Materialia 146 (2018) 213–217. doi:10.1016/j.scriptamat.2017.11.040.

[148] R. W. Harrison, A. W. Carruthers, J. A. Hinks, M. G. Burke, S. E. Donnelly, Cascade size and dose rate effects on precipitation in ion-irradiated fe14cr alloy, Scripta Materialia 172 (2019) 33–37. doi:10.1016/j.scriptamat.2019.06.034.

[149] O. Tissot, C. Pareige, E. Meslin, B. Decamps, J. Henry, Kinetics of precipitation in an electron-irradiated fe15cr alloy, Scripta Materialia 122 (2016) 31–35. doi:10.1016/j.scriptamat.2016.05.021.

[150] F. Soisson, T. Jourdan, Radiation-accelerated precipitation in fecr alloys, Acta Materialia 103 (2016) 870–881. doi:10.1016/j.actamat.2015.11.001.

[151] J.-H. Ke, E. R. Reese, E. A. Marquis, G. R. Odette, D. Morgan, Flux effects in precipitation under irradiation simulation of fe-cr alloys, Acta Materialia 164 (2019) 586–601. doi:10.1016/j.actamat.2018.10.063.

[152] S. J. Zinkle, L. L. Snead, Opportunities and limitations for ion beams in radiation effects studies: Bridging critical gaps between charged particle and neutron irradiations, Scripta Materialia 143 (2018) 154–160. doi:10.1016/j.scriptamat.2017.06.041.

[153] S. Shu, B. D. Wirth, P. B. Wells, D. D. Morgan, G. R. Odette, Multi-technique characterization of the precipitates in thermally aged and neutron irradiated fe-cu and fe-cu-mn model alloys: Atom probe tomography reconstruction implications, Acta Materialia 146 (2018) 237–252. doi:10.1016/j.actamat.2017.12.006.

[154] G. R. Odette, M. J. Alinger, B. D. Wirth, Recent developments in irradiation-resistant steels, Annual Review of Materials Research 38 (1) (2008) 471–503. doi:10.1146/annurev.matsci.38.060407.130315.

[155] C. A. Williams, D. Haley, E. A. Marquis, G. D. W. Smith, M. P. Moody, Defining clusters in apt reconstructions of ods steels, Ultramicroscopy 132 (2013) 271–278. doi:10.1016/j.ultramic.2012.12.011.

[156] C. A. Williams, E. A. Marquis, A. Cerezo, G. D. W. Smith, Nanoscale characterisation of odseurofer 97 steel: An atom-probe tomography study, Journal of Nuclear Materials 400 (1) (2010) 37–45. doi:10.1016/j.jnucmat.2010.02.007.

[157] C. Hatzoglou, B. Radiguet, G. Da Costa, P. Pareige, M. Roussel, M. Hernandez-Mayoral, C. Pareige, Quantification of apt physical limitations on chemical composition of precipitates in fecr alloys, Journal of Nuclear Materials 522 (2019) 64–73. doi:10.1016/j.jnucmat.2019.05.022.

[158] E. A. Marquis, F. Vurpillot, Chromatic aberrations in the field evaporation behavior of small precipitates, Microscopy and Microanalysis 14 (6) (2008) 561–570. doi:10.1017/S1431927608080793.

[159] C. Oberdorfer, T. Withrow, L. J. Yu, K. Fisher, E. A. Marquis, W. Windl, Influence of surface relaxation on solute atoms positioning within atom probe tomography reconstructions, Materials Characterization 146 (2018) 324–335. doi:10.1016/j.matchar.2018.05.014.

[160] I. Ghamarian, L.-J. Yu, E. Marquis, Quantification of solute topology in atom probe tomography data: application to the microstructure of a proton-irradiated alloy 625, Metall. Mater. Trans A.

[161] J. Hyde, C. English, An analysis of the structure of irradiation induced cu- enriched clusters in low and high nickel welds, in: Microstructural Processes in Irradiated Materials, Fall MRS.

[162] Y. Dong, A. Etienne, A. Frolov, S. Fedotova, K. Fujii, K. Fukuya, C. Hatzoglou, E. Kuleshova, K. Lindgren, A. London, A. Lopez, S. Lozano-Perez, Y. Miyahara, Y. Nagai, K. Nishida, B. Radiguet, D. K. Schreiber, N. Soneda, M. Thuvander, T. Toyama, J. Wang, F. Sefta, P. Chou, E. A. Marquis, Atom probe tomography interlaboratory study on clustering analysis in experimental data using the maximum separation distance approach, Microscopy and Microanalysis 25 (2) (2019) 356–366. doi:10.1017/S1431927618015581.

[163] L. T. Stephenson, M. P. Moody, P. V. Liddicoat, S. P. Ringer, New techniques for the analysis of fine-scaled clustering phenomena within atom probe tomography (apt) data, Microscopy and Microanalysis 13 (6) (2007) 448–463. doi:10.1017/s1431927607070900.

[164] I. Ghamarian, E. A. Marquis, Hierarchical density-based cluster analysis framework for atom probe tomography data, Ultramicroscopy 200 (2019) 28–38. doi:10.1016/j.ultramic.2019.01.011.

[165] Y. Zhao, J. Marian, Direct prediction of the solute softening-to-hardening transition in w–re alloys using stochastic simulations of screw dislocation motion, Modelling and Simulation in Materials Science and Engineering 26 (4) (2018) 045002.

[166] C.-H. Huang, L. Gharaee, Y. Zhao, P. Erhart, J. Marian, Mechanism of nucleation and incipient growth of re clusters in irradiated w-re alloys from kinetic monte carlo simulations, Physical Review B 96 (9) (2017) 094108.

[167] P. D. Edmondson, B. Gault, M. R. Gilbert, An atom probe tomography and inventory calculation examination of second phase precipitates in neutron irradiated single crystal tungsten, Nuclear Fusion 60 (12) (2020) 126013.

[168] X. Hu, T. Koyanagi, M. Fukuda, N. K. Kumar, L. L. Snead, B. D. Wirth, Y. Katoh, Irradiation hardening of pure tungsten exposed to neutron irradiation, Journal of Nuclear Materials 480 (2016) 235–243.

[169] Y. Katoh, L. Snead, L. Garrison, X. Hu, T. Koyanagi, C. Parish, P. Edmondson, M. Fukuda, T. Hwang, T. Tanaka, et al., Response of unalloyed tungsten to mixed spectrum neutrons, Journal of Nuclear Materials 520 (2019) 193–207.

[170] M. Gilbert, J.-C. Sublet, Neutron-induced transmutation effects in w and w-alloys in a fusion environment, Nuclear Fusion 51 (4) (2011) 043005.

[171] T. Hwang, A. Hasegawa, K. Tomura, N. Ebisawa, T. Toyama, Y. Nagai, M. Fukuda, T. Miyazawa, T. Tanaka, S. Nogami, Effect of neutron irradiation on rhenium cluster formation in tungsten and tungsten-rhenium alloys, Journal of Nuclear Materials 507 (2018) 78–86.

[172] A. Xu, C. Beck, D. E. Armstrong, K. Rajan, G. D. Smith, P. A. Bagot, S. G. Roberts, Ion-irradiation-induced clustering in W-Re and W-Re-Os alloys: A comparative study using atom probe tomography and nanoindentation measurements, Acta Materialia 87 (2015) 121 – 127. doi:10.1016/j.actamat.2014.12.049.

[173] J. Wróbel, D. Nguyen-Manh, K. Kurzydłowski, S. Dudarev, A first-principles model for anomalous segregation in dilute ternary tungsten-rhenium-vacancy alloys, Journal of Physics: Condensed Matter 29 (14) (2017) 145403.

[174] M. Hossain, J. Marian, Stress-dependent solute energetics in w–re alloys from first-principles calculations, Acta materialia 80 (2014) 107–117.

[175] L. Gharaee, J. Marian, P. Erhart, The role of interstitial binding in radiation induced segregation in w-re alloys, Journal of Applied Physics 120 (2) (2016) 025901.

[176] M. J. Lloyd, R. G. Abernethy, D. E. Armstrong, P. A. Bagot, M. P. Moody, E. Martinez, D. Nguyen-Manh, Radiation-induced segregation in w-re: from kinetic monte carlo simulations to atom probe tomography experiments, The European Physical Journal B 92 (10) (2019) 1–12.

[177] C.-H. Huang, M. R. Gilbert, J. Marian, Simulating irradiation hardening in tungsten under fast neutron irradiation including re production by transmutation, Journal of Nuclear Materials 499 (2018) 204–215.

[178] S. J. Zinkle, N. A. M. Ghoniem, Operating temperature windows for fusion reactor structural materials, Fusion Engineering and Design 51-52 (2000) 55.

[179] S. J. Zinkle, G. A. Was, Materials challenges in nuclear energy,, Acta Mater. 61 (2013) 735–758, the Diamond Jubilee Issue. doi:10.1016/j.actamat.2012.11.004.

[180] P. M. Derlet, S. L. Dudarev, Microscopic structure of a heavily irradiated material, Physical Review Materials 4 (2020) 023605. doi:10.1103/PhysRevMaterials.4.023605.

[181] M. P. Surh, J. B. Sturgeon, W. G. Wolfer, Void nucleation, growth, and coalescence in irradiated metals, Journal of Nuclear Materials 378 (2008) 86 – 97. doi:10.1016/j.jnucmat.2008.05.009.

[182] C. H. Woo, B. N. Singh, The concept of production bias and its possible role in defect accumulation under cascade damage conditions, physica status solidi (b) 159 (1990) 609 – 616.

[183] C. H. Woo, B. N. Singh, F. A. Garner, Production bias: a proposed modification of the driving force for void swelling under cascade damage conditions, Journal of Nuclear Materials 191-194 (1992) 1224 – 1228.

[184] C. H. Woo, A. A. Semenov, F. A. Garner, Analysis of microstructural evolution driven by production bias, Journal of Nuclear Materials 206 (1993) 170 – 199.

[185] S. L. Dudarev, D. R. Mason, E. Tarleton, P.-W. Ma, A. E. Sand, Multiscale model for stresses, strains and swelling of reactor components under irradiation, Nuclear Fusion 58 (2018) 126002. doi:10.1088/1741-4326/aadb48.

[186] S. J. Zinkle, Advanced materials for fusion technology, Fusion Engineering and Design 74 (1) (2005) 31 – 40, proceedings of the 23rd Symposium of Fusion Technology. doi:10.1016/j.fusengdes.2005.08.008.

[187] I. Cook, Materials research for fusion energy, Nature Materials 5 (2006) 77 – 80. doi:10.1038/nmat1584.

[188] T. Muroga, M. Gasparotto, S. J. Zinkle, Overview of materials research for fusion reactors, Fusion Engineering and Design 61-62 (2002) 13 – 25. doi:10.1016/S0920-3796(02)00219-3.

[189] S. J. Zinkle, J. P. Blanchard, R. W. Callis, C. E. Kessel, R. J. Kurtz, P. J. Lee, K. A. McCarthy, N. B. Morley, F. Najmabadi, R. E. Nygren, G. R. Tynan, D. G. Whyte, R. S. Willms, B. D. Wirth, Fusion materials science and technology research opportunities now and during the iter era, Fusion Engineering and Design 89 (7) (2014) 1579 – 1585, proceedings of the 11th International Symposium on Fusion Nuclear Technology-11 (ISFNT-11) Barcelona, Spain, 15-20 September, 2013. doi:10.1016/j.fusengdes.2014.02.048.

[190] R. Pitts, S. Carpentier, F. Escourbiac, T. Hirai, V. Komarov, S. Lisgo, A. Kukushkin, A. Loarte, M. Merola, A. Sashala Naik, R. Mitteau, M. Sugihara, B. Bazylev, P. Stangeby, A full tungsten divertor for iter: Physics issues and design status, Journal of Nuclear Materials 438 (2013) S48 – S56, proceedings of the 20th International Conference on Plasma-Surface Interactions in Controlled Fusion Devices. doi:10.1016/j.jnucmat.2013.01.008.

[191] T. Loewenhoff, A. Bürger, J. Linke, G. Pintsuk, A. Schmidt, L. Singheiser, C. Thomser, Evolution of tungsten degradation under combined high cycle edge-localized mode and steady-state heat loads, Physica Scripta T145 (2011) 014057. doi:10.1088/0031-8949/2011/t145/014057.

[192] R. Abernethy, Predicting the performance of tungsten in a fusion environment: a literature review, Materials Science and Technology 33 (4) (2017) 388–399. doi:10.1080/02670836.2016.1185260.

[193] M. Baldwin, R. Doerner, Helium induced nanoscopic morphology on tungsten under fusion relevant plasma conditions, Nuclear Fusion 48 (3) (2008) 035001. doi:10.1088/0029-5515/48/3/035001.

[194] S. Kajita, W. Sakaguchi, N. Ohno, N. Yoshida, T. Saeki, Formation process of tungsten nanostructure by the exposure to helium plasma under fusion relevant plasma conditions, Nuclear Fusion 49 (9) (2009) 095005. doi:10.1088/0029-5515/49/9/095005.

[195] M. Tokitani, S. Kajita, S. Masuzaki, Y. Hirahata, N. Ohno, T. T. and, Exfoliation of the tungsten fibreform nanostructure by unipolar arcing in the LHD divertor plasma, Nuclear Fusion 51 (10) (2011) 102001. doi:10.1088/0029-5515/51/10/102001.

[196] G. Wright, D. Brunner, M. Baldwin, R. Doerner, B. Labombard, B. Lipschultz, J. Terry, D. Whyte, Tungsten nano-tendril growth in the alcator c-mod divertor, Nuclear Fusion 52 (4) (2012) 042003. doi:10.1088/0029-5515/52/4/042003.

[197] P. D. Edmondson, A. Xu, L. R. Hanna, M. Dagan, S. G. Roberts, L. L. Snead, Atomic scale, 3-dimensional characterization of radiation effects in tungsten for fusion applications, Microscopy and Microanalysis 21 (S3) (2015) 579580. doi:10.1017/S1431927615003694.

[198] M. Klimenkov, U. Jntsch, M. Rieth, H. Schneider, D. Armstrong, J. Gibson, S. Roberts, Effect of neutron irradiation on the microstructure of tungsten, Nuclear Materials and Energy 9 (2016) 480 – 483. doi:10.1016/j.nme.2016.09.010.

[199] X. Hu, T. Koyanagi, M. Fukuda, N. K. Kumar, L. L. Snead, B. D. Wirth, Y. Katoh, Irradiation hardening of pure tungsten exposed to neutron irradiation, Journal of Nuclear Materials 480 (2016) 235 – 243. doi:10.1016/j.jnucmat.2016.08.024.

[200] X. Hu, C. M. Parish, K. Wang, T. Koyanagi, B. P. Eftink, Y. Katoh, Transmutation-induced precipitation in tungsten irradiated with a mixed energy neutron spectrum, Acta Materialia 165 (2019) 51 – 61. doi:10.1016/j.actamat.2018.11.032.

[201] A. Xu, D. E. Armstrong, C. Beck, M. P. Moody, G. D. Smith, P. A. Bagot, S. G. Roberts, Ion-irradiation induced clustering in w-re-ta, w-re and w-ta alloys: An atom probe tomography and nanoindentation study, Acta Materialia 124 (2017) 71 – 78. doi:10.1016/j.actamat.2016.10.050.

[202] K. Henriksson, K. Nordlund, J. Keinonen, Molecular dynamics simulations of helium cluster formation in tungsten, Nuclear Instruments and Methods in Physics Research Section B: Beam Interactions with Materials and Atoms 244 (2) (2006) 377 – 391. doi:10.1016/j.nimb.2005.10.020.

[203] F. Sefta, K. D. Hammond, N. Juslin, B. D. Wirth, Tungsten surface evolution by helium bubble nucleation, growth and rupture, Nuclear Fusion 53 (7) (2013) 073015. doi:10.1088/0029-5515/53/7/073015.

[204] A. Lasa, K. Henriksson, K. Nordlund, Md simulations of onset of tungsten fuzz formation under helium irradiation, Nuclear Instruments and Methods in Physics Research Section B: Beam Interactions with Materials and Atoms 303 (2013) 156 – 161, proceedings of the 11th Computer Simulation of Radiation Effects in Solids (COSIRES) Conference Santa Fe, New Mexico, USA, July 24-29, 2012. doi:10.1016/j.nimb.2012.11.029.

[205] F. Sefta, N. Juslin, K. Hammond, B. Wirth, Molecular dynamics simulations on the effect of sub-surface helium bubbles on the sputtering yield of tungsten, Journal of Nuclear Materials 438 (2013) S493 – S496, proceedings of the 20th International Conference on Plasma-Surface Interactions in Controlled Fusion Devices. doi:10.1016/j.jnucmat.2013.01.101.

[206] A. F. Voter, Parallel replica method for dynamics of infrequent events, Phys. Rev. B 57 (1998) R13985–R13988. doi:10.1103/PhysRevB.57.R13985.

[207] A. F. Voter, A method for accelerating the molecular dynamics simulation of infrequent events, The Journal of Chemical Physics 106 (11) (1997) 4665–4677. doi:10.1063/1.473503.

[208] M. R. Sørensen, A. F. Voter, Temperature-accelerated dynamics for simulation of infrequent events, The Journal of Chemical Physics 112 (21) (2000) 9599–9606. doi:10.1063/1.481576.

[209] G. Henkelman, H. Jónsson, Long time scale kinetic monte carlo simulations without lattice approximation and predefined event table, The Journal of Chemical Physics 115 (21) (2001) 9657–9666. doi:10.1063/1.1415500.

[210] L. K. Béland, P. Brommer, F. El-Mellouhi, J.-F. m. c. Joly, N. Mousseau, Kinetic activation-relaxation technique, Phys. Rev. E 84 (2011) 046704. doi:10.1103/PhysRevE.84.046704.

[211] H. Xu, Y. N. Osetsky, R. E. Stoller, Simulating complex atomistic processes: On-the-fly kinetic monte carlo scheme with selective active volumes, Phys. Rev. B 84 (2011) 132103. doi:10.1103/PhysRevB.84.132103.

[212] B. Sadigh, P. Erhart, A. Stukowski, A. Caro, E. Martinez, L. Zepeda-Ruiz, Scalable parallel monte carlo algorithm for atomistic simulations of precipitation in alloys, Phys. Rev. B 85 (2012) 184203. doi:10.1103/PhysRevB.85.184203.

[213] E. Martínez, B. P. Uberuaga, B. D. Wirth, Atomistic modeling of helium segregation to grain boundaries in tungsten and its effect on de-cohesion, Nuclear Fusion 57 (8) (2017) 086044. doi:10.1088/1741-4326/aa6e15.

[214] W. S. Cunningham, J. M. Gentile, O. El-Atwani, C. N. Taylor, M. Efe, S. A. Maloy, J. R. Trelewicz, Softening due to grain boundary cavity formation and its competition with hardening in helium implanted nanocrystalline tungsten, ACS Appl. Mater. Interfaces 12 (19) (2018) 2897. doi:10.1021/acsami.0c01381.

[215] A. Weerasinghe, B. D. Wirth, D. Maroudas, Elastic properties of plasma-exposed tungsten predicted by molecular-dynamics simulations, Scientific Reports 8 (1) (2020) 2228722297. doi:10.1038/s41598-018-20990-1.

[216] Y. Yang, D. Frazer, M. Balooch, P. Hosemann, Irradiation damage investigation of helium implanted polycrystalline copper, Journal of Nuclear Materials 512 (2018) 137 – 143. doi:10.1016/j.jnucmat.2018.09.022.

[217] C. Becquart, C. Domain, An object kinetic monte carlo simulation of the dynamics of helium and point defects in tungsten, Journal of Nuclear Materials 385 (2) (2009) 223 – 227, nuclear Materials III. doi:10.1016/j.jnucmat.2008.11.027.

[218] K. Nordlund, C. Björkas, T. Ahlgren, A. Lasa, A. E. Sand, Multiscale modelling of plasma–wall interactions in fusion reactor conditions, Journal of Physics D: Applied Physics 47 (22) (2014) 224018. doi:10.1088/0022-3727/47/22/224018.

[219] J. Marian, C. S. Becquart, C. Domain, S. L. Dudarev, M. R. Gilbert, R. J. Kurtz, D. R. Mason, K. Nordlund, A. E. Sand, L. L. Snead, T. Suzudo, B. D. Wirth, Recent advances in modeling and simulation of the exposure and response of tungsten to fusion energy conditions, Nuclear Fusion 57 (9) (2017) 092008. doi:10.1088/1741-4326/aa5e8d.

[220] E. Martínez, A. Caro, Atomistic modeling of long-term evolution of twist boundaries under vacancy supersaturation, Phys. Rev. B 86 (2012) 214109. doi:10.1103/PhysRevB.86.214109.

[221] E. Martínez, M. J. Caturla, J. Marian, DFT-Parameterized Object Kinetic Monte Carlo Simulations of Radiation Damage, Springer International Publishing, Cham, 2018, pp. 1–32. doi:10.1007/978-3-319-50257-1_137-1.

[222] B. D. Wirth, X. Hu, A. Kohnert, D. Xu, Modeling defect cluster evolution in irradiated structural materials: Focus on comparing to high-resolution experimental characterization studies, Journal of Materials Research 30 (9) (2015) 14401455. doi:10.1557/jmr.2015.25.

[223] S. I. Golubov, R. E. Stoller, S. J. Zinkle, A. M. Ovcharenko, Kinetics of coarsening of helium bubbles during implantation and post-implantation annealing, Journal of Nuclear Materials 361 (2) (2007) 149 – 159, tMS 2007:Wechsler Symposium. doi:10.1016/j.jnucmat.2006.12.032.

[224] T. Ahlgren, K. Heinola, K. Vörtler, J. Keinonen, Simulation of irradiation induced deuterium trapping in tungsten, Journal of Nuclear Materials 427 (1) (2012) 152 – 161. doi:10.1016/j.jnucmat.2012.04.031.

[225] J. Marian, V. V. Bulatov, Stochastic cluster dynamics method for simulations of multispecies irradiation damage accumulation, Journal of Nuclear Materials 415 (1) (2011) 84 – 95. doi:10.1016/j.jnucmat.2011.05.045.

[226] J. Marian, T. L. Hoang, Modeling fast neutron irradiation damage accumulation in tungsten, Journal of Nuclear Materials 429 (1) (2012) 293 – 297. doi:10.1016/j.jnucmat.2012.06.019.

[227] J. Knap, M. Ortiz, An analysis of the quasicontinuum method, Journal of the Mechanics and Physics of Solids 49 (9) (2001) 1899–1923.

[228] J. Marian, J. Knap, M. Ortiz, Nanovoid cavitation by dislocation emission in aluminum, Physical review letters 93 (16) (2004) 165503.

[229] J. Marian, J. Knap, G. H. Campbell, A quasicontinuum study of nanovoid collapse under uniaxial loading in ta, Acta materialia 56 (10) (2008) 2389–2399.

[230] J. Marian, G. Venturini, B. Hansen, J. Knap, M. Ortiz, G. Campbell, Finite-temperature extension of the quasicontinuum method using langevin dynamics: entropy losses and analysis of errors, Modelling and Simulation in Materials Science and Engineering 18 (1) (2009) 015003.

[231] I. Uytdenhouwen, M. Decréton, T. Hirai, J. Linke, G. Pintsuk, G. Van Oost, Influence of recrystallization on thermal shock resistance of various tungsten grades, Journal of Nuclear Materials 363-365 (2007) 1099 – 1103, plasma-Surface Interactions-17. doi:10.1016/j.jnucmat.2007.01.146.

[232] M. Rieth, S. L. Dudarev, S. M. Gonzalez de Vicente, J. Aktaa, T. Ahlgren, S. Antusch, D. E. J. Armstrong, M. Balden, N. Baluc, M.-F. Barthe, W. Basuki, M. Battabyal, C. S. Becquart, D. Blagoeva, H. Boldyryeva, J. Brinkmann, M. Celino, L. Ciupinski, J. B. Correia, A. De Backer, C. Domain, E. Gaganidze, C. Garca-Rosales, J. Gibson, M. Gilbert, S. Giusepponi, B. Gludovatz, H. Greuner, K. Heinola, T. Höschen, A. Hoffmann, N. Holstein, F. Koch, W. Krauss, H. Li, S. Lindig, J. Linke, C. Linsmeier, P. López-Ruiz, H. Maier, J. Matejicek, T. P. Mishra, M. Muhammed, A. Muñoz, M. Muzyk, K. Nordlund, D. Nguyen-Manh, J. Opschoor, N. Ordás, T. Palacios, G. Pintsuk, R. Pippan, J. Reiser, J. Riesch, S. Roberts, L. Romaner, M. Rosiński, M. Sanchez, W. Schulmeyer, H. Traxler, A. Ureña, J. G. van der Laan, L. Veleva, S. Wahlberg, M. Walter, T. Weber, T. Weitkamp, S. Wurster, M. A. Yar, J. H. You, A. Zivelonghi, Recent progress in research on tungsten materials for nuclear fusion applications in europe, Journal of Nuclear Materials 432 (1) (2013) 482 – 500. doi:10.1016/j.jnucmat.2012.08.018.

[233] V. Philipps, Tungsten as material for plasma-facing components in fusion devices, Journal of Nuclear Materials 415 (1, Supplement) (2011) S2 – S9, proceedings of the 19th International Conference on Plasma-Surface Interactions in Controlled Fusion. doi:10.1016/j.jnucmat.2011.01.110.

[234] S. Wurster, N. Baluc, M. Battabyal, T. Crosby, J. Du, C. García-Rosales, A. Hasegawa, A. Hoffmann, A. Kimura, H. Kurishita, R. Kurtz, H. Li, S. Noh, J. Reiser, J. Riesch, M. Rieth, W. Setyawan, M. Walter, J.-H. You, R. Pippan, Recent progress in r&d on tungsten alloys for divertor structural and plasma facing materials, Journal of Nuclear Materials 442 (1, Supplement 1) (2013) S181 – S189, Fifteenth International Conference on Fusion Reactor Materials. doi:10.1016/j.jnucmat.2013.02.074.

[235] C. Linsmeier, M. Rieth, J. Aktaa, T. Chikada, A. Hoffmann, J. Hoffmann, A. Houben, H. Kurishita, X. Jin, M. Li, A. Litnovsky, S. Matsuo, A. von Müller, V. Nikolic, T. Palacios, R. Pippan, D. Qu, J. Reiser, J. Riesch, T. Shikama, R. Stieglitz, T. Weber, S. Wurster, J.-H. You, Z. Zhou, Development of advanced high heat flux and plasma-facing materials, Nuclear Fusion 57 (9) (2017) 092007. doi:10.1088/1741-4326/aa6f71.

[236] L. El-Guebaly, R. Kurtz, M. Rieth, H. Kurishita, A. Robinson, A. Team, W-based alloys for advanced divertor designs: Options and environmental impact of state-of-the-art alloys, Fusion Science and Technology 60 (1) (2011) 185–189. doi:10.13182/FST11-A12349.

[237] O. El-Atwani, N. Li, M. Li, A. Devaraj, J. K. S. Baldwin, M. M. Schneider, D. Sobieraj, J. S. Wróbel, D. Nguyen-Manh, S. A. Maloy, E. Martinez, Outstanding radiation resistance of tungsten-based high-entropy alloys, Science Advances 5 (3). doi:10.1126/sciadv.aav2002.

[238] O. K. Donaldson, K. Hattar, T. Kaub, G. B. Thompson, J. R. Trelewicz, Solute stabilization of nanocrystalline tungsten against abnormal grain growth, Journal of Materials Research 33 (1) (2018) 6880. doi:10.1557/jmr.2017.296.

[239] O. El-Atwani, W. Cunningham, E. Esquivel, M. Li, J. Trelewicz, B. Uberuaga, S. Maloy, In-situ irradiation tolerance investigation of high strength ultrafine tungsten-titanium carbide alloy, Acta Materialia 164 (2019) 547 – 559. doi:10.1016/j.actamat.2018.10.038.

[240] T. Chookajorn, C. A. Schuh, Thermodynamics of stable nanocrystalline alloys: A monte carlo analysis, Phys. Rev. B 89 (2014) 064102. doi:10.1103/PhysRevB.89.064102.

[241] W. S. Cunningham, K. Hattar, Y. Zhu, D. J. Edwards, J. R. Trelewicz, Suppressing irradiation induced grain growth and defect accumulation in nanocrystalline tungsten through grain boundary doping, Acta Materialia 206 (2021) 116629. doi:https://doi.org/10.1016/j.actamat.2021.116629.

[242] F. Koch, H. Bolt, Self passivating w-based alloys as plasma facing material for nuclear fusion, Physica Scripta T128 (2007) 100–105. doi:10.1088/0031-8949/2007/t128/020.

[243] P. López-Ruiz, F. Koch, N. Ordás, S. Lindig, C. García-Rosales, Manufacturing of self-passivating w-cr-si alloys by mechanical alloying and hip, Fusion Engineering and Design 86 (9) (2011) 1719 – 1723, proceedings of the 26th Symposium of Fusion Technology (SOFT-26). doi:10.1016/j.fusengdes.2011.03.107.

[244] C. García-Rosales, P. López-Ruiz, S. Alvarez-Martín, A. Calvo, N. Ordás, F. Koch, J. Brinkmann, Oxidation behaviour of bulk w-cr-ti alloys prepared by mechanical alloying and hiping, Fusion Engineering and Design 89 (7) (2014) 1611 – 1616, proceedings of the 11th International Symposium on Fusion Nuclear Technology-11 (ISFNT-11) Barcelona, Spain, 15-20 September, 2013. doi:10.1016/j.fusengdes.2014.04.057.

[245] D. Maisonnier, D. Campbell, I. Cook, L. D. Pace, L. Giancarli, J. Hayward, A. L. Puma, M. Medrano, P. Norajitra, M. Roccella, P. Sardain, M. Tran, D. Ward, Power plant conceptual studies in europe, Nuclear Fusion 47 (11) (2007) 1524–1532. doi:10.1088/0029-5515/47/11/014.

[246] T. Wegener, F. Klein, A. Litnovsky, M. Rasinski, J. Brinkmann, F. Koch, C. Linsmeier, Development of yttrium-containing self-passivating tungsten alloys for future fusion power plants, Nuclear Materials and Energy 9 (2016) 394 – 398. doi:10.1016/j.nme.2016.07.011.

[247] A. Litnovsky, T. Wegener, F. Klein, C. Linsmeier, M. Rasinski, A. Kreter, X. Tan, J. Schmitz, J. W. Coenen, Y. Mao, J. Gonzalez-Julian, M. Bram, New oxidation-resistant tungsten alloys for use in the nuclear fusion reactors, Physica Scripta T170 (2017) 014012. doi:10.1088/1402-4896/aa81f5.

[248] F. Klein, T. Wegener, A. Litnovsky, M. Rasinski, X. Tan, J. Gonzalez-Julian, J. Schmitz, M. Bram, J. Coenen, C. Linsmeier, Oxidation resistance of bulk plasma-facing tungsten alloys, Nuclear Materials and Energy 15 (2018) 226 – 231. doi:10.1016/j.nme.2018.05.003.

[249] A. Litnovsky, T. Wegener, F. Klein, C. Linsmeier, M. Rasinski, A. Kreter, B. Unterberg, M. Vogel, S. Kraus, U. Breuer, C. Garcia-Rosales, A. Calvo, N. Ordas, Smart alloys for a future fusion power plant: First studies under stationary plasma load and in accidental conditions, Nuclear Materials and Energy 12 (2017) 1363 – 1367, proceedings of the 22nd International Conference on Plasma Surface Interactions 2016, 22nd PSI. doi:10.1016/j.nme.2016.11.015.

[250] P. Bleuet, E. Welcomme, E. Dooryhée, J. Susini, J.-L. Hodeau, P. Walter, Probing the structure of heterogeneous diluted materials by diffraction tomography, Nature Materials 7 (2008) 468–472, proceedings of the 22nd International Conference on Plasma Surface Interactions 2016, 22nd PSI. doi:10.1038/nmat2168.

[251] T. Ungár, Microstructural parameters from x-ray diffraction peak broadening, Scripta Materialia 51 (8) (2004) 777 – 781, viewpoint set no. 35. Metals and alloys with a structural scale from the micrometer to the atomic dimensions. doi:10.1016/j.scriptamat.2004.05.007.

[252] D. Sprouster, J. Trelewicz, L. Snead, X. Hu, D. Morrall, T. Koyanagi, C. Parish, L. Tan, Y. Katoh, B. Wirth, Advanced synchrotron characterization techniques for fusion materials science, Journal of Nuclear Materials 543 (2021) 152574. doi:https://doi.org/10.1016/j.jnucmat.2020.152574.

[253] A. Bhattacharya, C. M. Parish, J. Henry, Y. Katoh, High throughput crystal structure and composition mapping of crystalline nanoprecipitates in alloys by transmission kikuchi diffraction and analytical electron microscopy, Ultramicroscopy 202 (2019) 33 – 43. doi:10.1016/j.ultramic.2019.03.015.

[254] K. Hattar, D. Bufford, D. Buller, Concurrent in situ ion irradiation transmission electron microscope, Nuclear Instruments and Methods in Physics

Research Section B: Beam Interactions with Materials and Atoms 338 (2014) 56 – 65. doi:10.1016/j.nimb.2014.08.002.

[255] L. Jiang, Y.-J. Hu, K. Sun, P. Xiu, M. Song, Y. Zhang, W. L. Boldman, M. L. Crespillo, P. D. Rack, L. Qi, W. J. Weber, L. Wang, Irradiation-induced extremes create hierarchical face-/body-centered-cubic phases in nanostructured high entropy alloys, Advanced Materials 32 (39) (2020) 2002652. doi:https://doi.org/10.1002/adma.202002652.

[256] V. Krsjak, J. Degmova, S. Sojak, V. Slugen, Effects of displacement damage and helium production rates on the nucleation and growth of helium bubbles positron annihilation spectroscopy aspects, Journal of Nuclear Materials 499 (2018) 38 – 46. doi:10.1016/j.jnucmat.2017.11.007.

[257] F. Tuomisto, I. Makkonen, J. Heikinheimo, F. Granberg, F. Djurabekova, K. Nordlund, G. Velisa, H. Bei, H. Xue, W. Weber, Y. Zhang, Segregation of Ni at early stages of radiation damage in NiCoFeCr solid solution alloys, Acta Materialia 196 (2020) 44–51. doi:https://doi.org/10.1016/j.actamat.2020.06.024.

[258] P. Edmondson, A. London, A. Xu, D. Armstrong, S. Roberts, Small-scale characterisation of irradiated nuclear materials: Part i microstructure, Journal of Nuclear Materials 462 (2015) 369 – 373. doi:10.1016/j.jnucmat.2014.11.067.

[259] X. Wang, C. Hatzoglou, B. Sneed, Z. Fan, W. Guo, K. Jin, D. Chen, H. Bei, Y. Wang, W. J. Weber, Y. Zhang, B. Gault, K. L. More, F. Vurpillot, J. D. Poplawsky, Interpreting nanovoids in atom probe tomography data for accurate local compositional measurements, Nature Communications 11 (2020) 1022. doi:https://doi.org/10.1038/s41467-020-14832-w.

[260] G. Odette, M. Alinger, B. Wirth, Recent developments in irradiation-resistant steels, Annual Review of Materials Research 38 (1) (2008) 471–503. doi:10.1146/annurev.matsci.38.060407.130315.

[261] I. Beyerlein, A. Caro, M. Demkowicz, N. Mara, A. Misra, B. Uberuaga, Radiation damage tolerant nanomaterials, Materials Today 16 (11) (2013) 443 – 449. doi:10.1016/j.mattod.2013.10.019.

[262] I. M. Robertson, C. A. Schuh, J. S. Vetrano, N. D. Browning, D. P. Field, D. J. Jensen, M. K. Miller, I. Baker, D. C. Dunand, R. Dunin-Borkowski, et al., Towards an integrated materials characterization toolbox, Journal of Materials Research 26 (11) (2011) 13411383. doi:10.1557/jmr.2011.41.

[263] Y. Zhang, A. Debelle, A. Boulle, P. Kluth, F. Tuomisto, Advanced techniques for characterization of ion beam modified materials, Current Opinion in Solid State and Materials Science 19 (1) (2015) 19 – 28, ion Beam Modification of Materials. doi:10.1016/j.cossms.2014.09.007.

[264] L. Tan, L. Snead, Y. Katoh, Development of new generation reduced activation ferritic-martensitic steels for advanced fusion reactors, Journal of Nuclear Materials 478 (2016) 42 – 49. doi:10.1016/j.jnucmat.2016.05.037.

[265] Y. TAKAHASHI, M. MURABAYASHI, Measurement of thermal properties of nuclear materials by laser flash method, Journal of Nuclear Science and Technology 12 (3) (1975) 133–144. doi:10.1080/18811248.1975.9733082.

[266] M. Khafizov, C. Yablinsky, T. R. Allen, D. H. Hurley, Measurement of thermal conductivity in proton irradiated silicon, Nuclear Instruments and Methods in Physics Research Section B: Beam Interactions with Materials and Atoms 325 (2014) 11 – 14. doi:10.1016/j.nimb.2014.02.003.

[267] F. Hofmann, M. P. Short, C. A. Dennett, Transient grating spectroscopy: An ultrarapid, nondestructive materials evaluation technique, MRS Bulletin 44 (5) (2019) 392402. doi:10.1557/mrs.2019.104.

[268] M. C. Hoffmann, J. Hebling, H. Y. Hwang, K.-L. Yeh, K. A. Nelson, Impact ionization in insb probed by terahertz pump—terahertz probe spectroscopy, Phys. Rev. B 79 (2009) 161201. doi:10.1103/PhysRevB.79.161201.

[269] C. Dennett, K. So, A. Kushima, D. Buller, K. Hattar, M. Short, Detecting self-ion irradiation-induced void swelling in pure copper using transient grating spectroscopy, Acta Materialia 145 (2018) 496 – 503. doi:10.1016/j.actamat.2017.12.007.

[270] C. Frez, G. J. Diebold, C. D. Tran, S. Yu, Determination of thermal diffusivities, thermal conductivities, and sound speeds of room-temperature ionic liquids by the transient grating technique, J. Chem. Eng. Data 51 (2006) 1250–1255. doi:10.1021/je0600092.

[271] A. T. Motta, L. Capolungo, L.-Q. Chen, M. N. Cinbiz, M. R. Daymond, D. A. Koss, E. Lacroix, G. Pastore, P.-C. A. Simon, M. R. Tonks, B. D. Wirth, M. A. Zikry, Hydrogen in zirconium alloys: A review, J. Nucl. Mater. 518 (2019) 440 – 460. doi:10.1016/j.jnucmat.2019.02.042.

[272] E. Wakai, K. Kikuchi, S. Yamamoto, T. Aruga, M. Ando, H. Tanigawa, T. Taguchi, T. Sawai, K. Oka, S. Ohnuki, Swelling behavior of f82h steel irradiated by triple/dual ion beams, J. Nucl. Mater. 318 (2003) 267 – 273, fifth International Workshop on Spallation Materials Technology. doi:10.1016/S0022-3115(03)00122-3.

[273] K. Farrell, E. Lee, Ion Damage in a Fe-10Cr-6Mo-0.5Nb Ferritic Steel., Vol. ASTM STP955, ASTM International, West Conshohocken, PA, 1987, pp. 498–507, Radiation-Induced Changes in Microstructure: 13th International Symposium (Part I).

[274] F. Garner, E. Simonen, B. Oliver, L. Greenwood, M. Grossbeck, W. Wolfer, P. Scott, Retention of hydrogen in fcc metals irradiated at temperatures leading to high densities of bubbles or voids, J. Nucl. Mater. 356 (1) (2006) 122 – 135, proceedings of the Seventh International Workshop on Spallation Materials Technology. doi:10.1016/j.jnucmat.2006.05.023.

[275] S. M. Myers, F. Besenbacher, J. Bøttiger, Deuterium in he-implanted fe: Trapping and the surface permeation barrier, Applied Physics Letters 39 (5) (1981) 450–452. doi:10.1063/1.92735.

[276] C. Judge, H. Rajakumar, A. Korinek, G. Bickel, On the potential synergies of helium and hydrogen on the nucleation and stability of cavity clusters in inconel x-750 irradiated in a high thermal neutron flux spectra, in: 19th International Conference on Environmental Degradation of Materials in Nuclear Power Systems - Water Reactors, August 18-22, 2019, Boston, MA.

[277] E. Hayward, C. Deo, Synergistic effects in hydrogen–helium bubbles, J. Phys.: Condens. Matter 24 (26) (2012) 265402. doi:10.1088/0953-8984/24/26/265402.

[278] Z. J. Bergstrom, M. A. Cusentino, B. D. Wirth, A molecular dynamics study of subsurface hydrogen-helium bubbles in tungsten, Fus. Sci. Tech. 71 (1) (2017) 122–135. doi:10.13182/FST16-121.

[279] Z. J. Bergstrom, L. Yang, B. D. Wirth, An ab-initio study of hydrogen trapping at bcc w metal noble gas interfaces, J. Appl. Phys.Under review.

[280] S. Taller, D. Woodley, E. Getto, A. M. Monterrosa, Z. Jiao, O. Toader, F. Naab, T. Kubley, S. Dwaraknath, G. S. Was, Multiple ion beam irradiation for the study of radiation damage in materials, Nuclear Instruments and Methods in Physics Research Section B: Beam Interactions with Materials and Atoms 412 (2017) 1 – 10. doi:10.1016/j.nimb.2017.08.035.

[281] G. Shaw, W. Garcia, X. Hu, B. D. Wirth, Investigating helium–deuterium synergies in plasma-exposed tungsten using laser ablation techniques, Physica Scripta T171 (2020) 014029. doi:10.1088/1402-4896/ab47c7.

[282] O. El-Atwani, J. E. N. II, A. C. Leff, J. K. Baldwin, K. Hattar, M. L. Taheri, Evidence of a temperature transition for denuded zone formation in nanocrystalline fe under he irradiation, Materials Research Letters 5 (3) (2017) 195–200. doi:10.1080/21663831.2016.1243591.

[283] O. El-Atwani, W. Cunningham, D. Perez, E. Martinez, J. Trelewicz, M. Li, S. Maloy, Temperature threshold for preferential bubble formation on grain boundaries in tungsten under in-situ helium irradiation, Scripta Materialia 180 (2020) 6–10. doi:https://doi.org/10.1016/j.scriptamat.2020.01.013.

[284] B. N. Nguyen, R. J. Kurtz, F. Gao, Modeling the effects of helium-vacancy clusters on the stress-strain response of a grain boundary in iron by a mechanistic finite element approach informed by molecular dynamics data, J. Nucl. Mater. 526 (2019) 151766. doi:10.1016/j.jnucmat.2019.151766.

[285] J. Messina, R. Luo, K. Xu, G. Lu, H. Deng, M. Tschopp, F. Gao, Utilizing machine learning to predict aluminum segregation in magnesium grain boundariesIn preparation.

[286] B. R. Johnson, M. R. Elmore, B. McCarthy, J. Lang, B. Schmitt, J. Birnbaum, K. Geelhood, A. Devaraj, Formation and diffusion of zirconium hydrides in nickel-plated zircaloy-4 tubing, Tech. Rep. PNNL-27232, Pacific Northwest National Laboratory, Richland, Washington (2017).

[287] Q. Yu, M. Reyes, N. Shah, J. Marian, Kinetic model of incipient hydride formation in zr clad under dynamic oxide growth conditions, Materials 13 (5) (2020) 1088.

[288] W. G. Luscher, D. J. Senor, K. K. Clayton, G. R. Longhurst, In situ measurement of tritium permeation through stainless steel, Journal of Nuclear Materials 437 (1) (2013) 373 – 379. doi:10.1016/j.jnucmat.2013.02.009.

[289] G. Nandipati, W. Setyawan, C. H. Henager, D. J. Senor, Progress toward developing a mechanistic understanding of tritium permeation in tpbars, Tech. Rep. PNNL-26890, Pacific Northwest National Laboratory, Richland, Washington (2017).

[290] E. C. Buck, D. D. Reilly, P. J. MacFarlan, J. A. Trevino, G. J. Sevigny, B. W. Arey, Irradiated tritium-bearing pellet characterization, Tech. Rep. PNNL-28289, Pacific Northwest National Laboratory, Richland, Washington (2019).

[291] W. Setyawan, R. Devanathan, Modeling the irradiation enhancement of diffusion and phase changes in pellets, Tech. Rep. PNNL-25938, Pacific Northwest National Laboratory, Richland, Washington (2016).

[292] Q. Yu, M. J. Simmonds, R. Doerner, G. R. Tynan, L. Yang, B. D. Wirth, J. Marian, Understanding hydrogen retention in damaged tungsten using experimentally-guided models of complex multispecies evolution, Nuclear Fusion 60 (9) (2020) 096003.

[293] N. Fernandez, Y. Ferro, D. Kato, Hydrogen diffusion and vacancies formation in tungsten: density functional theory calculations and statistical models, Acta Materialia 94 (2015) 307–318.

[294] J. Hou, X.-S. Kong, X. Wu, J. Song, C. Liu, Predictive model of hydrogen trapping and bubbling in nanovoids in bcc metals, Nature materials 18 (8) (2019) 833–839.

[295] Y.-N. Liu, T. Ahlgren, L. Bukonte, K. Nordlund, X. Shu, Y. Yu, X.-C. Li, G.-H. Lu, Mechanism of vacancy formation induced by hydrogen in tungsten, AIP advances 3 (12) (2013) 122111.

[296] K. Ohsawa, F. Nakamori, Y. Hatano, M. Yamaguchi, Thermodynamics of hydrogen-induced superabundant vacancy in tungsten, Journal of Nuclear Materials 458 (2015) 187–197.

[297] A. Sand, J. Byggmästar, A. Zitting, K. Nordlund, Defect structures and statistics in overlapping cascade damage in fusion-relevant bcc metals, Journal of Nuclear Materials 511 (2018) 64 – 74, special Section on 18th International Conference on Fusion Reactor Materials. doi:10.1016/j.jnucmat.2018.08.049.

[298] A. Fellman, A. E. Sand, J. Byggmästar, K. Nordlund, Radiation damage in tungsten from cascade overlap with voids and vacancy clusters, Journal of Physics: Condensed Matter 31 (40) (2019) 405402. doi:10.1088/1361-648x/ab2ea4.

[299] D. R. Mason, S. Das, P. M. Derlet, S. L. Dudarev, A. J. London, H. Yu, N. W. Phillips, D. Yang, K. Mizohata, R. Xu, F. Hofmann, Relaxation volumes of microscopic and mesoscopic irradiation-induced defects in tungsten, Physical Review Letters 125 (2021) 225503. doi:10.1103/PhysRevLett.125.225503.

[300] S. Chmiela, H. E. Sauceda, K.-R. Müller, A. Tkatchenko, Towards exact molecular dynamics simulations with machine-learned force fields, Nat. Commun. 9 (2018) 1–10. doi:10.1038/s41467-018-06169-2.

[301] P. Hauseux, T.-T. Nguyen, A. Ambrosetti, K. S. Ruiz, S. P. A. Bordas, A. Tkatchenko, From quantum to continuum mechanics in the delamination of atomically-thin layers from substrates, Nat. Commun. 11 (2020) 1–8. doi:10.1038/s41467-020-15480-w.

[302] S. Araki, K. Mashima, T. Masumura, T. Tsuchiyama, S. Takaki, T. Ohmura, Effect of grain boundary segregation of carbon on critical grain boundary strength of ferritic steel, Scripta Materialia 169 (2019) 38 – 41. doi:10.1016/j.scriptamat.2019.05.001.

[303] G. Was, S. Taller, Z. Jiao, A. Monterrosa, D. Woodley, D. Jennings, T. Kubley, F. Naab, O. Toader, E. Uberseder, Resolution of the carbon contamination problem in ion irradiation experiments, Nuclear Instruments and Methods in Physics Research Section B: Beam Interactions with Materials and Atoms 412 (2017) 58 – 65. doi:10.1016/j.nimb.2017.08.039.

[304] R. Ngayam-Happy, C. Becquart, C. Domain, First principle-based akmc modelling of the formation and medium-term evolution of point defect and

solute-rich clusters in a neutron irradiated complex fe-cumnnisip alloy representative of reactor pressure vessel steels, Journal of Nuclear Materials 440 (1) (2013) 143 – 152. doi:10.1016/j.jnucmat.2013.04.081.

[305] D. Sprouster, J. Sinsheimer, E. Dooryhee, S. Ghose, P. Wells, T. Stan, N. Almirall, G. Odette, L. Ecker, Structural characterization of nanoscale intermetallic precipitates in highly neutron irradiated reactor pressure vessel steels, Scripta Materialia 113 (2016) 18 – 22. doi:10.1016/j.scriptamat.2015.10.019.

[306] A. Reza, C. A. Dennett, M. P. Short, J. Waite, Y. Zayachuk, C. M. Magazzeni, S. Hills, F. Hofmann, Non-contact, non-destructive mapping of thermal diffusivity and surface acoustic wave speed using transient grating spectroscopy, Review of Scientific Instruments 91 (5) (2020) 054902. doi:10.1063/5.0003742.

[307] J. Marian, T. Hoang, M. Fluss, L. L. Hsiung, A review of helium-hydrogen synergistic effects in radiation damage observed in fusion energy steels and an interaction model to guide future understanding, Journal of Nuclear Materials 462 (2015) 409 – 421. doi:10.1016/j.jnucmat.2014.12.046.

[308] I. I. Chernov, M. S. Staltsov, B. A. Kalin, L. Y. Guseva, Some problems of hydrogen in reactor structural materials: A review, Inorganic Materials: Applied Research 8 (5) (2017) 643–650. doi:10.1134/S2075113317050094.

[309] A. Bhattacharya, E. Meslin, J. Henry, B. Dcamps, A. Barbu, Dramatic reduction of void swelling by helium in ion-irradiated high purity -iron, Materials Research Letters 6 (7) (2018) 372–377. doi:10.1080/21663831.2018.1462266.

[310] Y. Zayachuk, M. H. J. 't Hoen, I. Uytdenhouwen, G. V. Oost, Thermal desorption spectroscopy of W–Ta alloys, exposed to high-flux deuterium plasma, Physica Scripta T145 (2011) 014041. doi:10.1088/0031-8949/2011/t145/014041.

[311] A. Hollingsworth, M. Lavrentiev, R. Watkins, A. Davies, S. Davies, R. Smith, D. Mason, A. Baron-Wiechec, Z. Kollo, J. Hess, I. Jepu, J. Likonen, K. Heinola, K. Mizohata, E. Meslin, M.-F. Barthe, A. Widdowson, I. Grech, K. Abraham, E. Pender, A. McShee, Y. Martynova, M. Freisinger, A. D. Backer, Comparative study of deuterium retention in irradiated Eurofer and Fe–Cr from a new ion implantation materials facility, Nuclear Fusion 60 (1) (2019) 016024. doi:10.1088/1741-4326/ab546e.